An investigation of shaft line torsional vibration during ice impacts on PSRVs

by
Rosca Johan Oscar de Waal

Thesis presented in partial fulfilment of the requirements for the degree of Master of Engineering (Mechanical) in the Faculty of Engineering at Stellenbosch University

Supervisor: Dr. Anriëtte Bekker
Co-supervisor: Prof. Philippus Stephanus Heyns

March 2017

Declaration

By submitting this thesis electronically, I declare that the entirety of the work contained therein is my own, original work, that I am the sole author thereof (save to the extent explicitly otherwise stated), that reproduction and publication thereof by Stellenbosch University will not infringe any third party rights and that I have not previously in its entirety or in part submitted it for obtaining any qualification.

Date: ..... March 2017 .....

Abstract

An investigation of shaft line torsional vibration during ice impacts on PSRVs

R.J.O. de Waal

Department of Mechanical and Mechatronic Engineering,
Stellenbosch University,
Private Bag X1, Matieland 7602, South Africa.

Thesis: MEng (Mech)

March 2017

In order to estimate the forces exerted on ship propellers during ice navigation, the rotational dynamics of the propulsion system need to be accurately modelled. The direct measurements of propeller loads of ships during ice navigation is challenged by the harsh operating environment. Indirect measurements are therefore performed on the shaft line of such ships to estimate propeller loads through an inverse problem. Three case studies are presented, namely open water, cavitation and ice navigation. The maximum torque loading on the shaft occurred during ice navigation and the maximum thrust case during cavitation. Ice-induced moments on the SAA II propeller were determined from shaft line measurements using inverse methods, whereby the maximum ice load was found to be 941 kNm. Estimated load profiles for navigation in the Arctic and Antarctica are presented using rainflow counting techniques. The aim of the present research was to perform data-driven modelling of the rotational dynamics of the shaft line to aid future design of ice going vessels.

Uittreksel

'n Ondersoek van dryfas torsionele vibrasie tydens ysimpak op pool verskaffings- en navorsingskepe

R.J.O. de Waal

Departement Meganiese en Megatroniese Ingenieurswese,
Universiteit van Stellenbosch,
Privaatsak X1, Matieland 7602, Suid Afrika.

Tesis: MIng (Meg)

Maart 2017

Ten einde die kragte op 'n skip se aandrywingstelsel te bepaal, moet die rotasionele dinamika van die stelsel gemodelleer word terwyl die skip vaar. Tydens ysnavigasie is die direkte bepaling van skroeflaste van skepe uitdagend weens die ruwe operasionele omgewing. Om skroeflaste te bepaal word indirekte metings op die dryfaste van sulke skepe uitgevoer. 'n Inverse probleem moet opgelos word om die beraamde skroeflaste te bepaal. Drie gevallestudies word aangebied, naamlik oop water, kavitasie en ysnavigasie. Die maksimum wringkrag is gedurende ysnavigasie en die maksimum stukrag gevalle is gedurende kavitasie gemeet. Die wringkrag weens ysimpakte op die SAA II skroef is bepaal deur dryfas-metings en die daaropvolgende inverse metodes. 'n Maksimum yslading van 941 kNm is bepaal. Geraamde lasprofiele vir navigasie in die Arktiese see en Antarktika word aangebied deur gebruik te maak van reënval-tellingstegnieke. Die doel van die huidige navorsing behels die toepassing van data gedrewe modellering op die rotasionele dinamika van die dryfas tot voordeel van die ontwerp van ysnavigasie skepe in die toekoms.

Acknowledgements

I would like to express my sincere gratitude to the following people and organisations:

- Dr. Annie Bekker for her support and contribution throughout the duration of this project.
- Prof. Stephan Heyns from University of Pretoria for his guidance and post-graduate funding.
- Ferdie Zietsman and the workshop members for always being willing to help and set time aside.
- SANAP for accommodating this project.
- Captain Gavin and his crew on-board the SAA II during the 2014/2015 and 2015/2016 voyage for their assistance and time.
- Kapitän Stefan Schwarze and his crew on-board the Polarstern during the 2016 PS100 voyage for their willingness and assistance during research.

Dedications

This thesis is dedicated to my family and friends.

Contents

List of Figures

List of Tables

Nomenclature

Variables

A	cross-sectional area	$[\mathrm{m}^2]$
A_i	vector variable	$[\mathrm{N \cdot m/rad}]$
B	dynamic model matrix	$[\mathrm{N \cdot m/rad}]$
B_i	dynamic model matrix elements	$[\mathrm{N \cdot m/rad}]$
C	torsional damping matrix	$[\mathrm{N \cdot m \cdot s/rad}]$
c_i	torsional damping elements	$[\mathrm{N \cdot m \cdot s/rad}]$
C_q	empirical coefficient	$[\ ]$
c_p	propagation speed	$[\mathrm{m/s}]$
D	propeller diameter	$[\mathrm{m}]$
D_{limit}	propeller diameter limiting value	$[\mathrm{m}]$
d_h	propeller hub external diameter	$[\mathrm{m}]$
d_{in}	inner diameter	$[\mathrm{m}]$
d_o	outer diameter	$[\mathrm{m}]$
E	modulus of elasticity	$[\mathrm{Pa}]$

EAR	expanded blade area ratio	[ ]
$e_{i,j,k}$	elements of matrix W	[N · m/rad]
F_b	maximum backward blade force	[N]
F_f	maximum forward blade force	[N]
f	frequency	[Hz]
f_z	immersion function	[ ]
G	shear modulus	[Pa]
H	impulse response matrix	[ ]
H_{ice}	maximum ice thickness	[m]
h_i	impulse response matrix elements	[ ]
h_o	depth of the propeller centreline	[m]
I	number of stress blocks	[ ]
J_i	polar moment of inertia	[kg · m^2]
j	number of retained singular values	[ ]
K_b	bulk modulus of elasticity	[Pa]
K	torsional rigidity matrix	[N · m/rad]
K_a	Load response factor	[ ]
k	gauge factor	[ ]
k_i	torsional rigidity elements	[N · m/rad]
k_w	Weibull shape parameter	[ ]

$k_{1,2}$	multiplication factor	[ ]
L	regularization matrix	[ ]
l	length	[m]
M	diagonal matrix of L	[ ]
MDR	Miner Palmgrens accumulated fatigue damage ratio	[ ]
N_z	number of cycles to failure in stress block z	[ ]
N_{ice}	number of ice impacts	[ ]
N_{class}	reference number of impacts	[ ]
$N_{1,2,3,4,5}$	multiplication constant	[ ]
n	propeller rotational speed	[rps]
n_e	number of non-zero eliminated singular values	[ ]
n_z	number of cycles in stress block z	[ ]
P_D	propulsion power	[W]
$P_{0.7}$	propeller pitch at 0.7 times the radius	[m]
p	number of rows in matrix L	[ ]
Q	torque vector	[N · m]
Q_{ice}	ice induced external moment	[N · m]
Q_{shaft}	measured internal torque in shaft	[N · m]
Q_A	response torque amplitude on shaft	[N · m]
$q_{p,i}$	ice induced external moment elements	[N · m]

$q_{shaft,i}$	measured internal torque in shaft elements	$[\mathrm{N \cdot m}]$
R	electrical resistance	$[\Omega]$
R_T	total vessel resistance	$[\mathrm{N}]$
S_{ice}	ice strength index for blade ice force	$[\ ]$
S_p	polar modulus	$[\mathrm{m}^4]$
T_{prop}	propeller thrust	$[\mathrm{N}]$
T_{shaft}	measured axial thrust in shaft	$[\mathrm{N}]$
t	time	$[\mathrm{s}]$
t_d	thrust deduction factor	$[\ ]$
U	left singular vectors of H	$[\ ]$
U_A	output voltage	$[\mathrm{V}]$
U_E	excitation voltage	$[\mathrm{V}]$
u	left singular elements	$[\ ]$
V	right singular vectors of H	$[\ ]$
V_s	vessel speed	$[\mathrm{m/s}]$
v	right singular elements	$[\ ]$
W	dynamic model matrix	$[\mathrm{N \cdot m/rad}]$
w	wake fraction	$[\ ]$
X	non-singular matrix of L	$[\ ]$
X_r	vessel resistance	$[\mathrm{N}]$

x	non-singular matrix elements of L	[ ]
Z	number of propeller blades	[ ]
α	propeller rotational angle	[deg]
β	Newmark-Beta parameter	[ ]
γ	Newmark-Beta parameter	[ ]
γ_s	shear strain	[mm/mm]
γ_{xy}	shear strain for plane-strain condition	[mm/mm]
ε	normal strain	[mm/mm]
ε_x	x-axis strain for plane-strain condition	[mm/mm]
ε_y	y-axis strain for plane-strain condition	[mm/mm]
η_D	propulsive efficiency	[ ]
η_H	hull efficiency	[ ]
η_O	open water efficiency	[ ]
η_R	rotational efficiency	[ ]
λ	Tikhonov regularization parameter	[ ]
μ	diagonal matrix elements of L	[ ]
ν	Poisson's ratio	[ ]
ρ	material density	[kg/m^3]
Σ	diagonal matrix of non-negative singular values of H	[ ]

σ	non-negative singular value elements of H	[ ]
σ_s	normal stress	[Pa]
τ	shear stress	[Pa]
Φ	variable of integration	[s]
ω	rotational speed	[rad/s]

Vectors

θ	angular displacement	[rad]
$\dot{\theta}$	angular velocity	[rad/s]
$\ddot{\theta}$	angular acceleration	[rad/s^2]

Subscripts

i	Point i = 1, 2, 3,...,13
max	maximum
o	original
x	x-axis
y	y-axis
z	z-axis

Acronyms

AWI Alfred Wegener Institut

A/D analog-to-digital

CMU central measurement unit

CPP controllable pitch propeller

DAQ data acquisition

DNV Det Norske Veritas

EAR expanded blade area ratio

FFT fast fourier transform

GPS global positioning system

GSVD generalized singular value decomposition

HBM Hottinger Baldwin Messtechnik

IACS International Association of Classification Societies

LXRS lossless extended range synchronized

MatLab Matrix Laboratory

MCR maximum continuous rating

PC polar class

PSRV polar supply and research vessel

rpm revolutions per minute

SA South Africa

SAA II SA Agulhas II

SANAE South African National Antarctic Expeditions

SANAP South African National Antarctic Program

SOG speed over ground

SVD singular value decomposition

TTVC transient torsional vibration calculations

TVC torsional vibration calculations

Wi-Fi wireless fidelity

Chapter 1

Introduction

Efficient and safe shipping in Arctic regions is an increasing requirement due to maritime transport in ice-covered seas being expected to increase in future decades (Ikonen *et al.*, 2014). Vessel passage through ice-infested waters entails exposure to additional ice-related loads on the propulsion system. This affects the efficiency and safety of vessel operations (Polić *et al.*, 2014) and could result in failure of a shaft line element if not accounted for. The propeller is therefore required to operate efficiently in ice and open water while withstanding both extreme loads and fatigue loads (Huisman *et al.*, 2014). Extreme and cyclic moderate loading of the propeller is increased during propeller-ice interaction, where extreme loading dictates the ultimate strength of propeller design and cyclic moderate loading determines the fatigue life of the propeller (Huisman *et al.*, 2014). Ice going vessels are exposed to transient torsional vibration induced by propeller-ice interaction which leads to the interest in the effect of ice loads on the propulsion system of such vessels (Batrak *et al.*, 2014).

Ice-related loads are typically measured between the engine and the propeller on the shaft for both full-scale trials and model-scale tests (Polić *et al.*, 2014). These loads are therefore not measured directly and include the dynamic response of the mechanical transmission line elements (Polić *et al.*, 2014). The use of numerical methods can help to predict the global loads but are not adequate for efficiency and reliability design optimization of the propeller (Huisman *et al.*, 2014). It has been determined by Tang and Brennan

(2013) that multi-point measurements should be made instead of the conventional method involving a single measurement at the free end of the shaft, especially for shaft lines containing highly flexible components. Significant local deformation of different modes results in single measurements of full torsional vibration characteristics of the shafting system not being obtainable (Tang and Brennan, 2013). There exists no in-depth, definitive study on propeller-ice interaction (Sampson *et al.*, 2009) and there is a lack of knowledge regarding the physical processes during propeller-ice interaction that cause these loads (Huisman *et al.*, 2014).

Shipping registers, such as Korean Register (Korean Register, 2015), American Bureau of Shipping (American Bureau of Shipping, 2006), Det Norske Veritas (DNV) (Det Norske Veritas, 2011*a*) and Lloyd's Register (Germanischer Lloyd, 2007) specify the requirement for calculation of torsional shaft line vibration during the design stage. Full-scale measurements are subsequently performed during sea trials in order to ensure safe vessel operation (Tang and Brennan, 2013). A study by the Transportation Safety Board of Canada (2010) found that propulsion system failure is still one of the greatest contributors to vessel failure. This motivates the need for further study in this field.

Classical steady-state torsional vibration calculations exist for propulsion shafts based on frequency domain analyses and have established guidelines which guarantee safe vessel operation in open water (Batrak *et al.*, 2014). However, for ice-infested waters, transient torsional vibration calculations (TTVC) are required that are based on the time-domain approach (Batrak *et al.*, 2014). The complication with ice induced TTVC is that the classical methods used, for numeric integration of a system of differential equations, are inefficient and time-consuming (Batrak *et al.*, 2014). It is due to this reason that there are recommendations to use a lumped mass model approach to simplify the propulsion system.

Other complications in TTVC induced by ice impacts are the uncertainties involved. There is a significant increase in the effective propeller inertia when ice blocks are milled through a propeller. To date, there is yet insufficient knowledge with regards to this process (Batrak *et al.*, 2014). Ice milling

causes an associated reduction in engine rotational speed causing the propeller to operate in transient conditions (Batrak *et al.*, 2014). For a correct approach, dynamic stiffness of the couplings should be used for the fast components and static stiffness for the slow components, but this is impossible to implement with TTVC and thus it is advised to use the static stiffness only for the calculations (Batrak *et al.*, 2014). All the aforementioned uncertainties question the effort required to make TTVC as accurate as possible, as well as the ability to determine exact ice-propeller loads from shaft line measurements.

The data required for the torque analysis can be obtained from one of two methods; scale models which are quicker and less costly, or full-scale measurements which are very time-consuming and costly. Full-scale measurements offer advantages over a model-scale approach: a model test rig is to be designed to be capable of measuring highly dynamic moments and forces in all directions and be extensively calibrated and tested under controlled conditions (Brouwer *et al.*, 2013). Although model testing provides a cost-effective method for analysis, full-scale measurements of vessels provide accurate performance data of the vessel relative to the environmental conditions (Dinham-Peren and Dand, 2010).

The aim of the present investigation was to perform data-driven modelling of the rotational dynamics of the shaft line for the following reasons:

- Contribute towards sparse literature of full-scale measurements and operational techniques through which loads can be identified and compared.
- Investigate the possible effects of ice loading and cavitation on shaft line dynamics.
- Obtain a realistic ice-induced loading profile for vessels sailing in ice infested waters to Antarctica and the Arctic.
- Determine propeller-ice loading from shaft line measurements to aid future design of ice-going vessels.

A consortium comprising STX Finland, Aker Arctic, Rolls Royce, Wärtsilä, Smit Vessel management Services, The Department of Environmental Affairs

of South Africa, University of Aalto (Espoo, Finland), University of Oulu (Espoo, Finland) and Stellenbosch University (South Africa) has been studying the full-scale measurements of the SA Agulhas II (SAA II) polar supply and research vessel (PSRV) during open water and ice-going responses in the Bay of Bothnia and on four voyages between Cape Town and Antarctica during 2012 to 2016. Stellenbosch University, in collaboration with Alfred Wegener Institut (AWI), also performed full-scale measurements on the Polarstern PSRV during a voyage to the Arctic in 2016.

During the manufacturing of the SAA II in 2012, KYOWA strain gauges with a Manner Telemetry system were installed in order to determine torque and thrust on the port side intermediate shaft line (Kujala *et al.*, 2014). The data obtained from this system was found to contain disturbances and noise by Myklebost and Dahler (2013) during the 2012/2013 voyage to Antarctica. An attempt was made to fix the system during the 2014/2015 voyage, but the validity of the data remained questionable. A supplementary system, consisting of a V-link lossless extended range synchronized (LXRS) and WSDA-Base, was installed during the 2015/2016 voyage to validate the previously recorded data. The V-link system was also used to perform measurements on the Polarstern during a voyage to the Arctic in 2016.

A flow diagram describing the processes performed during this study is presented in Figure 1.1. The sequence of events were as follows:

1. Shaft line measurements were validated through numerical methods, machine control data and model tests.

2. Full-scale measurements on-board the PSRVs were recorded and processed.

3. Effects of cavitation and ice impacts on the shaft line dynamics were analysed through the time and frequency domain approach.

4. Lumped mass model of the SAA II shaft line was obtained.

5. The transfer function between external ice-induced moments and measured internal torque was determined.

6. Inverse methods were formulated through singular value decomposition (SVD), generalized singular value decomposition (GSVD) and Tikhonov regularization methods.

7. External ice-induced loading on the propeller was determined from shaft line measurements.

External ice-induced loading on the propeller was only determined for the SAA II due to a limitation in the required information for a lumped mass model of the Polarstern shaft line.

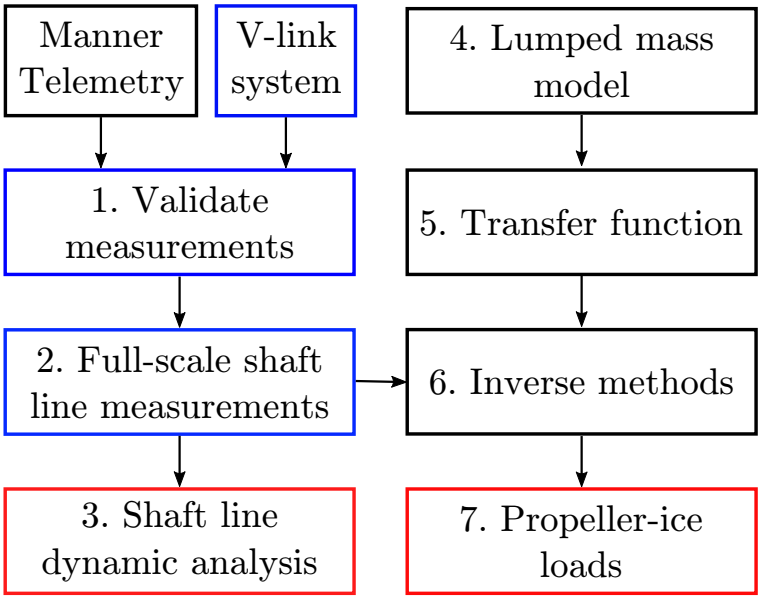

Figure 1.1: Outline of thesis approach to determine shaft line dynamic analysis and ice induced loading on the propeller. Black boxes were only applicable to the SAA II and red boxes define the end result.

Chapter 2

Literature study

Determining ice-induced propeller loads from shaft line measurements is complicated due to the measured loads on the shaft including the dynamic response of the shaft line. To better understand this principle, the relevant shaft line components will be discussed and the concept of torsional vibration explained. Furthermore, the process of determining internal torque and thrust through strain gauge measurements will be explained, followed by methods for numerically determining the dynamic shaft line response.

2.1 Propulsion machinery

Propulsion machinery enable motion of a vessel in ice and open water through a coupled system consisting of the following main components: a diesel engine and/or electric motor connected to a transmission line with a propeller. A typical propulsion system encompassing these elements is presented in Figure 2.1.

The propeller is a rotational element that creates directional thrust from the machine power, by inducing a pressure difference between its suction and pressure surface (Polić *et al.*, 2014). When a vessel operates in ice-infested waters, the first element of the propulsion machinery to interact with ice is the propeller. This transfers the ice-related loads to other elements of the transmission system, as presented in Figure 2.1 (Polić *et al.*, 2014).

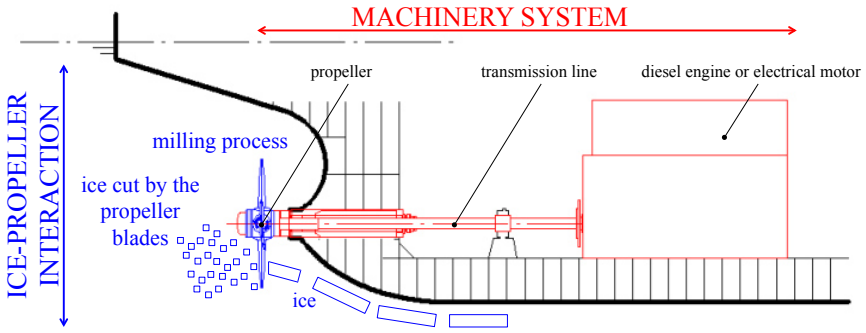

Figure 2.1: Propulsion machinery in ice (Polić *et al.*, 2014).

During the design of the propeller, it is necessary to take into consideration the blade edge impact strength, especially blade contact with multi-year hard blue ice which could result in local pressures reaching between 30 MPa to 40 MPa (Det Norske Veritas, 2011*b*). It is therefore required to strengthen blade edges and tips adequately to enable their design to withstand such contact pressures and avoid local indentations (Det Norske Veritas, 2011*b*). However, the blade still needs to be the weak part in the propulsion line in order to prevent engine damage. The bending of one blade should not lead to successive damage of any other propulsion components (Det Norske Veritas, 2011*b*). The shaft line is therefore designed for blade failure before shafting failure.

There are two main types of propellers, namely fixed pitch propeller and controllable pitch propeller (CPP) (Araujo *et al.*, 2013). CPP operates at a high power to volume ratio and therefore needs to be actuated through a hydraulic oil power system, usually a piston in a cylinder (Martelli *et al.*, 2013). CPP designs have improved efficiency for diesel or gas turbines as a result of the ability to maintain an optimum shaft speed, with provision for a wide range of thrust and load levels (Araujo *et al.*, 2013). Further benefits of CPP involve reduced space and weight as reversing gears are not required (Araujo *et al.*, 2013). The only drawback of this system compared to a fixed pitch propeller is the higher cost due to special parts such as the shafting, hydraulics and bridge controls being required (Araujo *et al.*, 2013). A diagram of the internal components of a CPP is presented in Figure 2.2.

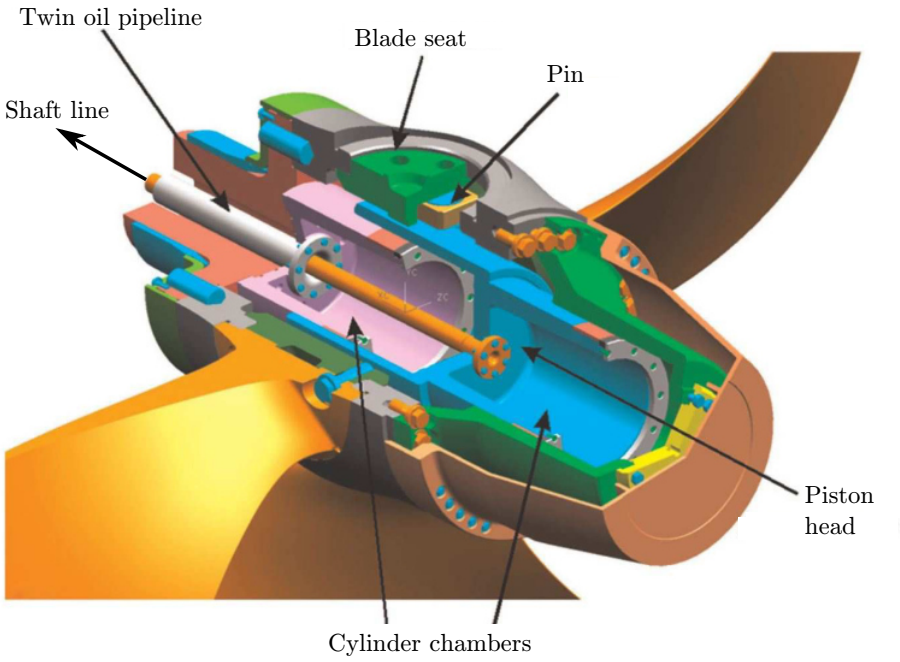

Figure 2.2: Main components inside the hub of a CPP. Adapted from Martelli *et al.* (2013).

The main components of a CPP are the tank, pumps, valves, filters, pipelines, oil distribution box, cooler, double-effect cylinder and sensors (Martelli *et al.*, 2013). Oil flows from the tank to the oil distribution box (which contains a directional valve) through a twin pipe located within the shaft and through to the propeller hub piston (Martelli *et al.*, 2013). Within the CPP hub, a double-effect hydraulic cylinder is longitudinally actuated by the pressure of the oil. Two actuating cylinder chambers are required to enable pitch adjustment of the blades by both positive and negative angles (Martelli *et al.*, 2013). The piston is connected to the blades through a pin and converts the stroke of the piston into a blade angular rotation (Martelli *et al.*, 2013).

2.2 Torsional vibration

The quantification of torsional vibration in rotating machinery is of importance to assess the possibility of damage or failure of machine components and premature fatigue failure (Kushwaha, 2012). There is also the possibility of a significant increase in the amplitude of the torsional vibration if the system operates close to its natural frequency, which results in excessive stress and

leads to component failure (Kushwaha, 2012). Torsional vibration is defined by McGraw-Hill Dictionary of Scientific & Technical Terms (2003) as '*a periodic motion of a shaft in which the shaft is twisted about its axis first in one direction and then the other; this motion may be superimposed on rotational or other motion.*'

The main source of excitation for polar class propulsion systems is attributed to propeller-ice interaction (Barro and Lee, 2011). Rules have been laid for polar class (PC) ships intended for Arctic navigation by the International Association of Classification Societies (IACS) (International Association of Classification Societies, 2016) and classification societies which encompass Korean Register (Korean Register, 2015), American Bureau of Shipping (American Bureau of Shipping, 2006), Det Norske Veritas (DNV) (Det Norske Veritas, 2011*a*), Lloyd's Register (Germanischer Lloyd, 2007) and Finnish-Swedish Ice Class Rules' Guidelines (Finnish Maritime Administration and Swedish Maritime Administration, 2005), amongst others. These regulations have been integrated to obtain the classification of ice going vessels (Barro and Lee, 2011).

2.3 Operational loads

During ice passage, the propeller is subjected to varying loads. These loads can be classified as non-contact loads, which refer to the hydrodynamic load on the blade experienced in open water conditions and contact loads, which refer to ice milling and ice impact (Barro and Lee, 2011). Ice milling can be defined as the process during which ice is trapped between the hull and the blade, wherein it becomes crushed and results in high loads, or the interaction with generally large pieces of ice (Barro and Lee, 2011). Smaller ice debris that result in more moderate loads and which are passed through the propeller are referred to as ice impacts (Barro and Lee, 2011).

An example of internal torsional vibration obtained through full-scale measurements on the shaft line of a vessel during a single propeller-ice interaction is presented in Figure 2.3, where one notices the torque fluctuates about a

mean, non-zero torque value. This non-zero value is the hydrodynamic load which can be defined as the water resistance against the rotating propeller which causes a constant torque to be induced (Ikonen *et al.*, 2014). The hydrodynamic load is presented by a dashed line in Figure 2.3.

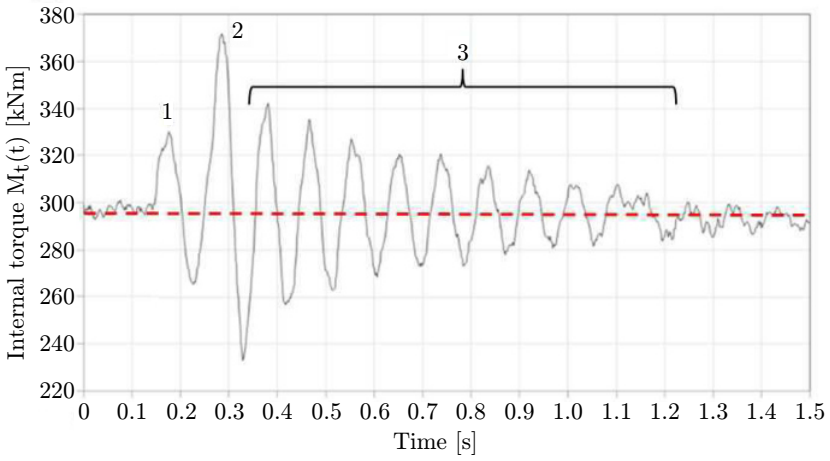

Figure 2.3: Internal torsional vibration response due to propeller-ice impacts, with the hydrodynamic load indicated with a dashed line. Adapted from Ikonen *et al.* (2014).

The rapid increase of internal torque after t = 0.15 s is due to ice-induced loading on the propeller, indicated by marker 1. During the time frame t = 0.15 s to 0.38 s multiple ice impacts may be present, resulting in the second peak (marker 2) in the response (Ikonen *et al.*, 2014). The reason for the quick deterioration of torque fluctuations (marker 3) is attributed to water damping, which causes the torque response profile to decay smoothly (Ikonen *et al.*, 2014).

Beyond a certain rotational speed, the flow pattern of water over the blades degenerates, resulting in a severe loss of thrust and physical damage over time. This phenomenon is due to cavitation (Casciani-Wood, 2015). A major concern relating to cavitation is therefore the result of thrust breakdown (Kuiper, 1997). The Encyclopædia Britannica (2016) defines cavitation as the '*formation of vapour bubbles within a liquid at low-pressure regions that occur in places where the liquid has been accelerated to high velocities.*'

During cavitation, the propeller surface is exposed to impact-like excitation resulting from a fluctuating pressure field (Casciani-Wood, 2015). According to Casciani-Wood (2015), cavitation damage is usually characterized by a strong radial pattern on the suction surface of the blades. During cavitation the most significant pressure reductions occur on the suction surface of the blade, with greater rotational speed increasing the possibility of cavitation.

Sharma *et al.* (1990) performed experiments on five model propellers and reported tip vortex cavitation to be the dominating type of cavitation, followed by side sheet cavitation. It was also observed that bubble and sheet cavitation were responsible for severe blade surface erosion as well as noise problems.

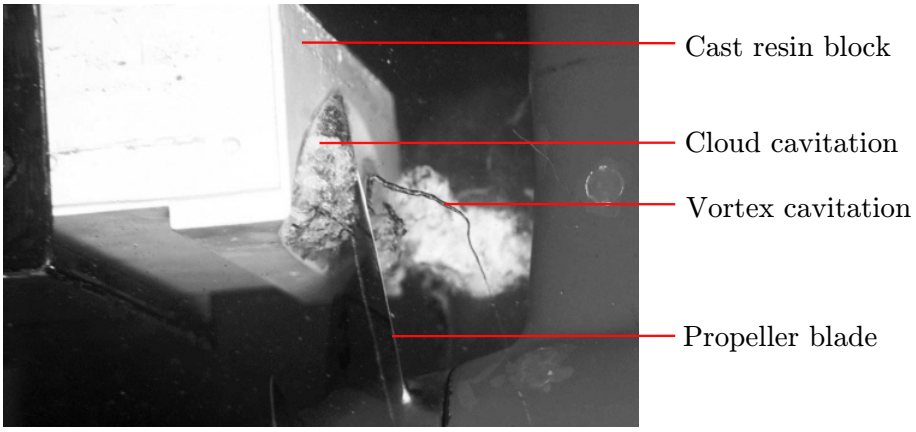

Figure 2.4: Cavitation during an ice blockage test. Adapted from Sampson *et al.* (2009).

Cavitation does not only occur in open water but has also been reported for ship passage in ice (Figure 2.4). Stable sheet and vortex cavitation develop when the blade of the propeller passes behind a piece of ice, with cloud cavitation forming as the wake of the ice-flow develops (Walker, 1996). The result is a reduction in mean forward hydrodynamic thrust as a result of propeller-ice interaction. This can cause a thirty percent increase in the aftwards directed loads on the propeller (Walker, 1996). Walker (1996) states that cavitation additionally increases the oscillation of hydrodynamic loads about their mean, inducing the propulsion system to fatigue.

2.4 Full-scale measurements

Propeller loads could ideally be determined from blade measurements (Ikonen *et al.*, 2014). However, the challenges to this approach include the interaction of the blades with the working environment as well as ice impacts that damage the sensors (Al-Bedoor *et al.*, 2006). Due to these harsh operating conditions, strain gauges are only feasible in laboratory-testing studies. These studies have demonstrated the limitations of this practical technique in terms of sensor survival (Al-Bedoor *et al.*, 2006). Besides this, the installation costs involved are high due to the requirement of cable ducting through the shaft to the propeller blades (Ikonen *et al.*, 2014). Current full-scale measurements of ice loads rely on shaft line measurements through strain gauges, which are installed between the propeller and the engine within the safety of the vessel hull. The thrust and torque of propulsion on the shaft line is then determined through an inverse problem where the propeller load is estimated through the structural transfer function between the propeller and the measurement location.

A major factor that makes the determination of the ice loads on the propeller, based on shaft measurements, difficult or impossible to determine is the dynamic response of the propulsion system. This dynamic response includes that of the engine, the shaft and the propeller (Ikonen *et al.*, 2014). Information with regards to the exact solutions of torsional vibration of a uniform shaft carrying multiple concentrated elements is rare and is one of the reasons why this problem is so often investigated (Chen, 2006).

Strain gauges are sensors that operate on the premise that the resistance in a thin wire will change proportionally to its change in length, as shown in Equation 2.1 (Hoffmann, 2001):

$$\frac{\Delta R}{R_o} = k\varepsilon \tag{2.1}$$

with

$$\varepsilon = \frac{\Delta l}{l_o} \tag{2.2}$$

They are usually placed in a Wheatstone bridge configuration, which is a

circuit capable of measuring small changes in electrical resistance. The layout of a Wheatstone bridge is presented in Figure 2.5, with the four branches of the bridge being formed by resistors (R_1 to R_4) with the output voltage (U_A) being measured between nodes 1 and 4 and the excitation voltage (U_E) measured between nodes 2 and 3.

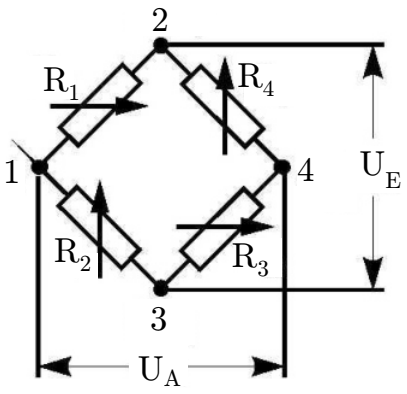

Figure 2.5: Diagram of a general strain gauge setup for a Wheatstone bridge circuit. Adapted from Hoffmann (2001).

2.5 DNV Ice Class Rules

The DNV Ice Class Rules define the requirements for varying types of vessels which are occasionally or primarily intended for navigation in ice. According to the DNV Rules, the maximum torque on a propeller due to ice influence, for a PC-5 rated vessel, can be defined as follows (Det Norske Veritas, 2011*a*):
For $D < D_{limit}$

$$Q_{ice,max} = N_1 \left(1 - \frac{d_h}{D}\right) \left(\frac{P_{0.7}}{D}\right)^{0.16} (nD)^{0.17} D^3 \tag{2.3}$$

For $D \geq D_{limit}$

$$Q_{ice,max} = N_2 \left(1 - \frac{d_h}{D}\right) (H_{ice})^{1.1} \left(\frac{P_{0.7}}{D}\right)^{0.16} (nD)^{0.17} D^{1.9} \tag{2.4}$$

with

$$D_{limit} = 1.8 H_{ice} \tag{2.5}$$

where N_1 and N_2 are equal to 14.7 and 27.93 for open propellers and 10.4 and 19.76 for ducted propellers. Det Norske Veritas (2011*a*) describes three cases

containing a sequence of blade impacts which are modelled as half sinusoidal functions. This loading profile is used to model the propeller-ice torque excitation for shaft line dynamics. The torsional excitation is described according to varying conditions as presented in Table 2.1, with Figure 2.6 displaying the torque excitation time histories.

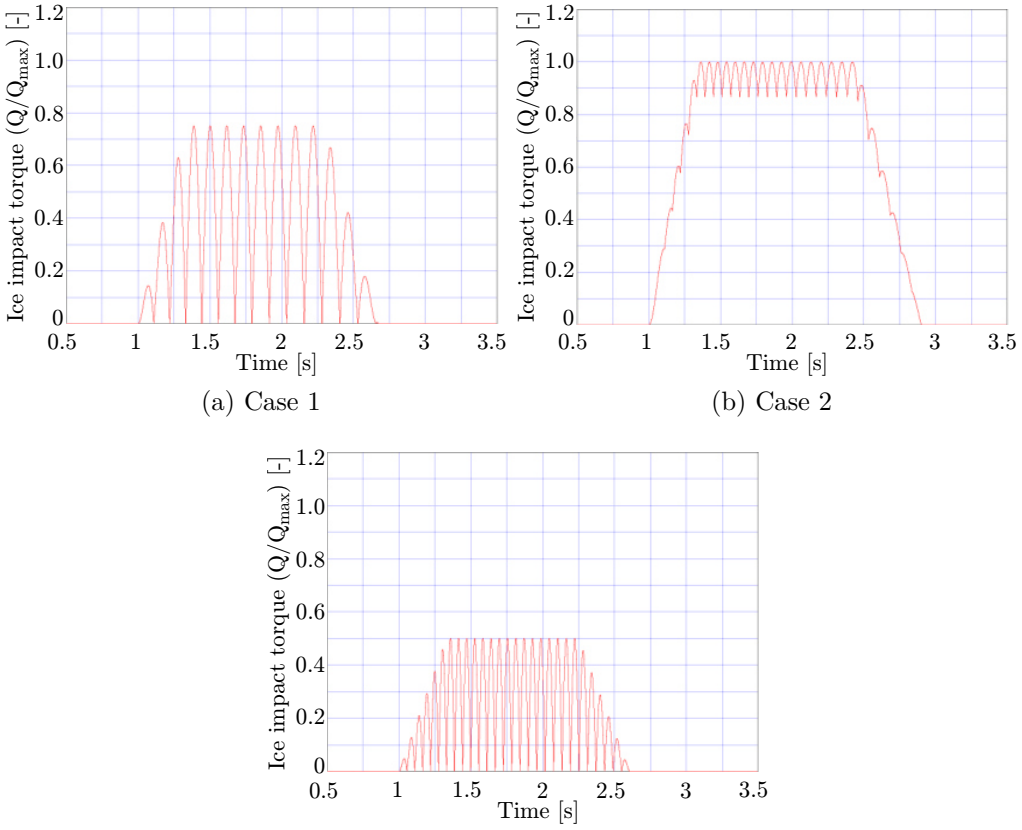

(a) Case 1

(b) Case 2

(c) Case 3

Figure 2.6: Modelled torque excitation on the propeller used for shaft line dynamic analysis. These propeller-ice interactions are for four bladed propellers during (a) 90° and (b) 135° single-blade impact sequence and (c) 45° double bladed impact sequence. Adapted from Det Norske Veritas (2011*a*).

A single blade impact can be described by a half-sine impact function which is expressed in terms of the propeller rotation angle using the C_q and α_i parameters with the maximum ice induced torque on the propeller:
For $\varphi = [0, \alpha_i]$

$$Q_{ice}(\varphi) = C_q Q_{ice,max} sin\left(\varphi \frac{180}{\alpha_i}\right) \tag{2.6}$$

For $\varphi = [\alpha_i, 360°]$

$$Q_{ice}(\varphi) = 0 \tag{2.7}$$

α_i is expressed in terms of the propeller rotation angle (degrees) versus the duration of propeller-ice interaction and C_q is defined as an empirical coefficient defining the magnitude of these impacts. Transient torsional vibration analysis should be used to determine the response torque Q_{shaft} at any component in the propulsion system through the excitation torque Q_{ice} applied at the propeller (Det Norske Veritas, 2011*a*). The excitation torque Q_{ice} needs to be superimposed on the bollard condition hydrodynamic torque when performing calculations for all three cases.

Table 2.1: Torque excitation parameters for different ice cases (Det Norske Veritas, 2011*a*).

Torque excitation	Ice-propeller interaction	C_q	α_i
Case 1	Single ice block	0.75	90°
Case 2	Single ice block	1	135°
Case 3	Two ice blocks	0.5	45°

Det Norske Veritas (2011*a*) also describes the maximum forward and backward ice induced forces allowed on the propeller. These ice induced forces on the blades can be translated to shaft line thrust at the propeller by multiplying the blade forces by a factor of 1.1 (Det Norske Veritas, 2011*a*). For the backward bending case:

when $D < D_{limit}$

$$F_b = N_3 S_{ice} \left[nD\right]^{0.7} \left[\frac{EAR}{Z}\right]^{0.3} D^2 \tag{2.8}$$

when $D \geq D_{limit}$

$$F_b = N_4 S_{ice} \left[nD\right]^{0.7} \left[\frac{EAR}{Z}\right]^{0.3} \left[H_{ice}\right]^{1.4} D^{N_5} \tag{2.9}$$

with $D_{limit} = 0.85[H_{ice}]^{1.4}$ for open propellers, $D_{limit} = 4H_{ice}$ for ducted propellers and EAR being the expanded area ratio of the blades. For the forward bending case:

when $D < D_{limit}$ for open propellers and $D \leq D_{limit}$ for ducted propellers

$$F_f = 250 \left(\frac{EAR}{Z}\right) D^2 \tag{2.10}$$

when $D \geq D_{limit}$ for open propellers and $D > D_{limit}$ for ducted propellers

$$F_f = 500 \left(\frac{1}{1 - \frac{d_h}{D}} \right) H_{ice} \left(\frac{EAR}{Z} \right) D \tag{2.11}$$

with

$$D_{limit} = \left(\frac{2}{1 - \frac{d_h}{D}} \right) H_{ice} \tag{2.12}$$

where N_3, N_4 and N_5 are equal to 27, 23 and 1 for open propellers and 9.5, 66 and 0.6 for ducted propellers.

2.6 Fatigue

A concern related to dynamic structures is the effect of fatigue. Fatigue is one of the most common causes of damage to metallic structures and can be defined as a degradation process under cyclic loading (Connor *et al.*, 2010). A reliable method of fatigue life estimation is required for the future design of dynamic structural systems. During propeller exposure to a spectrum of maximum ice loads, as defined by the ice rules, the safety factor for the influenced parts against fatigue is specified to be 1.5 according to Miner's rule (Det Norske Veritas, 2011*b*). Palmgren-Miner's rule is used to estimate the cumulative damage ratio of a section of the component of interest and is expressed as the accumulated damage at different stress levels from each load cycle, independent of their sequence (Det Norske Veritas, 2011*b*). The damage ratio (MDR) represents the ratio of the component's used life, with failure due to fatigue occurring when this damage ratio exceeds one (Det Norske Veritas, 2011*b*):

$$MDR = \sum_{z=1}^{I} \frac{n_z}{N_z} \leq 1 \tag{2.13}$$

with

$$n_z = (ZN_{ice})^{1-\left(1-\frac{z}{I}\right)^{k_w}} - \sum_{z=1}^{z} n_{z-1} \tag{2.14}$$

$$N_{ice} = k_1 k_2 N_{class} n \tag{2.15}$$

$$k_2 = 0.8 - f_z \quad for \quad f_z < 0 \tag{2.16}$$

$$k_2 = 0.6 - 0.2 f_z \quad for \quad 1 < f_z \leq 2.5 \tag{2.17}$$

$$f_z = \frac{h_o - H_{ice}}{D/2} - 1 \tag{2.18}$$

It is required to design the propulsion line components with sufficient strength to withstand the maximum induced loads on the propeller as described by Equation 2.3 and 2.4. At the same time, damage to other propulsion line components is to be prevented in the event of plastic bending of a propeller blade (Det Norske Veritas, 2011*a*). Furthermore, fatigue strength is to accommodate the load distribution (Equation 2.19) which is presented as an accumulated load spectrum in Figure 2.7 (Det Norske Veritas, 2011*a*).

$$Q_A(N) = Q_{A,max}\left[1 - \frac{log(N)}{log(ZN_{ice})}\right]^{1/k_w} \tag{2.19}$$

where Q_A is the response torque amplitude on the shaft during a sequence of ice impacts on the propeller and $Q_{A,max}$ is the highest response torque amplitude on the shaft during a sequence of ice impacts on the propeller.

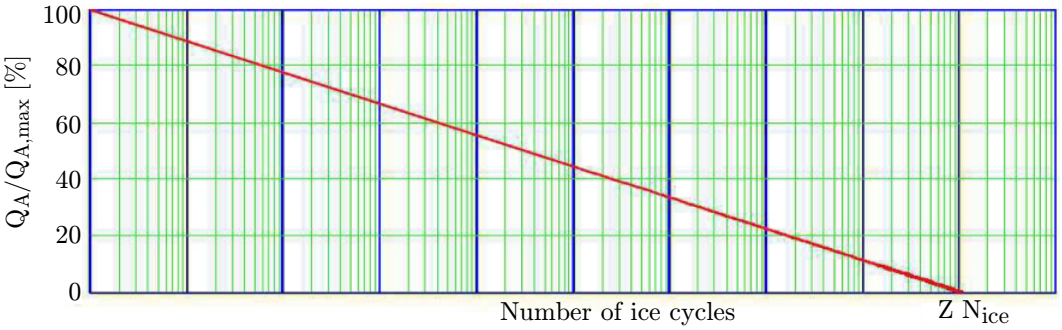

Figure 2.7: Total number of load cycles in the load spectrum. Adapted from Det Norske Veritas (2011*a*).

Cycle counting is a convenient method to summarize irregular loading histories by determining the number of times certain cycles of various magnitudes occur (ASTM International E1049-85, 2011). Many different cycle counting methods, of which level-crossing counting, peak counting, simple-range counting and rainflow counting are the most well known (ASTM International E1049-85, 2011). Of these methods, rainflow counting has been proven to be the better method for irregular loads (Connor *et al.*, 2010). Rainflow counting was also used by Myklebost and Dahler (2013) during the analysis of shaft line torque. Rainflow counting enables one to extract cycles from randomly loaded data, with amplitudes defined as half the difference between two consecutive peaks and troughs.

The propulsion system of a vessel is exposed to a wide spectrum of loads during operation. Only the dominating cases are considered during fatigue analysis as loads below the maximum continuous rating (MCR) in bollard condition theoretically do not result in shaft line failure, with MCR defined as the maximum rated torque Q_{MCR} the propulsion system can safely operate continuously (Det Norske Veritas, 2011*b*). Figure 2.8 represents the typical load cases that need to be assessed for vessels navigating in ice with a directly coupled two-stroke plant. $Q_{shaft,ice,peak}$ is the highest response peak torque measured in the shaft due to ice impacts on the propeller, $Q_{shaft,ice,ave}$ is the average torque in the shaft during an ice milling sequence, $Q_{shaft,o}$ is the shaft torque at maximum continuous power in bollard condition, $Q_{shaft,ice}$ is the response torque in the shaft due to ice impacts on the propeller and Q_{shaft} is the total torque response in the shaft due to external loading on the propeller.

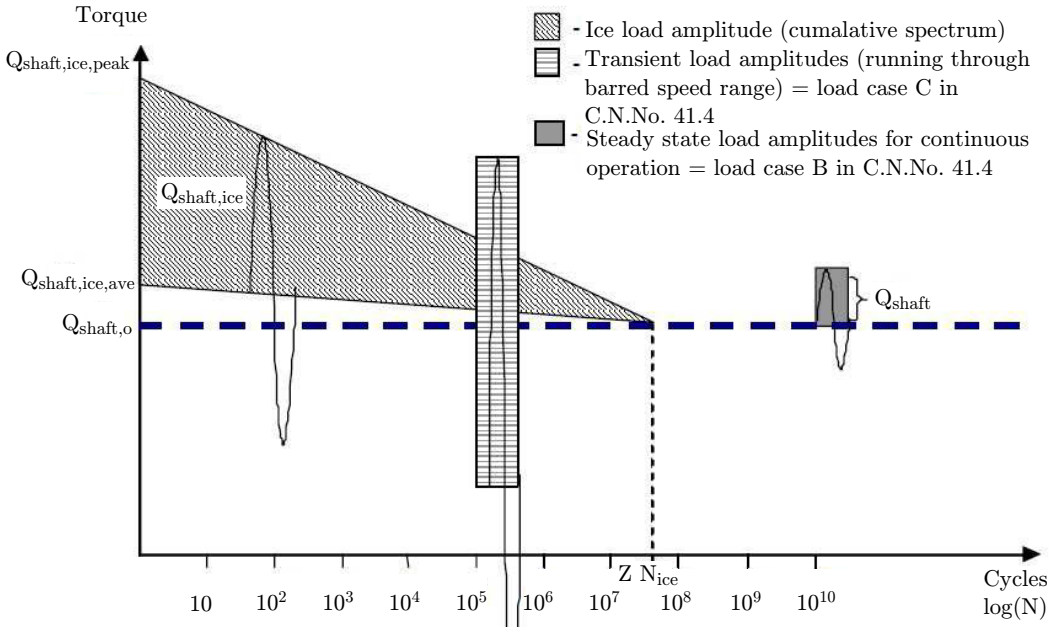

Figure 2.8: Typical load cases to be assessed for directly coupled two-stroke plant ice class vessels. Adapted from Det Norske Veritas (2011*b*).

2.7 Methods

Successful ice-going propulsion plant designs require the quantification of ice impacts. It is not always possible to measure these impact loads directly

on the propeller due to limitations of space in the propeller hub and of the current measurement equipment (Polić *et al.*, 2014). Therefore these loads are determined indirectly through measurements of the shaft line dynamic response (Polić *et al.*, 2014). This leads to the indirect force estimation approach whereby the input force is determined from indirect measurements on the shaft (Jacquelin *et al.*, 2003). This type of problem has been investigated through the frequency domain (Doyle, 1987; Gao and Randall, 1999) and time domain (Ikonen *et al.*, 2014; He and Du, 2010) approach. For forced harmonic excitation of the shaft line (open water), the frequency domain approach can be used (Batrak, 2010). However, for impact loading on the propulsion system with transient torsional vibration (ice-infested water), the time domain approach should be used (Batrak, 2010).

The successful determination of propeller loading from shaft line measurements depend on the blade angle, excitation amplitude, torsional rigidity of the shaft and the drive mass moment of inertia (Al-Bedoor *et al.*, 2006). Al-Bedoor *et al.* (2006) used a mathematical model to simulate the feasibility of determining rotating blade vibration from the torsional vibration of the shaft. The results from this study confirmed blade vibration signatures to be detectable from shaft line torsional vibration and proving the feasibility of shaft line measurements.

2.7.1 Lumped mass model

To determine propeller loads from shaft line measurements, the transfer function between the externally induced loads and the internal shaft line measured torque is to be determined. One of the most commonly used methods in torsional vibration analyses is the lumped mass model which represents propulsion components as polar moments of inertia. Connecting shafts are modelled as torsional spring elements. Examples include studies by Ikonen *et al.* (2014), He and Du (2010) and Det Norske Veritas (2011*a*) who presented lumped mass models of shafts for dynamic analysis.

Torsional vibration calculations form the basis of the mass-elastic shaft line models. Time is incremented in a step-wise fashion to allow for numer-

ical integration of differential equations. This step time should not exceed the highest natural frequency period by more than 5% for numerical stability reasons (Det Norske Veritas, 2011*a*). It is therefore strongly advised by Det Norske Veritas (2011*a*) to use a minimum number of lumped masses to simplify the model. The simplification process aims at maintaining a constant inertia, maintaining the lower natural frequencies, minimising computer calculation time and avoiding numerical challenges presented by local high-frequency vibrations (Det Norske Veritas, 2011*a*).

The complete mechanical form of the governing equation for a mass-damper system with non-linearities in matrix element is provided by the following equation (Batrak *et al.*, 2012):

$$J\ddot{\theta} + C\dot{\theta} + K\theta = Q(t) \tag{2.20}$$

where J is the polar moment of inertia, C the damping, K the rigidity, Q the generalized excitation torque vector and θ the angular displacement vector of the twisting angles at the system nodes. This is the general equation used to solve transient torsional vibration problems (Batrak *et al.*, 2012).

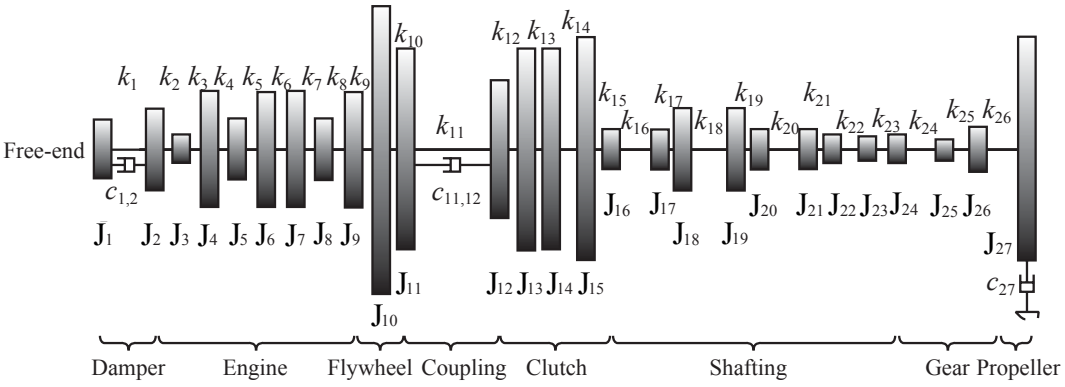

Figure 2.9: Marine propulsion shafting lumped parameter model. Apdapted from Tang and Brennan (2013).

A simplified lumped mass model of a marine propulsion shafting system is presented in Figure 2.9. This specific model consists of twenty-seven lumped masses, with J_i presenting the polar mass moments of inertia, c_i the external damping coefficients, $k_{i,i+1}$ the torsional stiffness and $c_{i,i+1}$ the internal damping coefficients of the shaft (Tang and Brennan, 2013). This model was

used to analyse the free torsional vibration characteristics and forced torsional vibration response of the propulsion system. This was done to investigate the phenomenon of numerical predictions and experimental torsional vibration stress curves that vary throughout the shafting system.

2.7.2 Reverse model

Polić *et al.* (2014) used a different method in which the measured ice-related response of the shaft was linked to that of the ice-propeller load. This was achieved through collecting the shaft response and filtering it with a different sampling frequency, followed by the conversion to the ice-propeller load using a reverse model of the propulsion machinery.

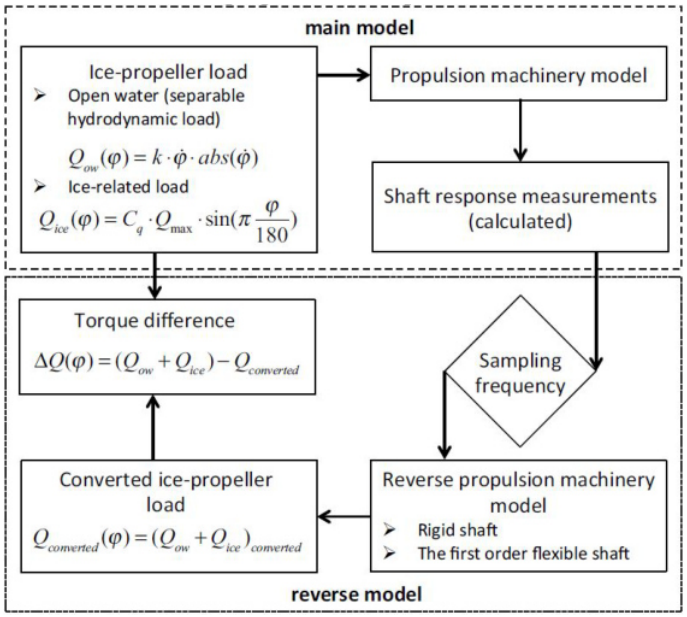

Figure 2.10: Overview of transformation procedure involving the reverse model (Polić *et al.*, 2014).

This process consists of six steps: (1) Rule-based DNV ice-propeller load is determined and applied to the propulsion machinery model. (2) Bond graph methodology is used to create a simple model consisting of the propeller, transmission line and engine. (3) Rule-based load is used to simulate the propulsion machinery response. (4) Shaft response is collected at certain locations. (5) Conversion of shaft response back into the ice-propeller load through the reverse model. (6) Obtained ice-propeller load is compared to the original rule

based ice-propeller load (Polić *et al.*, 2014). An overview of this transformation procedure is provided in Figure 2.10, where Q_{ow} denotes the open water torque, Q_{ice} denotes the torque induced by ice impact, $Q_{converted}$ denotes the converted torque and k denotes the linear viscous damping. The bond graph method describes the energy flow and power transfer between and within the sub-element components, as presented in Figure 2.11 (Polić *et al.*, 2014).

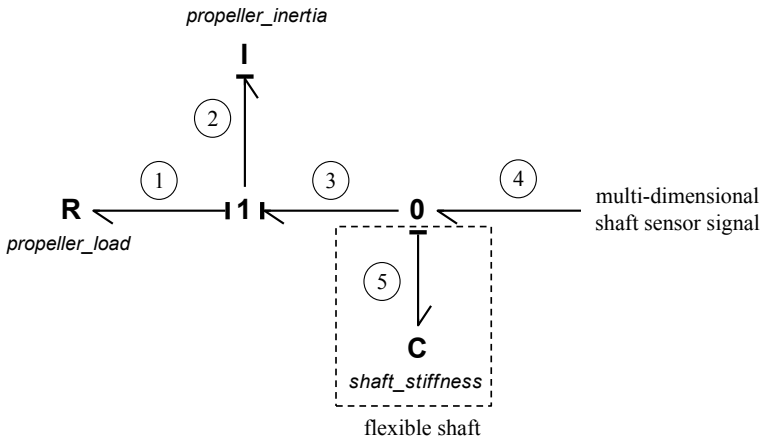

Figure 2.11: Bond graph representation of the reverse model (Polić *et al.*, 2014).

This method was however proven to require further research as the most suitable sampling frequency and the inter-dependencies with natural frequencies have not been identified. Furthermore, the dependency of the transmission design, engine load and ice-propeller load on the sample frequency needs further investigation and the flexible shaft model requires further development (Polić *et al.*, 2014).

Based on the present research, it was decided to use the lumped mass model approach. This model was used in conjunction with the governing equation of torsional vibration and Newmark-Beta method to determine the response of the structure. Regularization methods were verified and implemented on shaft torque data obtained from the SA Agulhas II (SAA II) during the 2015/2016 voyage to Antarctica. The examination of ice induced loading on the propeller was limited to moments acting about the shaft line axis.

Chapter 3

Full-scale measurements

Full-scale measurements were performed on the polar supply and research vessel (PSRV) SAA II and Polarstern. The port side shaft of each vessel was instrumented with strain gauges to determine the dynamic torque and thrust in the shaft. The rationale was that models of the structural transmissibility would be used to determine the effective ice loads on the propeller. Accelerometers were installed along the shaft line at the bearing supports in order to obtain additional data that could complement the strain gauge data. Machine control data was also recorded for the SAA II by the on-board computer and could be utilized in conjunction with the torque, thrust and accelerometer data. The only relative data available for the Polarstern was vessel speed, navigation and ocean data.

3.1 Voyage and vessel

The SAA II (Figure 3.1) was manufactured in Rauma shipyard in 2012 by STX Finland (Ikonen *et al.*, 2014). The shaft line was permanently instrumented with strain gauges during the construction phase to determine ice loads through indirect measurements (Kujala *et al.*, 2014). The hull was strengthened in accordance with DNV ICE-10 and the vessel classified to Polar Ice Class PC-5 (Kujala *et al.*, 2014). She is therefore rated for year-round operations in medium first-year ice containing old ice inclusions (International Association of Classification Societies, 2016). She is driven by four 3 MW diesel generators

that power two Conver Team electric motors of 4.5 MW each. She is equipped with two four-bladed variable pitch propellers with individual shaft lines (STX Finland Oy, 2012).

Figure 3.1: SAA II vessel instrumented during the 2014/2015 and 2015/2016 voyages to Antarctica.

The Polarstern (Figure 3.2) was manufactured during 1982 in Kiel by Howaldtwerke-Deutsche Werft AG and outfitted by Werft Nobiskrug GmbH in Rendsburg (The Alfred Wegener Institut, 2016). The hull was strengthened in accordance with Germanischer Lloyd Ice Class E3, which is the equivalent of Polar Ice Class PC-5 (Transport Safety Agency, 2010). The Polarstern therefore has the same rating as the SAA II. She is driven by four diesel engines, each of 3.5 MW, which in turn powers two shaft lines with variable pitch propellers.

Figure 3.2: Polarstern vessel instrumented during the PS100 2016 voyage to the Arctic.

The difference between the Polarstern and the SAA II is that the Polarstern has ducted propellers as well as direct diesel engine drive through a gearbox compared to the SAA II which has open propellers and diesel to electric drive to the shaft line (Figure 3.3). The specifications of the vessels are presented in Table 3.1.

Table 3.1: Vessel specifications (STX Finland Oy, 2012; The Alfred Wegener Institut, 2016).

	SA Agulhas II	FS Polarstern
Gross tonnage	12 897 tons	12 614 tons
Length	134 m	118 m
Breadth	22 m	25 m
Classification	DNV	Germanischer Lloyd
Class notation	1A1 PC-5/ICE-10	100 A5 ARC 3
Yard	STX Finland	Howaldtswerke-Deutsche
Location	Rauma, Finland	Hamburg & Kiel, Germany
Year built	2012	1982
Main engine maker	Wärtsilä	Klöckner-Humboldt-Deutz
Diesel engine type	6L32	KHD RBV 8 M 540
Electric motor type	N3 HXC 1120 LL8	-
Speed (n) at MCR	140 rpm	182.4 rpm
Power (P_D) at MCR	4500 kW	7765 kW
Nominal torque (Q_{MCR})	307 kN · m	407 kN · m
Propeller maker	Rolls-Royce	Vereinigte Edelstahlwerke
No. of blades/Diameter	4/4.3 m	4/4.2 m
Shaft characteristics	Direct drive	1:3.563 gearbox ratio
No. of motors/ propellers	2/2	4/2

(a) SAA II propeller (b) Polarstern propeller

Figure 3.3: Pictures of the (a) SAA II (Ship Year, 2013) and (b) Polarstern (Grobe and Alfred Wegener Institute, 2007) port side propeller.

3.1.1 SAA II Antarctic voyages

During the 2014/2015 and 2015/2016 voyage on-board the SAA II from Cape Town to Antarctica, torque, thrust, machine control, radial bearing vibration and navigation data was measured. The global positioning system (GPS) track of the voyages is presented in Figure 3.4. During the 2015/2016 voyage:

- The vessel departed Cape Town harbour (1) on 5 December 2015 and headed towards the Greenwich Meridian, along which she navigated to Antarctica (3) to allow oceanographers to collect samples.
- Ice was encountered on 11 December 2015 and continued until 16 December when she arrived at the shelf, Penguin Bukta (3).
- On 22 December she navigated to Akta Bukta near the German Antarctic Research Station, Neumayer.
- From Akta Bukta she headed through heavy pack ice towards the South Sandwich Islands and arrived at South Thule (4) on 24 December.
- After South Thule, she navigated out of the ice field and reached South Georgia (5) on 30 December 2015. Her journey back to Antarctica started on the same day, during which whale observations were performed.
- She re-encountered ice on 11 January on route to Penguin Bukta (3), where seal tagging was conducted.
- The voyage back to Cape Town started on 1 February. She left the ice field on 2 February and arrived in Cape Town on 11 February 2016.

For the 2014/2015 voyage, the route travelled was similar except that the vessel stopped at Bouvet Island during the outbound voyage to drop off scientists and supplies by helicopter. The vessel spent 119 hours manoeuvring through thick ice in 2014/2015 voyage compared to 126 hours during the 2015/2016 voyage, where the difference can be attributed to the extra time spent navigating through the ice field in search of Ross seals for seal researchers.

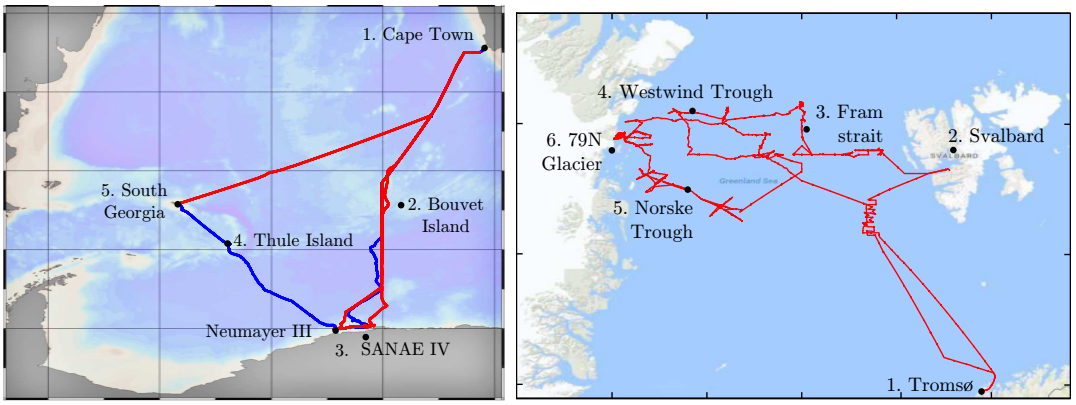

(a) Antarctic voyage (b) Arctic voyage

Figure 3.4: Round voyage for (a) SAA II to Antarctica (Red - outbound, blue - return voyage) and (b) Polarstern to the Arctic. Background for Antarctica adapted from AWI (2015) and for Arctic from Google (2016).

3.1.2 Polarstern Arctic voyage

During the 2016 Arctic voyage on-board the Polarstern, torque, thrust, radial bearing vibration, vessel speed and navigation were measured. The GPS track of the voyage is presented in Figure 3.4 and the route described as follows:

- The Polarstern departed Tromsø (1), Norway, on 18 July 2016 and headed directly for Svalbard (2) where she arrived on 21 July at Longyearbyen.
- She left Svalbard on the same day and headed West North West towards the zero degree meridian line in order to sail along the Fram Strait (3).
- The first encounter with ice was on 29 July. She voyaged along the zero meridian to just below 81 degrees North on 31 July.
- The voyage continued Westwards towards the Westwind Trough (4). Ice conditions became less concentrated.
- On 4 August she headed South and exited the ice field on 8 August. She continued to the Norske Trough (5) during which she re-encountered significant ice on 14 August.

- She steered towards the 79 North Glacier (6) at Greenland during which glaciologists performed a Bathymetry survey for coring purposes from 21 to 29 August.
- On 30 August she left the ice field, after which she headed back to Tromsø (1) and arrived at port on 6 September 2016.

The total duration of the voyage was 51 days, of which an estimated 70 hours was spent navigating in thick Arctic ice.

3.2 Instrumentation

Strain gauges were installed on the SAA II and Polarstern shaft line to measure torque and thrust loading. These strain gauges were placed in a Wheatstone bridge configuration to reject axial strain, compensate for temperature variations and reject bending strain. This was achieved by installing the T-rosette strain gauges in pairs on either side of the shaft line for the thrust measurements. The torque strain gauges were inclined at $\pm 45°$ to the centreline of the shaft to determine the maximum shear stress on the surface of the shaft (Figure 3.5a).

3.2.1 Strain measurements

The general equation used for a full Wheatstone bridge configuration is (Hoffmann, 2001):

$$\frac{U_A}{U_E} = \frac{k}{4}(\varepsilon_1 - \varepsilon_2 + \varepsilon_3 - \varepsilon_4) \tag{3.1}$$

When clockwise torque is applied, strain gauge number 2 and 4 will sense negative torque and strain gauge 1 and 3 will sense positive torque. Thus the absolute value of all strains (ε_1 to ε_4) will be the same and Equation 3.1 can be reduced to (Hoffmann, 2001):

$$\frac{U_A}{U_E} = k\varepsilon \tag{3.2}$$

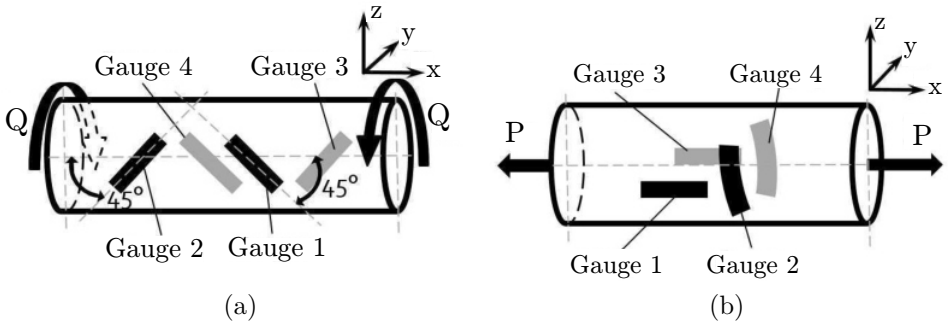

Figure 3.5: Strain gauge placement on shaft for (a) torque and (b) thrust measurements. Adapted from Hoffmann (2001).

Torque and shear strain can be related through substitution of the following equations (Hibbeler, 2011):

$$\tau = G\gamma_s \tag{3.3}$$

$$\tau = \frac{Q_{shaft} d_o}{2S_p} \tag{3.4}$$

$$\frac{\gamma_{s,max}}{2} = \sqrt{\left(\frac{\varepsilon_x - \varepsilon_y}{2}\right)^2 + \left(\frac{\gamma_{xy}}{2}\right)^2} \tag{3.5}$$

$$G = \frac{E}{2(1+\nu)} \tag{3.6}$$

$$S_p = \frac{\pi(d_o^4 - d_{in}^4)}{32} \tag{3.7}$$

where ε_x is the normal strain along the shaft axis, ε_y the normal strain perpendicular to the shaft axis and γ_{xy} the relative shear strain. When the strain gauges are aligned at 45° to the shaft axis, ε_x and ε_y measure the same but opposite magnitude with no shear strain. This becomes a case of principal strain whereby γ_{xy} is equal to zero and Equation 3.5 can be simplified to:

$$\frac{\gamma_{s,max}}{2} = \varepsilon \tag{3.8}$$

The above equations can be combined to obtain torque from the Wheatstone bridge output voltage:

$$Q_{shaft} = U_A \frac{\pi E(d_o^4 - d_{in}^4)}{16 U_E k d_o (1+\nu)} \tag{3.9}$$

For the thrust measurements, two T-rosette pairs were used together to form a full bridge, as presented in Figure 3.5b. The ratio of the output voltage to the input voltage for thrust loading includes the axial strains as well as the transverse deformation which is governed by Poisson's ratio (Hoffmann, 2001):

$$\frac{U_A}{U_E} = \frac{k}{4}[\varepsilon_1 - (-\nu\varepsilon_1) + \varepsilon_3 - (-\nu\varepsilon_3)] \tag{3.10}$$

As bending strain is rejected and the rig is temperature compensated, the axial strains (ε_1 and ε_3) are equal, thus Equation 3.10 can be simplified to:

$$\frac{U_A}{U_E} = \frac{k}{2}\varepsilon(1+\nu) \tag{3.11}$$

To determine the thrust induced by the propeller on the shaft line, the following equations are used (Hibbeler, 2011):

$$\sigma_s = E\varepsilon \tag{3.12}$$

$$T_{shaft} = \sigma_s A \tag{3.13}$$

$$A = \frac{\pi(d_o^2 - d_{in}^2)}{4} \tag{3.14}$$

The thrust can be obtained from the T-rosette Wheatstone bridge output voltage:

$$T_{shaft} = \frac{U_A E\pi(d_o^2 - d_{in}^2)}{2U_E k(1+\nu)} \tag{3.15}$$

Torque and thrust were measured on the port side intermediate shaft line using pre-installed KYOWA strain gauges during the 2014/2015 voyage on-board the SAA II. These strain gauges were located 25.2 m from the propeller's center of gravity on the aft-side of the thrust bearing. A Manner Telemetry System was used to transmit the strain gauge signals on the shaft to a digital recorder at a sample frequency of 500 Hz (Manner Sensortelemetrie, 2012). This system consists of a rotor antenna and stator that uses a non-contact induction procedure to transfer the measurement data from the shaft line, as presented in Figure 3.6.

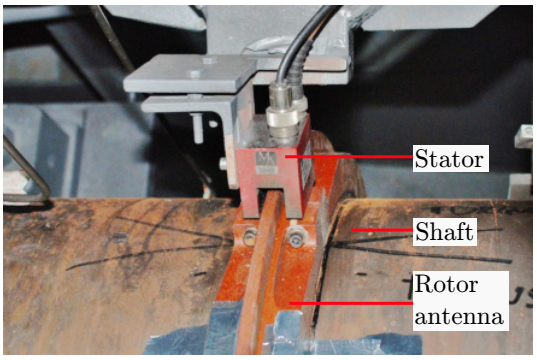

Figure 3.6: Rotor antenna and stator installed on the port side intermediate shaft line.

However, the data from the Manner Telemetry system was questionable. A supplementary V-link lossless extended range synchronized (LXRS) system, produced by LORD MicroStrain, was installed on the SAA II to validate the data. The Manner Telemetry system was later proven to be unreliable through analytical calculations, machine control data and through comparison to the V-link data. These tests are documented in Appendix A. The V-link system was used to record strain on the shaft lines of the SAA II, during the 2015/2016 Antarctic voyage, and on the Polarstern during the 2016 Arctic voyage. This system is similar to the Manner Telemetry system in that it transmits strain data wirelessly from the strain gauges on the shaft to a data acquisition system. The Manner Telemetry system uses a non-contact induction procedure where the V-link uses wireless fidelity (Wi-Fi), presented in Figure 3.7a.

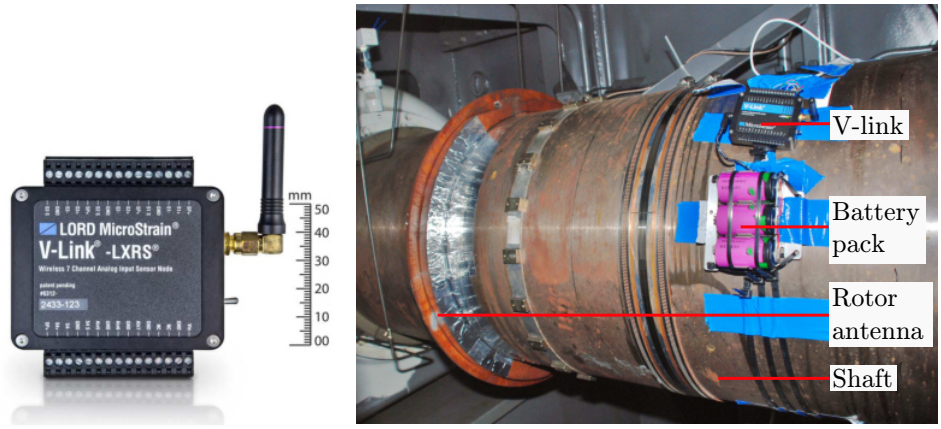

(a) (b)

Figure 3.7: Illustration of (a) V-link device (LORD MicroStrain sensing systems, 2015) and (b) measurement setup on shaft line of the SAA II.

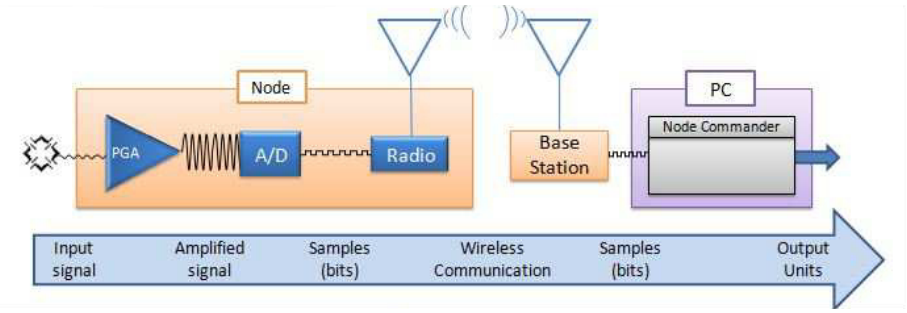

Figure 3.8: Diagram illustrating the procedure for transmitting data from the shaft to the data acquisitioner (PC - personal computer, PGA - Programmable Gain Amplifier) (LORD MicroStrain sensing systems, 2015).

The V-link system (Figure 3.7b) has been set up accordingly: the full-bridge strain gauges transmit a voltage output to the V-link that is also attached to the shaft. The V-link then uses an analog-to-digital (A/D) converter in order to transmit this data wirelessly through Wi-Fi to a WSDA-Base data gateway. The WSDA-Base is managed through Node Commander software and is connected to a Hottinger Baldwin Messtechnik (HBM) Quantum which then converts the digital signal to strain using a scale obtained from calibrating the node. A diagram illustrating this procedure is provided in Figure 3.8.

The shaft line dimensions for the SAA II were obtained from engineering drawings by STX Finland Oy (2012). The material specifications were sourced from Rolls-Royce AB (2010*c*) which provided parameters for numerical calculations during the propulsion system design phase. Polarstern shaft line dimensions were obtained from engineering drawings by Werft Nobiskrug GmbH (1980) and the material properties from Germanischer Lloyd (1981) during the test certificate of the materials. As the Polarstern was built in 1982, old German material specifications were used. Therefore the new equivalent classification was obtained. This was achieved from Metallurgica Veneta (2004) catalogue, in which the new material grade equivalent for St52-3N was found to be S355J2. The dimensions, material properties and shaft related variables for the two vessels are presented in Table 3.2. Variable h_o was not directly obtainable from engineering drawings and had to be extracted from scaled vessel drawings.

Table 3.2: Shaft line dimensions, material properties and shaft related variables for measurement location (STX Finland Oy, 2012; Rolls-Royce AB, 2010*c*; Escher Wyss, 1980; Metallurgica Veneta, 2004; Det Norske Veritas, 2011*a*).

Description	Symbol	SA Agulhas II	FS Polarstern
Modulus of elasticity	E	210 GPa	220 GPa
Shear modulus	G	81 GPa	84 GPa
Outer diameter	d_o	0.5 m	0.39 m
Inner diameter	d_{in}	0.175 m	0.213 m
Hub diameter	d_h	1.32 m	1.60 m
Max ice thickness	H_{ice}	2.0 m	2.0 m
Ice strength index	S_{ice}	1.1 m	1.1 m
Pitch at 0.7·radius	$P_{0.7}$	5.15 m	4.42 m
Expanded blade area ratio	EAR	0.51	0.55
Depth of propeller centerline	h_o	3.75 m	6.92 m

3.2.2 SA Agulhas II

Torque and thrust were measured on the port side intermediate shaft line using HBM strain gauges placed in a full bridge and T-rosette configuration. The configurations were such that they rejected bending and temperature variations of the shaft. These strain gauges were located 25.9 m from the propeller's center of gravity, as presented in Figure 3.11a.

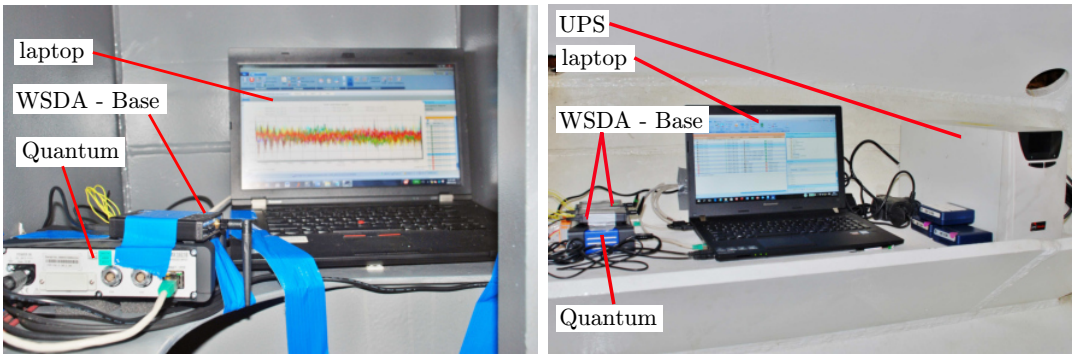

(a) (b)

Figure 3.9: Setup for shaft line data collection for (a) SAA II and (b) Polarstern. (UPS - uninterruptible power supply).

In addition to the strain gauge measurements on the shaft line, accelerometers were mounted at three locations on the shaft support structures. Three

accelerometer sets were installed on the available shaft support structures. The orientation of the accelerometers is indicated in Figure 3.11a. The specifications of the accelerometers used are provided in Table B.1. Data was acquired through a HBM Quantum mobile data acquisition system, transmitted to a laptop via an ethernet cable and recorded through Catman AP V3.5 software at a sample rate of 600 Hz (Figure 3.9a).

3.2.3 FS Polarstern

Similar measurements were performed on the Polarstern as for the SAA II, with the measurement rig presented in Figure 3.9b. The power source in the shaft line room was directly from the generator, resulting in unstable power. An uninterruptible power supply was therefore used to filter out harmful peaks which could potentially damage the equipment. The difference between the SAA II and Polarstern rigs is that additional torque measurements were performed on the Polarstern shaft line. Two sets of accelerometers were installed on the Polarstern due to limitations in the available shaft support structures within the intermediate shaft line room. One x-direction measurement was recorded as it was noted the bearings on which accelerometer measurements were performed are radial bearings that do not transfer axial vibration well. The details of the accelerometers used are presented in Table B.2 and the shaft line instrumentation in Figure 3.11b.

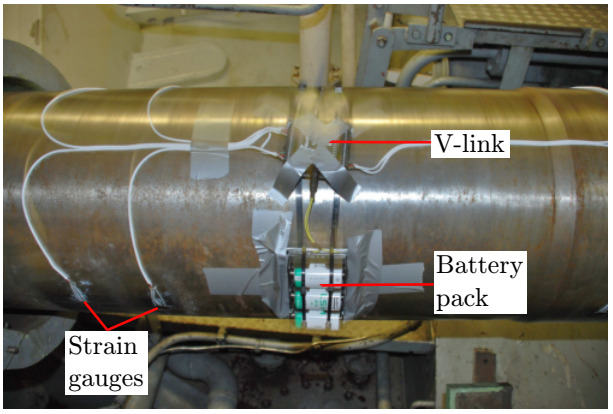

Figure 3.10: Strain gauge setup on Polarstern intermediate port side shaft.

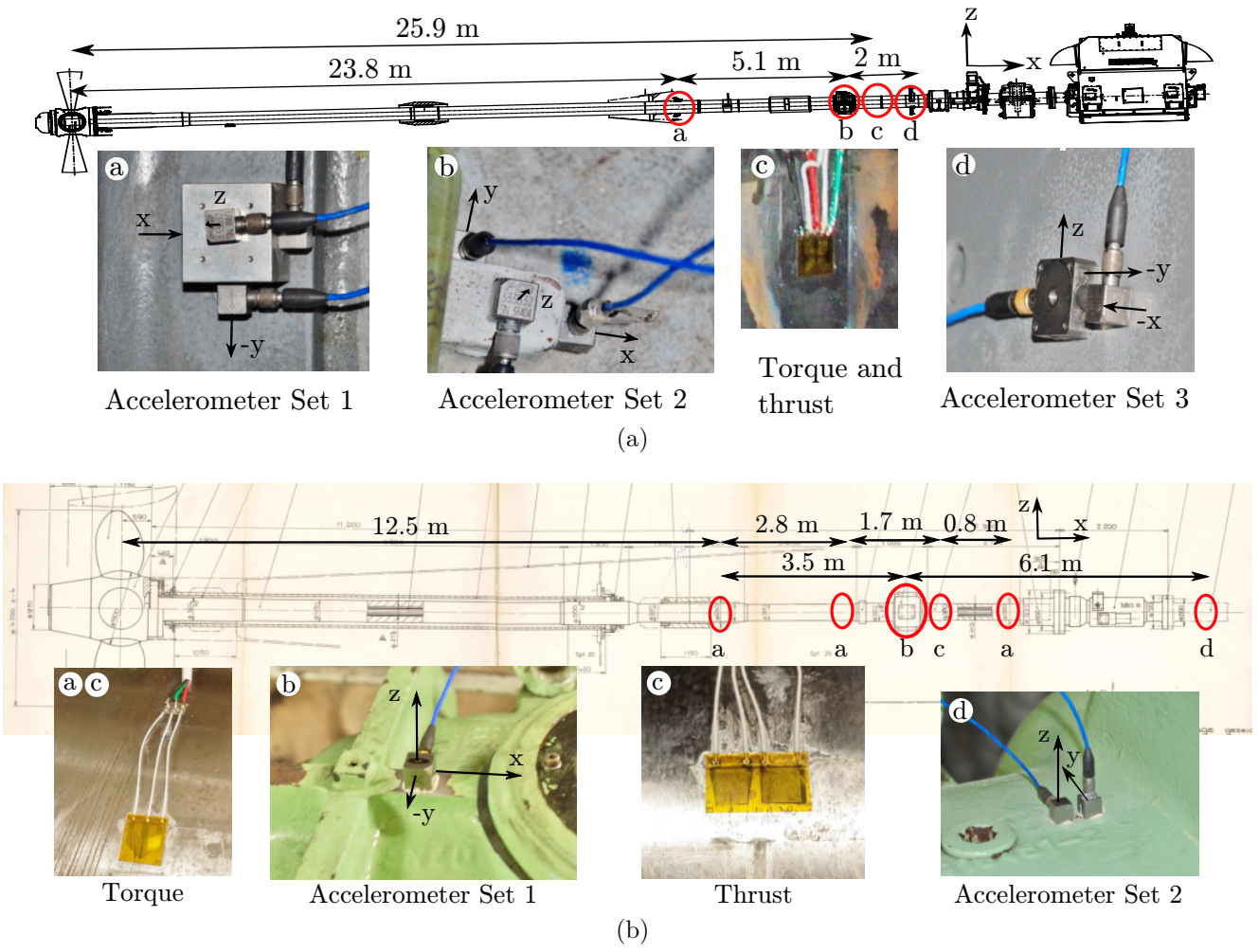

Figure 3.11: Accelerometers and strain gauges mounted along the shaft line for the (a) SAA II (Adapted from STX Finland Oy (2012)) and for the (b) Polarstern (Adapted from Werft Nobiskrug GmbH (1980)).

Chapter 4

Sample data analysis

Rainflow counting was implemented to obtain an overall representation of the significant dataset. Case studies were selected from ice navigation, open water and cavitation and compared for further insight. Lastly, the maximum torque and thrust conditions were investigated.

4.1 Rainflow counting algorithm

Rainflow counting was performed on the recorded torque and thrust shaft line data, obtained from the SAA II and Polarstern, through peak and amplitude cycle counting. It is required to first identify the turning points of the data signals using an algorithm (`sig2ext.m`) written by Nieslony (2003), with the graphical result for half a second time signal presented in Figure 4.1a. Red crosses indicate the peaks and green dots the troughs that were identified by the algorithm. To obtain the amplitudes of the data signals, the identified turning points are then processed by a second algorithm (`rainflow.m`), also written by Nieslony (2003). Figure 4.1b represents the identified cycles from the identified turning points in Figure 4.1a.

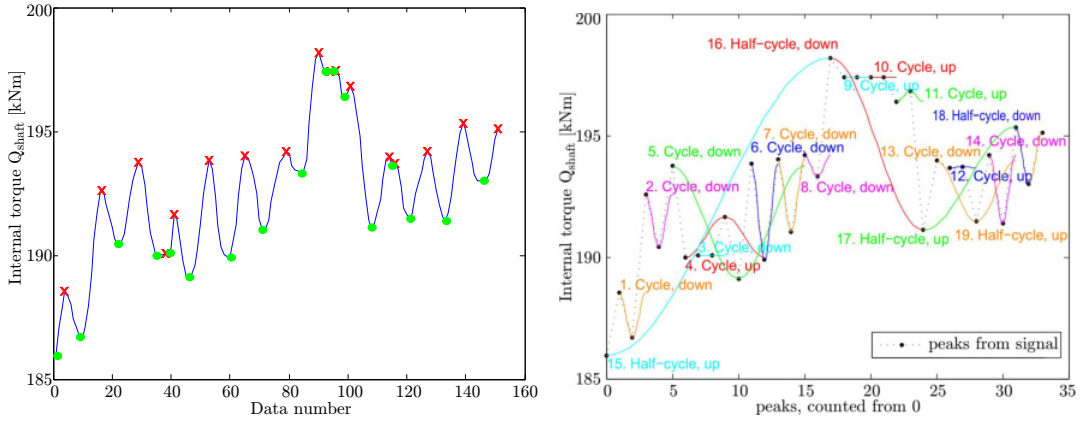

(a) (b)

Figure 4.1: Rainflow counting algorithm used to (a) identify the turning points (crosses - peaks, circles - troughs) and (b) extract cycles from the data signal.

As data recordings were not possible throughout the voyage, it was required to design a representative load history from the recorded data. This was achieved by categorising the data into open water, ice navigation and stationary vessel operations. The conditions could be identified from the vessel's location, speed, shaft line data and logbook information. The logbook keeps a record of vessel operations and location for each day. Stationary times could therefore be determined. The boundary between ice navigation and open water was more difficult to distinguish precisely due to low concentrations and thickness of ice not affecting the shaft line response. This boundary was therefore distinguished through propeller-ice interaction whereby shaft line torque and thrust data resulted in a much more erratic response compared to open water. The vessel reduces its speed during navigation in thick ice. This could therefore be used in conjunction with the shaft line data to identify ice navigation.

Ice, open water and stationary operations were the three most significant conditions experienced by the respective vessels throughout their voyages. The total time spent in each of these conditions (Figure 4.2) was determined and compared against the total time recorded. This allowed for a scaling factor to be determined (Table 4.1) which enabled an estimation of the expected loading profile for a vessel during a voyage to the Arctic and Antarctica.

Table 4.1: Duration of voyage spent in open water, ice and stationary with recorded times for each of these conditions.

	SAA II (2015/2016)			Polarstern		
	Actual [days]	Recorded [days]	Scaling factor	Actual [days]	Recorded [days]	Scaling factor
Ice navigation	10.67	8.54	1.25	11.69	9.15	1.27
Open water	39.96	5.42	7.38	17.31	5.03	3.44
Stationary	17.46	1.58	11.03	19.97	10.95	1.82
Total	68.09	15.54	4.38	48.97	25.13	1.95

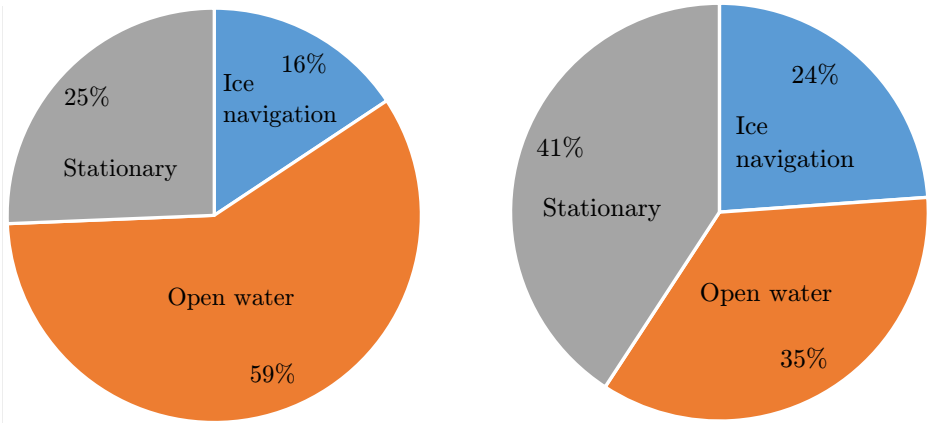

(a) (b)

Figure 4.2: Duration of voyages spent in ice, open water and stationary for (a) SAA II in Antarctica during the 2015/2016 voyage and (b) for the Polarstern in the Arctic during the PS100 voyage in 2016.

Rainflow counting analyses of peak torque values are presented in Figure 4.3 for both vessels. The plots have been displayed for the significant peaks only, as there are many high magnitude peaks occuring at low cycle magnitudes. The highest peak values and total cycles recorded during these conditions are presented in Figure 4.5. The bin size for the histograms was selected to be $1\,\mathrm{kN \cdot m}$ for torque and $1\,\mathrm{kN}$ for thrust. When comparing the results from the conditions for the two vessels, the following was observed:

- Ice navigation results in higher peak values, with the SAA II having a higher distribution overall.
- The most peaks occurred around $100\,\mathrm{kN \cdot m}$ for the SAA II and around $60\,\mathrm{kN \cdot m}$ and $80\,\mathrm{kN \cdot m}$ for the Polarstern.

- Both vessels had significantly higher cycle peaks at higher magnitudes of 310 kN · m for the SAA II and 250 kN · m for the Polarstern, whereby these high magnitude peaks were not as evident in the other two cases.

For the open water case, the greatest torque peak cycles of the SAA II occurred at 150 kN · m, higher than for the ice navigation case. This is due to the pitch of the propeller and shaft line speed being lowered during ice navigation to reduce the speed of the vessel while maintaining enough torque on the shaft line to allow the propeller to chop through ice.

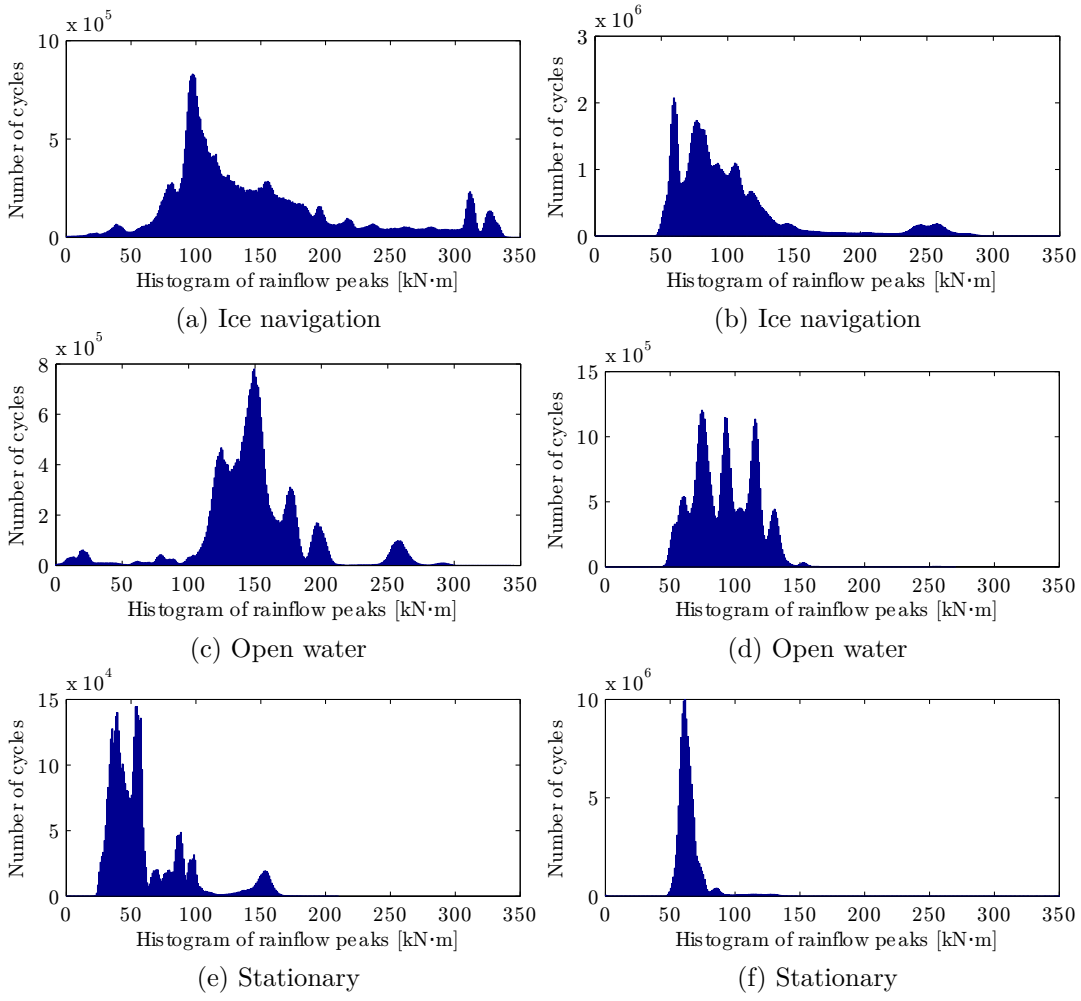

Figure 4.3: Comparison of torque peak rainflow cycles for the SAA II (left) during the 2015/2016 Antarctica voyage and for the Polarstern (right) during the 2016 Arctic voyage.

In open water, the SAA II generally operated above 7 knots at a pitch of 87% and shaft line speed of 135 rpm, compared to a speed below 6 knots, pitch of 74% and shaft line speed of between 90 and 110 rpm during ice navigation. The high cycle loading just above 250 kN · m could be a result of the vessel being operated at just below maximum pitch of 99.5% in open water conditions upon the return leg from Antarctica to Cape Town. The Polarstern had a much narrower spread of high cycle peak torque values, ranging from 50 to 150 kN · m. Within this range there were three distinct high cycle peaks, which were also apparent for the ice navigation condition, however not as prominent due to the broad excitation of torque peaks during ice navigation. The Polarstern generally operated below 7 knots during ice navigation, however the shaft line speed remained relatively constant around 174 rpm throughout the voyage, being directly driven by the diesel generators.

For the stationary case, low torque peak cycles are evident due to the pitch of the propeller being set close to zero during these conditions. The maximum cycles for the Polarstern occur above 50 kN · m. This could be due to the direct diesel engine drive which induces a torque greater than 50 kN · m, whereas the SAA II has a direct electric drive which is smoother. There are a number of high peak torque cycles evident for the stationary case for both vessels. This is due to the vessel using the propeller to keep the vessel stationary during deployment of equipment overboard or keeping a constant thrust on the propeller to keep the vessel stationary against the shelf or bay ice.

Histograms of the rainflow counting analyses of thrust peaks are presented in Figure 4.4 from which the following observations were made:

- The Polarstern experienced a greater range of significant peaks during ice navigation, ranging from 0 to 600 kN.
- The largest number of cycles for the Polarstern shaft occurred at 180 kN for both ice and open water conditions and at 25 kN for the stationary conditions.
- For the SAA II, the largest cycles were distributed between 50 and 150 kN for the ice condition, 170 kN for the open water condition and

140 kN for the stationary condition.

- The reason for the larger significant peaks during open water compared to ice navigation is due to the greater propeller pitch during this condition.

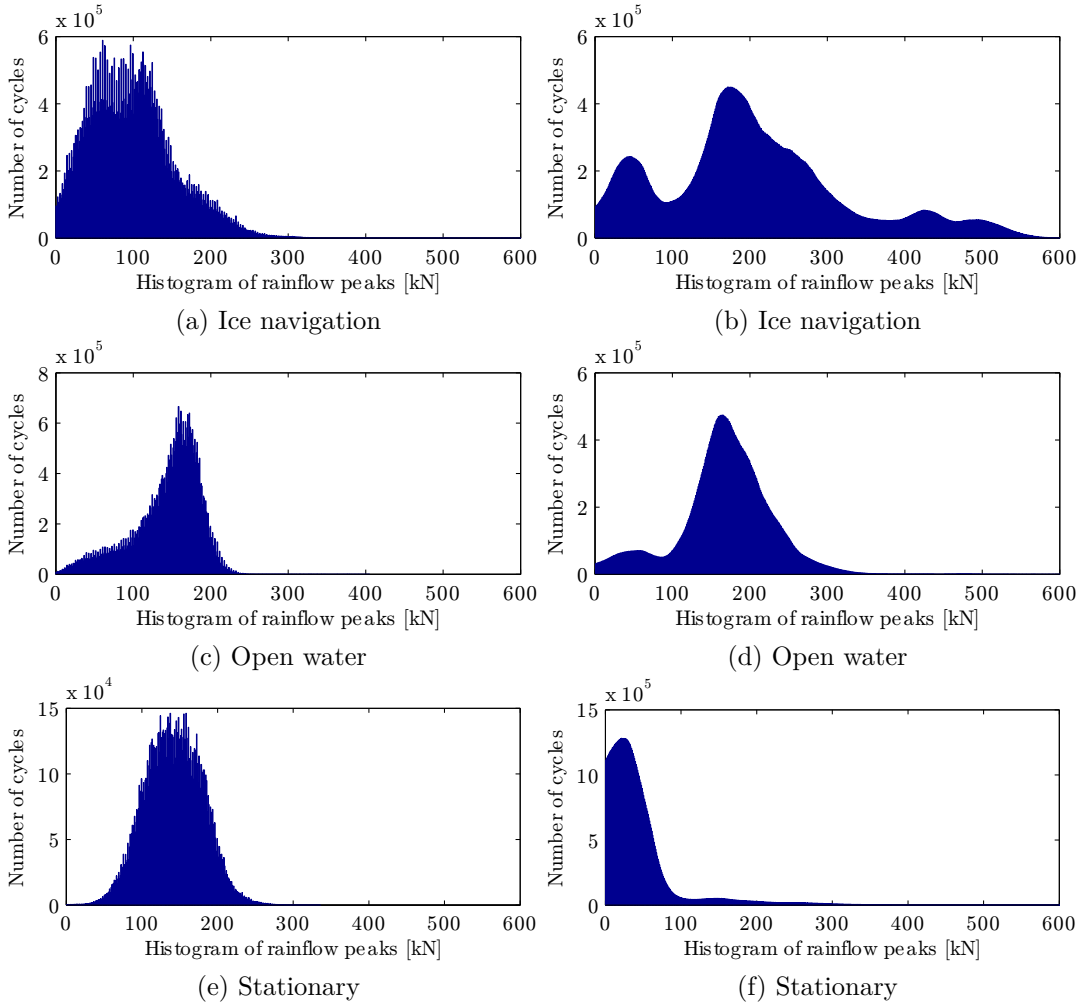

Figure 4.4: Comparison of thrust peak rainflow cycles for the SAA II (left) during the 2015/2016 Antarctica voyage and for the Polarstern (right) during the 2016 Arctic voyage.

The amplitude cycles were not plotted for the individual conditions due to the spread of significant cycles being very narrow. The maximum bin size during each condition is presented in Figure 4.5 from which it is evident that the Polarstern had greater torque peaks, torque amplitudes and thrust amplitudes during the stationary condition compared to the open water condition. This is due to rapid shaft line loading during stations whereby the vessel is required

to remain positioned in the same location, which often requires pushing back against floe ice. The Polarstern experienced higher peak loads compared to the SAA II. This could be due to the Arctic containing harder ice compared to Antarctic or the design of the Polarstern induces higher loads compared to the SAA II due to shaft line geometry. The location of measurements along the shaft is also a factor as torque fluctuates throughout the shaft. For a fair comparison to be made, these shaft line loads need to be converted to propeller loads whereby ice induced loading on the propeller could be compared.

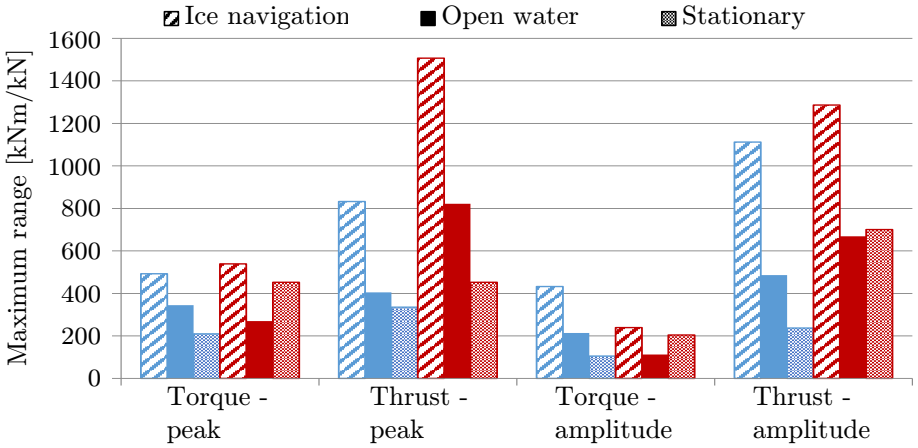

Figure 4.5: Maximum recorded bin size for the SAA II (blue) and Polarstern (red).

The predicted load profiles, which were derived from the three conditions experienced by the SAA II and Polarstern, are presented in Figure 4.6 and 4.7 on logarithmic scales. The torque peak values were divided by the nominal rated torque, Q_{MCR}, to obtain the load response factor, K_a. This is generally used for vessels exposed to varying loads and allows for the safe loading on components along the shaft line, specifically the propeller, to be determined.

Det Norske Veritas (2011*a*) provided an equation to predict the cumulative shaft torque distribution (Equation 2.19) through torque amplitudes as a function of N_{ice}. This equation was presented as an accumulated load spectrum in Figure 2.7. To obtain this curve, Equations 2.15 to 2.18 were used with variables from Table 3.2. This curve was plotted in Figure 4.6c for the SAA II and in Figure 4.7c for the Polarstern, with the curve data recorded in Table 4.2.

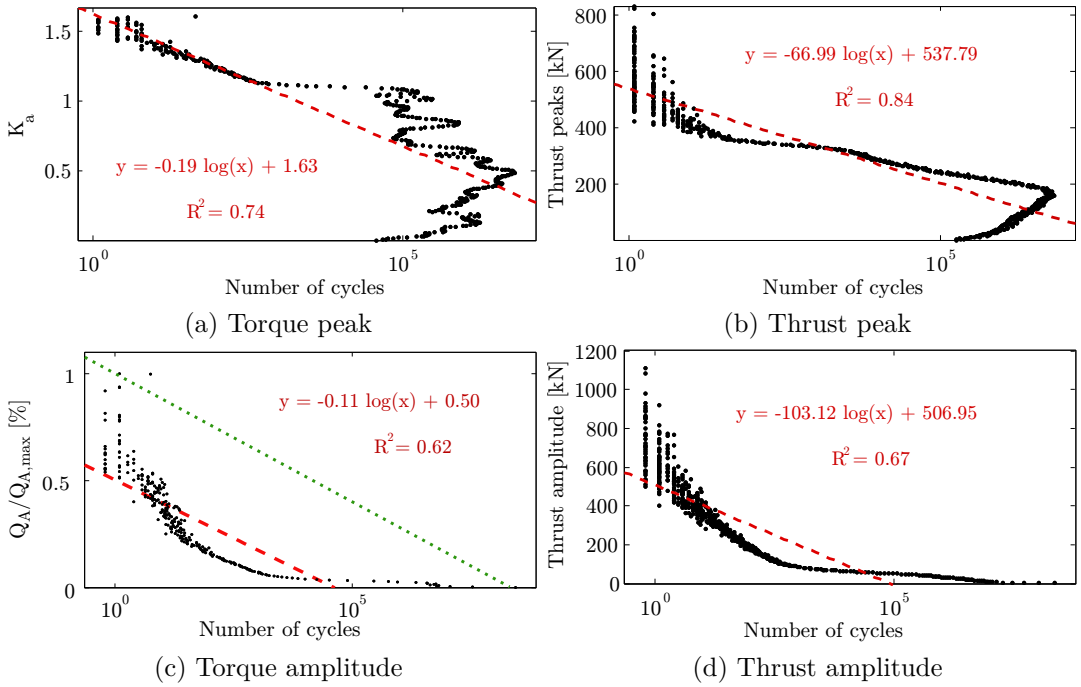

(a) Torque peak (b) Thrust peak

(c) Torque amplitude (d) Thrust amplitude

Figure 4.6: Estimated load profile for a vessel during a voyage to Antarctica based on shaft line measurements from the SAA II during the 2015/2016 voyage.

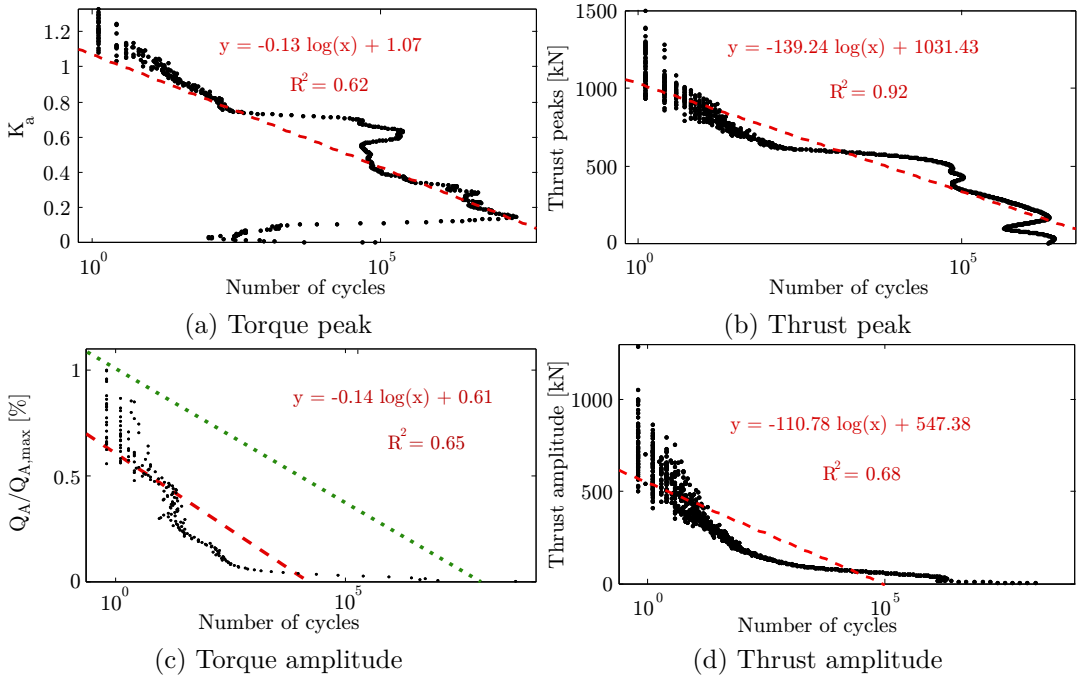

(a) Torque peak (b) Thrust peak

(c) Torque amplitude (d) Thrust amplitude

Figure 4.7: Estimated load profile for a vessel during a voyage to the Arctic based on shaft line measurements from the Polarstern during the 2016 PS100 voyage.

From the data, it is evident that there is a distinct change in the slope. The cause of this change was described by Myklebost and Dahler (2013) to be due to one of two possibilities: either the statistical distribution differs from medium to high impact values, or the distribution below the change in slope is a result of control system or motor excitations and the distribution above the change in slope is as a result of propeller-ice impacts. This corresponds to the typical load cases in Figure 2.8 from Det Norske Veritas (2011*b*) in which ice load amplitudes occur above the distinct change in slope.

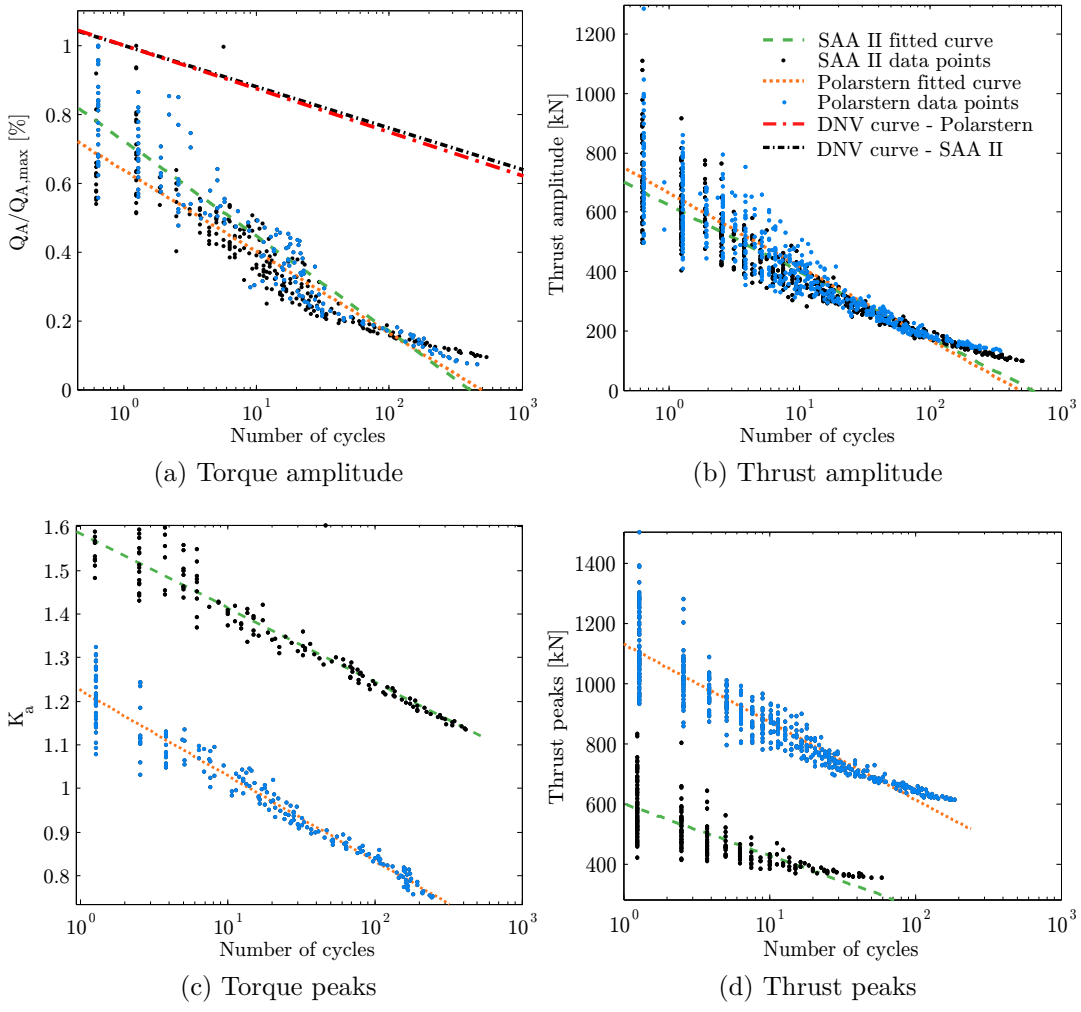

(a) Torque amplitude

(b) Thrust amplitude

(c) Torque peaks

(d) Thrust peaks

Figure 4.8: Comparison between two vessels of predicted load profiling during a voyage to the Arctic and Antarctica.

Table 4.2: Regression, total cycles and curve fit equations for rainflow counting data of the form $y = A\log(x) + B$.

	A	B	R^2	Total cycles
SAA II				
Torque amplitude	-102.47	275.81	0.82	8.73×10^7
Torque peak	-0.17	1.58	0.90	8.72×10^7
Thrust amplitude	-223.87	623.52	0.86	1.27×10^8
Thrust peak	-171.93	600.08	0.60	1.24×10^8
DNV curve	-0.12	1		
Polarstern				
Torque amplitude	-66.41	173.21	0.89	2.72×10^8
Torque peak	-0.20	1.22	0.94	2.72×10^8
Thrust amplitude	-249.58	665.97	0.83	2.63×10^8
Thrust peak	-258.60	1131.57	0.85	2.21×10^8
DNV curve	-0.13	1		

Myklebost and Dahler (2013) determined this change in slope to occur at $1.4 \cdot Q_{MCR}$ during the 2012/2013 voyage for the SAA II. For the 2015/2016 voyage, it was determined to be $1.14 \cdot Q_{MCR}$ for the SAA II and $0.75 \cdot Q_{MCR}$ for the Polarstern during the 2016 PS100 voyage. The change in slopes for peak torque, peak thrust, torque amplitude and thrust amplitude were determined and the data above these points presented in Figure 4.8. This was done to focus the analysis on the ice related loads. The following observations were made from Figure 4.8:

- The SAA II experienced greater torque peaks relative to its Q_{MCR}, however similar magnitudes were experienced by the two vessels overall. The plot is deceiving as it appears the SAA II experienced greater torque peaks. This is due to the 100 kN · m difference between the Q_{MCR} of the two vessels.

- Significantly smaller thrust peaks were experienced by the SAA II throughout its voyage compared to the Polarstern. One possible reason could be due to the smaller diameter shaft of the Polarstern, thus experiencing a greater thrust value at the location of the strain gauge measurement.

- The torque amplitude curve from DNV focuses on the cumulative ice loading distribution. It is therefore expected to have a better comparison

to the ice load data in Figure 4.8a compared to the total load presented in Figure 4.6c and 4.7c, which is not the case. Possible reasons for this phenomenon could be attributed to the fact that not many transition cases between open water and ice were recorded for both vessels. This would result in low cycles of high magnitude and high cycles of low magnitude being dominant, which is evident in the current data.

The representative curves for the data are recorded in Table 4.2, with regression values and total cycles for each of the four cases for each vessel.

4.2 Open water, cavitation and ice navigation

Three case studies were selected based on the shaft line response measured during the voyage. These were cavitation, ice navigation and open water as presented in Table 4.3. Five characteristics of the shaft line response were analysed for each of these case studies. These included torque, thrust and the x, y and z direction vibration on the radial bearings. These results are displayed in Figure 4.10.

Table 4.3: Average values of variables during case studies.

Variable	Open water	Cavitation	Ice navigation
SAA II			
Date	2016/02/02	2015/12/15	2015/12/24
Time	13:00	10:52	09:21
SOG	7.12 knots	1.05 knots	2.11 knots
Shaft speed	108.14 rpm	141.44 rpm	121.76 rpm
Pitch	99.56%	24.19%	72.74%
Motor power	1693.03 kW	2068.05 kW	3557.87 kW
Polarstern			
Date	2016/09/02	2016/08/20	2016/07/30
Time	08:30	18:05	11:18
SOG	14.01 knots	6.19 knots	4.70 knots
Shaft speed	174.00 rpm	174.25 rpm	173.50 rpm

Video recordings during cavitation were performed for short durations with a GoPro Hero 3+. These recordings were not possible during open water and

ice navigation for the SAA II due to the water resistance being too great at high speeds and ice blocks posing a risk to the camera. For the Polarstern, the GoPro was placed in a bolted and valve sealed window that looks out onto the propeller. The clarity of the recordings were dependent on the amount of sunlight able to penetrate the surface of the ocean and recordings during heavy ice posed too great a risk. The time signals and frequency content of the case studies were analysed and compared to identify certain characteristics and to determine the effect on fatigue life.

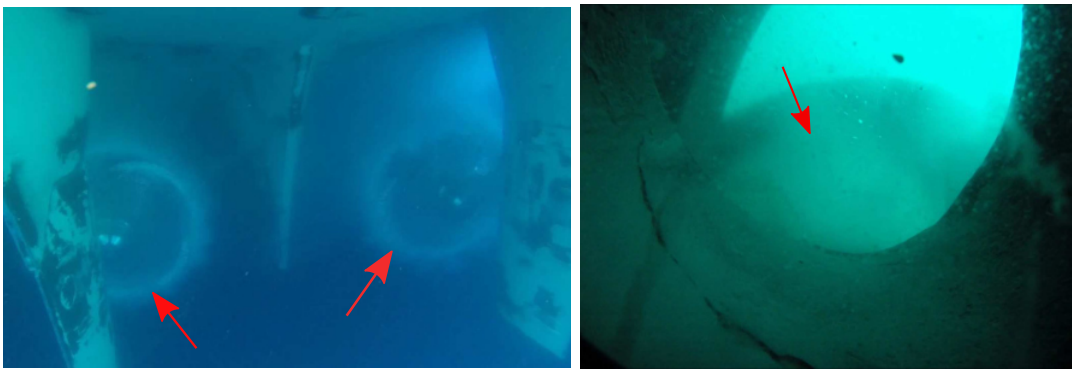

(a) SA Agulhas II (b) Polarstern

Figure 4.9: Snapshots of cavitation occurring during open water operation on (a) the SAA II on 14 January 2016 (SOG: 1.7 knots, shaft speed: 141.7 rpm, pitch: -72.2%, motor power: 2620 kW) and (b) the Polarstern on 24 August 2016 (SOG: 6.16 knots, shaft speed: 174.5 rpm).

Snapshots from video recordings during cavitation, on 14 January 2016 for the SAA II and on 24 August 2016 for the Polarstern, are presented in Figure 3.3. During the cavitation scenario there was noticeable vibration throughout the vessels, accompanied by a loud rumbling noise. This resembles that of tip vortex cavitation according to Kuiper (1997) due to broadband excitation of the vessel hull structure. Bubble and sheet cavitation also appears to have been present according to Sharma *et al.* (1990), whereby they reported these types of cavitation to result in noise problems. From Figure 4.9a, tip vortex cavitation is visible (arrows) but bubble and sheet cavitation is not clearly visible. The snapshot in Figure 4.9b of cavitation for the Polarstern, indicated with an arrow, is not very clear due to reduced sunlight on the day. The time

frame during these video recordings were not used for analysis due to better, more prominent conditions having been selected.

The shaft line response for both vessels during open water, cavitation and ice navigation for a fifteen second interval are presented in Figure 4.10. The open water condition was used as a reference against which to compare the other two case studies. When analysing the torque and thrust data, one needs to ensure that the induced changes are not caused by machine control parameters. Propeller pitch is the most common of these and has a direct effect on torque and thrust. When a positive propeller pitch is engaged, the torque and thrust response is positive. But when a negative pitch is engaged, the torque response is positive but the thrust response negative. This is due to the rotation of the shaft line always being in the same direction. Therefore the torque is positive for both positive and negative pitch and will reduce as pitch changes to zero; however the torque will only reach zero when the shaft line stops rotating. When analysing the accelerometer data, it is important to note that the accelerometers were mounted on the shaft line radial bearings and therefore the x direction vibration is not solely attributed to the shaft vibration, but rather a combination of the shaft line and the vessel hull.

The characteristics of the shaft line response during cavitation were found to result in an increase in torque and thrust amplitude as well as an increase in shaft vibration, specifically the x direction. The torque response of the vessels contains sudden changes in magnitude and significant amplitude fluctuations. Propeller pitch has a direct effect on the torque and thrust. However, in this case there are sudden drops in torque for the SAA II when a general increase is expected due to a gradual increase in pitch. Contrary to expectations it is therefore observed that torque decreases during instances of cavitation. This complies with research done by Walker (1996) whereby torque and thrust coefficients were found to reduce during cavitation, indicating a reduction in the mean level of hydrodynamic load on the propeller during cavitation. A decrease in thrust was also observed for the SAA II, with a significant increase in the amplitudes. The fluctuations were severe enough to result in a reverse thrust of $-1120.4\,\text{kN}$ and a maximum amplitude of $930.8\,\text{kN}$. The affect of

cavitation on the Polarstern was not as severe. There was an increase in both torque and thrust, however the amplitudes and oscillations were not as great as that of the SAA II. From the analysis, it is evident that thrust is more severely affected during this condition compared to torque, whereby a clear change in the thrust profile, with large oscillations about the hydrodynamic thrust value, is visible.

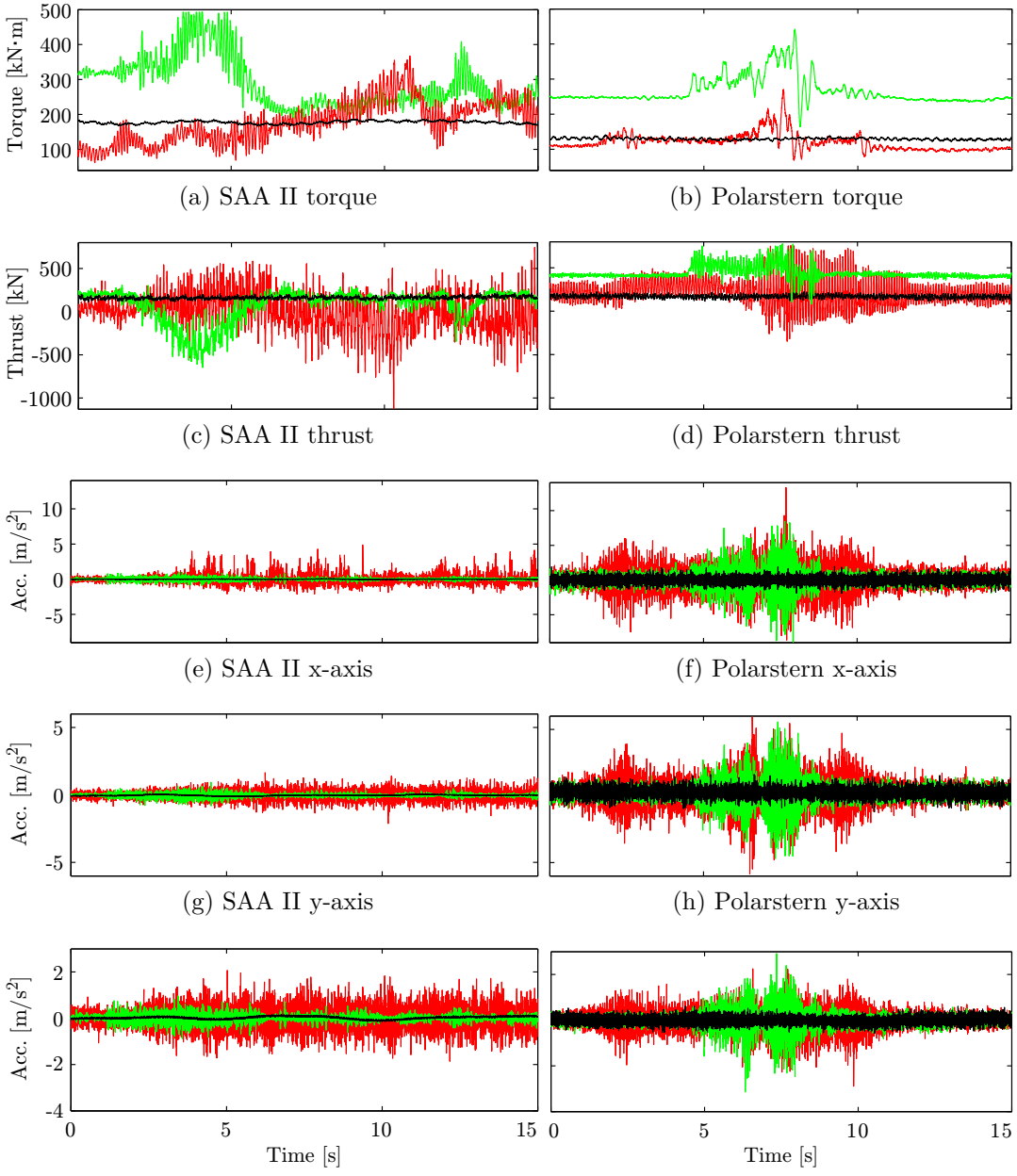

(a) SAA II torque (b) Polarstern torque

(c) SAA II thrust (d) Polarstern thrust

(e) SAA II x-axis (f) Polarstern x-axis

(g) SAA II y-axis (h) Polarstern y-axis

(i) SAA II z-axis (j) Polarstern z-axis

Figure 4.10: Comparison of open water (black), cavitation (red) and ice navigation (green) for the SAA II (left) and Polarstern (right).

For the ice navigation condition, one notices a greater change in the torque profile compared to the thrust for both vessels, whereby the highest torque values were achieved at 493.0 kN · m for the SAA II and 458.7 kN · m for the Polarstern. For ice navigation, the propeller pitch remained relatively constant and therefore the change in torque and thrust is the result of the propeller-ice interaction. The torque increased suddenly from around 325 kN · m to 470 kN · m for the SAA II during the first propeller-ice interaction phase. The thrust decreased from around 200 kN to −500 kN during the associated time frame. The reason for the increase in torque, according to Huisman *et al.* (2014) is due to the extreme loading as well as cyclic moderate loading during propeller-ice interaction. The reason for the large decrease in thrust could be due to the ice floes impacting the propeller from the bow-side, resulting in the elongation of the shaft. The first propeller-ice interaction for the Polarstern resulted in a change of torque from around 250 kN · m to 440 kN · m. There was a significant change in the thrust values, but instead of the thrust amplitudes increasing with oscillations about the hydrodynamic load as with the cavitation condition, the thrust decreased during ice impacts for the SAA II and increased for the Polarstern. The increase in thrust for the Polarstern during ice interaction is due to the ice floes adding an additional load to the hydrodynamic load, resulting in an overall greater thrust on the shaft line.

Table 4.4: Summary of torque and thrust measurements (OW - Open water, Cav - Cavitation, IN - Ice navigation).

	Torque [kN·m]			Thrust [kN]		
	OW	Cav	IN	OW	Cav	IN
SAA II						
Max abs. peak	186.9	367.7	493.0	219.8	-1120.4	644.9
Max amp.	10.6	152.9	155.0	52.2	930.8	497.6
Mean	177.5	177.7	288.6	161.0	-5.3	74.4
Polarstern						
Max peak	141.5	271.0	442.3	223.6	756.6	770.7
Max amp.	10.2	101.4	139.2	56.8	551.5	344.7
Mean	129.8	120.1	265.8	168.6	219.5	436.9

For the open water condition, the torque and thrust oscillated with time.

For thrust this variation was contained to around 55 kN, whereas variation in the torque signal was around 10 kN · m for the two vessels. The torque and thrust response fluctuated at a frequency of 1.76 Hz for the SAA II and 2.93 Hz, which is the same frequency as the shaft line rotational speed for each vessel (1.8 × 60rpm and 2.9 × 60rpm). This wave is therefore caused by the rotational driving torque of the electric motor for the SAA II and the diesel motor for the Polarstern. The greatest vibrations from the radial bearings were measured during cavitation, especially in the x direction. Vibrations from ice impacts were experienced more evenly by the three axes, with the x direction experiencing the greatest acceleration, followed by the y direction. The z direction experienced the least acceleration during cavitation and ice navigation. The Polarstern experiences higher levels of vibration during normal operation compared to the SAA II, as is evident from the open water vibration results, as well as during cavitation and ice navigation. The reason for this could be due to the direct diesel drive through a gearbox for the Polarstern, inducing greater vibrations to the shaft line compared to an electric motor drive with the SAA II. The characteristics of each case study are summarised in Table 4.4.

Fast Fourier Transforms (FFT) were calculated for the torque and thrust signals. The results for torque in Figure 4.11 allow for the following conclusions.

- In each case study the rpm of the shaft could be identified for both vessels. For the SAA II this was 1.7, 2.3 and 2.0 Hz for open water, cavitation and ice navigation respectively. For the Polarstern this value remained reasonably constant for all three cases at 2.9 Hz.

- The first blade-pass frequency of the four-bladed propeller was identified for the SAA II at 7.0 Hz for open water and 9.2 Hz for cavitation. The first blade-pass frequency was not evident for the ice navigation condition due to broadband excitation during propeller-ice impacts masking this frequency. For the Polarstern this frequency was 11.7 Hz for all three cases due to a constant rpm.

- The first natural frequency of the shaft line torsional vibration during ice navigation was determined to be 11.1 Hz (marker 2) for the SAA II,

which is similar to the value of 11.2 Hz determined by Peltokorpi *et al.* (2014) during full-scale measurements in the Baltic Sea. This peak increased to 11.3 Hz during cavitation and decreased to 10.9 Hz during open water. For the Polarstern this frequency changed from 11.1 Hz for open water to 11.3 Hz for cavitation and ice navigation (marker 5). The reason for this is attributed to the change in boundary conditions between the shaft line and the working environment.

- The second blade-pass frequency for the SAA II was identified as 14.2, 13.8 and 13.9 Hz for open water, cavitation and ice navigation. For the Polarstern this frequency was identified at 19.6, 20.1 and 20.2 Hz (marker 6).

- The second natural frequency of the shaft line torsional vibration for the SAA II was evident for all three case studies around 46.6 Hz (marker 3), however it was not dominant during ice navigation due to broad-band excitation from ice impacts. This frequency peak was stable for the Polarstern during all three cases at 41.2 Hz (marker 8).

- The third blade-pass frequency was not clearly evident for the SAA II, but was for the Polarstern at 46.4 Hz (marker 9).

- The blade natural frequencies for the Polarstern could be identified at 20.7 and 20.5 Hz (between marker 6 and 7) for open water and cavitation. These values are very similar to the experimentally determined value of 21.0 Hz, where the difference can be attributed to water damping on the blades during operational conditions.

- For ice navigation, there was a dominating frequency content around 5.3 Hz (marker 1) for the SAA II which was not evident in the other two case studies. This could be due to propeller-ice impacts not always occurring on all four blades for the same ice piece, but only three of the blades resulting in a frequency content three times the shaft rpm being excited. A similar incident occurred for the Polarstern at 4.0 Hz (marker 4) and 25.8 Hz (marker 7) for the cavitation condition. This can however not be confirmed and requires further investigation.

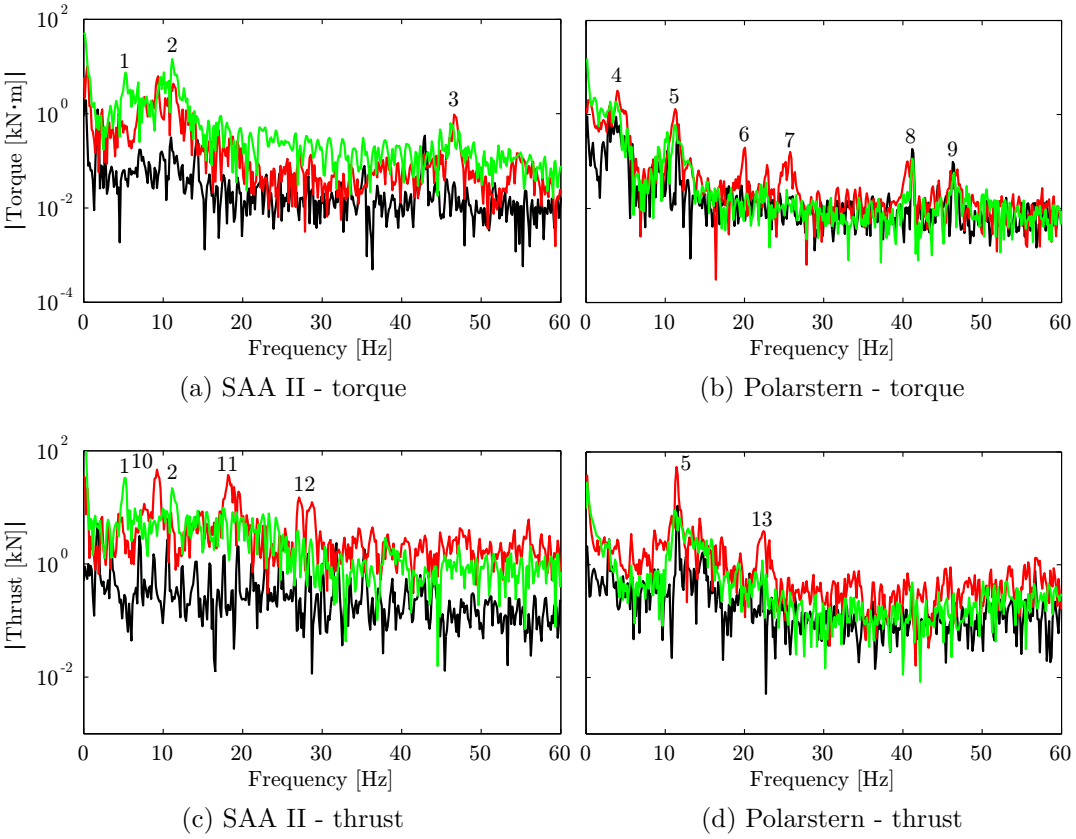

(a) SAA II - torque (b) Polarstern - torque

(c) SAA II - thrust (d) Polarstern - thrust

Figure 4.11: FFT of shaft line torque (a,b) and thrust (c,d) for the SAA II (left) and Polarstern (right) during open water (black), cavitation (red) and ice navigation (green) (Duration: 15 seconds, sample rate: 600 Hz, block size: 4096, window: Hanning, overlap: 50%).

For the thrust FFT spectrum (Figure 4.11), the same frequency contents were dominant as for the torque. Additional frequencies were evident at 18.6 Hz (marker 11) for the second axial excitation mode and 28.7 Hz (marker 12) for the third axial excitation mode of the SAA II during cavitation. These frequencies could be identified from axial vibration calculations performed by Rolls-Royce AB (2010*a*) during the design of the shaft, which were identified as 17.5 and 30.2 Hz for the second and third axial excitation modes. The first blade-pass frequency of the four-bladed propeller was evident for the SAA II at 9.2 Hz (marker 10) for the cavitation condition. There was a strong frequency content at 22.3 Hz (marker 13) for the Polarstern for all three cases. This frequency is very close to the natural frequency of the propeller blades and could therefore be an axial vibration of the blades but cannot be confirmed.

Chapter 5

Indirect force estimation

The current research involves measurements on the shaft line of the PSRVs from which the initial loading on the propeller could be determined. In order to achieve this, a forward problem was first formulated to determine the transfer function between the external moment on the propeller and the internal torque in the shaft line at the point of measurement. This was followed by an inverse problem to determine external propeller loads from the measured shaft line torque. This method was only implemented on the SAA II as limited information was available for the Polarstern.

5.1 Dynamic model

The forward problem for the SAA II was solved using a lumped mass model as per Rolls-Royce AB (2010*b*) documentation and Ikonen *et al.* (2014). The Newmark-Beta method was used for direct integration in the time domain. All calculations were performed using algorithms programmed in MatLab. A diagram of the model is presented in Figure 5.1.

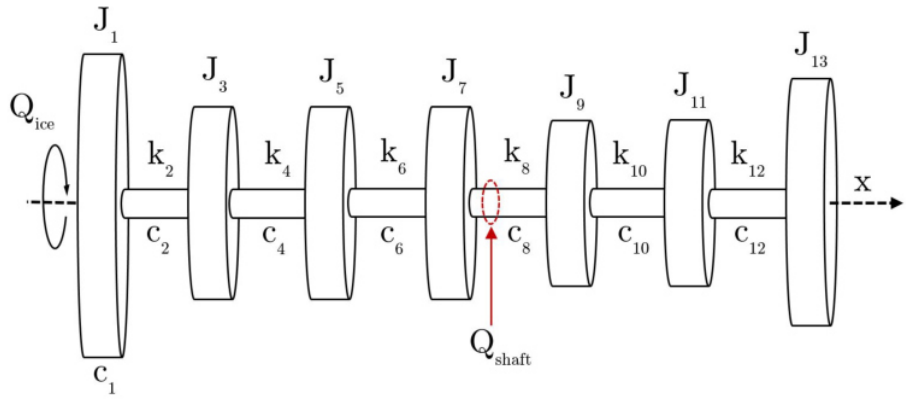

Figure 5.1: Dynamic model of the SAA II shaft line consisting of inertia, damping and torsional spring elements. J_1 is the CPP, J_3 the mid-propeller shaft, J_5 the sleeve coupling, J_7 the oil distribution box flange, J_9 the thrust shaft collar, J_{11} the electric motor flange and J_{13} the propulsion motor. c_1 is the water damping on the rotating propeller, $c_2, c_4, ..., c_{12}$ and $k_2, k_4, ..., k_{12}$ respectively represent the shaft line damping and torsional stiffness.

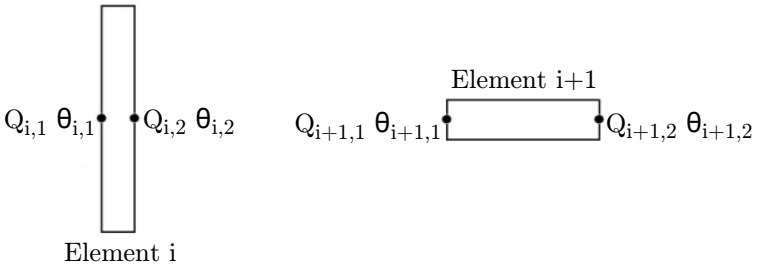

Figure 5.2: Elements and relative nodes. Adapted from Ikonen *et al.* (2014).

5.1.1 Forward problem

Only rotational degrees of freedom about the shaft axis (x-axis) are considered. Other degrees of freedom are ignored in this approach. Each element contains two nodes, one on either side of the element as shown in Figure 5.2, at which torsional moment Q and angular displacement θ is determined. Using the governing equation of torsional vibration, which was presented in Equation 2.20, Equation 5.1 can be derived for inertia elements for odd values of i and Equation 5.2 for torsional spring elements for even values of i:

$$J_i\ddot{\theta}_{i,1} + c_i\dot{\theta}_{i,1} = -Q_{i,1} + Q_{i,2} + Q_{ice} \tag{5.1}$$

$$c_i\left(\dot{\theta}_{i,2} - \dot{\theta}_{i,1}\right) + k_i\left(\theta_{i,2} - \theta_{i,1}\right) = Q_{i,1} \tag{5.2}$$

with i being the increment for the thirteen elements of the shaft line system. Subscript $(i, 1)$ denotes the value of the variable on the left side of the element and subscript $(i, 2)$ on the right side of the element. For inertia elements, the angular displacement on the right and left side are equal, and therefore $\theta_{i,1} = \theta_{i,2}$. For spring elements, the internal torque remains constant and therefore $Q_{i,1} = Q_{i,2}$.

Direct numerical integration of dynamic equations is one of the most general approaches to obtaining the solution to the dynamic response of a structural system (Wilson, 2002). There are many different direct integration methods that could be used to obtain the approximate solution of a dynamic system, where the two principal approaches to multi-degree of freedom direct integration methods are the explicit and implicit schemes (Dukkipati, 2010). For an explicit scheme, previously determined values of displacement, velocity and acceleration are used to determine the response quantities (Dukkipati, 2010). For an implicit scheme, the equations of motion and difference equations are combined to calculate the displacement directly (Dukkipati, 2010).

The most widely used explicit schemes are the central difference, fourth-order Runge-Kutta and two-cycle iteration with trapezoidal rule method (Dukkipati, 2010). For implicit schemes, it is the Wilson-Theta, Houbolt, Newmark-Beta and Park Stiffly stable method (Dukkipati, 2010). Implicit schemes involve iterative procedures for each time step, making them more computationally intensive (Wilson, 2002). However, the disadvantage of explicit schemes is that they are only conditionally stable relative to the size of the selected time step whereas implicit schemes can be either conditionally or unconditionally stable Wilson (2002). Wilson (2002) states that from a significant amount of experience, only single-step, implicit, unconditional stable methods should be used for step-by-step analysis of practical structures. The author therefore suggests the Newmark-Beta method, but states that this method is only unconditionally stable if

$$2\beta \geq \gamma \geq \frac{1}{2} \tag{5.3}$$

where $\gamma = 0.5$ and $\beta = 0.25$ are parameters which quantify the contribution of the angular displacement, velocity and acceleration to the dynamic response in

the next time step. Using the Average Acceleration method for Newmark-Beta, with $\gamma = 0.5$ and $\beta = 0.25$, will result in no energy dissipation and provide good accuracy for small time steps (Wilson, 2002). The angular velocity $\dot{\theta}$ and angular acceleration $\ddot{\theta}$ can be determined for the next time step through the Newmark-Beta method (Wilson, 2002):

$$\ddot{\theta}_{t+\Delta t} = \frac{1}{\beta \Delta t^2}\left(\theta_{t+\Delta t} - \theta_t\right) - \frac{1}{\beta \Delta t}\dot{\theta}_t - \left(\frac{1}{2\beta} - 1\right)\ddot{\theta}_t \tag{5.4}$$

$$\dot{\theta}_{t+\Delta t} = \frac{\gamma}{\beta \Delta t}\left(\theta_{t+\Delta t} - \theta_t\right) + \left(1 - \frac{\gamma}{\beta}\right)\dot{\theta}_t - \left(\frac{\gamma}{2\beta} - 1\right)\Delta t \ddot{\theta}_t \tag{5.5}$$

These equations can be written in incremental form by determining the change in values from the previous time step to the current time step (He and Du, 2010):

$$\Delta\ddot{\theta}_t = \ddot{\theta}_{t+\Delta t} - \ddot{\theta}_t = \frac{1}{\beta \Delta t^2}\Delta\theta_t - \frac{1}{\beta \Delta t}\dot{\theta}_t - \frac{1}{2\beta}\ddot{\theta}_t \tag{5.6}$$

$$\Delta\dot{\theta}_t = \dot{\theta}_{t+\Delta t} - \dot{\theta}_t = \frac{\gamma}{\beta \Delta t}\Delta\theta_t - \frac{\gamma}{\beta}\dot{\theta}_t - \left(\frac{\gamma}{2\beta} - 1\right)\ddot{\theta}_t \Delta t \tag{5.7}$$

The dynamic problem is solved by combining the Newmark-Beta integration method and an incremental form of the governing equation of torsional vibration. The dynamic response for internal torque $Q_{shaft}(t)$ on the shaft line can subsequently be determined from external ice loading $Q_{ice}(t)$ on the propeller.

Rewriting Equations 5.1 and 5.2 into incremental form and substituting the Newmark-Beta equations (Equation 5.6 and 5.7) for the angular velocity and angular acceleration variables, the following equations can be obtained:

$$\Delta Q_{i,1}(t) + A_i \Delta\theta_{i,1}(t) - \Delta Q_{i,2}(t) = B_i \tag{5.8}$$

$$\Delta Q_{i,1}(t) + A_i \Delta\theta_{i,1}(t) - A_i \Delta\theta_{i,2}(t) = B_i \tag{5.9}$$

where variables A_i and B_i for odd i values (inertia elements) are:

$$A_i = \frac{J_i}{\beta \Delta t^2} + \frac{c_i \gamma}{\beta \Delta t} \tag{5.10}$$

$$B_i = J_i \left[\frac{1}{\beta \Delta t} \dot{\theta}_i(t) + \frac{1}{2\beta} \ddot{\theta}_i(t) \right] + c_i \left[\frac{\gamma}{\beta} \dot{\theta}_i(t) + \left(\frac{\gamma}{2\beta} - 1 \right) \ddot{\theta}_i(t) \Delta t \right] + \Delta Q_{ice}(t) \quad (5.11)$$

and for even i values (spring elements):

$$A_i = k_i + \frac{c_i \gamma}{\beta \Delta t} \quad (5.12)$$

$$B_i = c_i \left[\frac{\gamma}{\beta} \left(\dot{\theta}_i(t - \Delta t) - \dot{\theta}_i(t) \right) + \left(\frac{\gamma}{2\beta} - 1 \right) \Delta t \left(\ddot{\theta}_i(t - \Delta t) - \ddot{\theta}_i(t) \right) \right] \quad (5.13)$$

These equations can then be written in matrix form to enable the handling of multiple element systems, with Equation 5.14 for odd i values (inertia elements) and Equation 5.15 for even i values (spring elements):

$$\begin{bmatrix} 1 & A_i & -1 & 0 \\ 0 & 1 & 0 & -1 \end{bmatrix} \begin{bmatrix} \Delta Q_{i,1} \\ \Delta \theta_{i,1} \\ \Delta Q_{i,2} \\ \Delta \theta_{i,2} \end{bmatrix} = \begin{bmatrix} B_i \\ 0 \end{bmatrix} \quad (5.14)$$

$$\begin{bmatrix} 1 & A_i & 0 & -A_i \\ 1 & 0 & -1 & 0 \end{bmatrix} \begin{bmatrix} \Delta Q_{i,1} \\ \Delta \theta_{i,1} \\ \Delta Q_{i,2} \\ \Delta \theta_{i,2} \end{bmatrix} = \begin{bmatrix} B_i \\ 0 \end{bmatrix} \quad (5.15)$$

where the second row in Equation 5.14 states that $\theta_{i,1} = \theta_{i,2}$ and the second row in Equation 5.15 states that $Q_{i,1} = Q_{i,2}$. The shaft line system can be described by a single equation when combining Equation 5.14 and 5.15 to obtain

$$W \begin{bmatrix} \Delta Q_1 & \Delta \theta_1 & \Delta Q_2 & \Delta \theta_2 & \cdots & \Delta Q_{N+1} & \Delta \theta_{N+1} \end{bmatrix}^T = B \quad (5.16)$$

where $N = 13$ represents the total number of elements with the additional state vector representing the right end of the last element N. Matrix W can be defined in the same way as was done by Ikonen *et al.* (2014):

$$W = \left[\begin{array}{cccccccccc} 1 & 0 & 0 & 0 & 0 & 0 & \cdots & 0 & 0 \\ \hline e_{1,1,1} & e_{1,1,2} & e_{1,1,3} & e_{1,1,4} & 0 & 0 & \cdots & 0 & 0 \\ e_{1,2,1} & e_{1,2,2} & e_{1,2,3} & e_{1,2,4} & 0 & 0 & \cdots & 0 & 0 \\ 0 & 0 & e_{2,1,1} & e_{2,1,2} & e_{2,1,3} & e_{2,1,4} & \cdots & 0 & 0 \\ 0 & 0 & e_{2,2,1} & e_{2,2,2} & e_{2,2,3} & e_{2,2,4} & \cdots & 0 & 0 \\ \vdots & \vdots & \vdots & \vdots & \ddots & \ddots & \ddots & \vdots & \vdots \\ 0 & 0 & 0 & 0 & \cdots & e_{N,1,1} & e_{N,1,2} & e_{N,1,3} & e_{N,1,4} \\ 0 & 0 & 0 & 0 & \cdots & e_{N,2,1} & e_{N,2,2} & e_{N,2,3} & e_{N,2,4} \\ \hline 0 & 0 & 0 & 0 & \cdots & 0 & 0 & 1 & 0 \end{array}\right] \tag{5.17}$$

where $e_{i,j,k}$ represents the elements of the two-by-four matrices in Equation 5.14 and 5.15 with i being the index of the elements, j the row number and k the column number of the corresponding two-by-four matrix. The first and last row of matrix W define the boundary conditions of the system, with the two constant setting the boundary conditions at both ends of the shaft (nodes 1 and 14). This results in the internal torques Q_i being set equal to zero while allowing free displacement about the axis of rotation. The B vector in Equation 5.16 is defined as

$$B = \begin{bmatrix} 0 & B_1 & 0 & B_2 & 0 & \cdots B_{N-1} & 0 & B_N & 0 & 0 \end{bmatrix}^T \tag{5.18}$$

where B_i are the values obtained from Equation 5.11 for odd values of i and from Equation 5.13 for even values of i.

During the iterative process, angular displacement, θ_i, angular velocity, $\dot{\theta}_i$, angular acceleration, $\ddot{\theta}_i$, and internal torque, Q_i, are assumed to have an initial value of zero at all nodes. This will require the hydrodynamic load to be subtracted from the measured internal torque on the shaft line to allow for a zero initial value for ΔQ_i. The variables for each time step can be determined by solving Equation 5.16 for the change in angular displacement $\Delta\theta_i$ and internal torque ΔQ_i:

$$\begin{bmatrix} \Delta Q_1 & \Delta\theta_1 & \Delta Q_2 & \Delta\theta_2 & \cdots & \Delta Q_{N+1} & \Delta\theta_{N+1} \end{bmatrix} = W^{-1}B \tag{5.19}$$

The variables θ_i and Q_i are updated through substitution of the determined increments from Equation 5.19. Variables $\dot{\theta}_i$ and $\ddot{\theta}_i$ are updated using

the Newmark-Beta equations (Equation 5.6 and 5.7) and the increments from Equation 5.19. Lastly, parameters A_i and B_i will be updated through the new angular velocity $\dot{\theta}_i$ and angular acceleration $\ddot{\theta}_i$ values. The external torque Q_{ice} is a step input applied on the propeller, therefore $Q_{ice} = 0$ for $t < 0$ and $Q_{ice} = 1$ for $t \geq 0$. However, the external torque applied in Equation 5.11 is the change in torque, therefore $\Delta Q_{ice} = 1$ for the first increment and thereafter set to zero. This procedure will be repeated until the desired time step is reached. The variables used for the dynamic model were obtained from Rolls-Royce AB (2010*b*) and are presented in Appendix B.3.

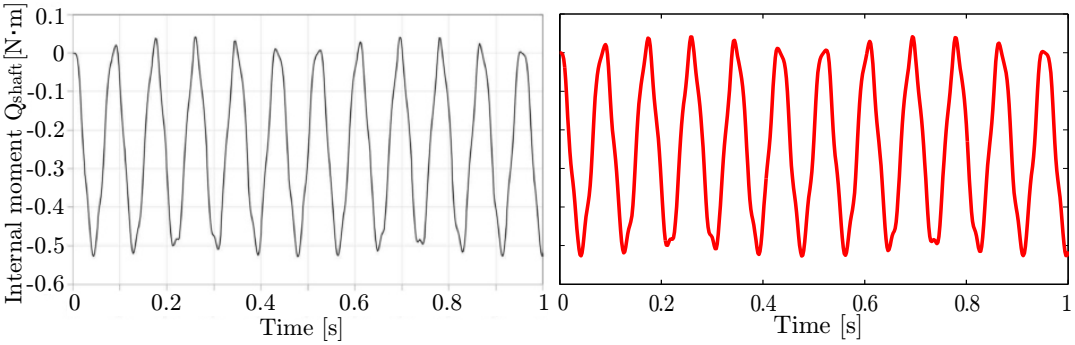

Figure 5.3: Resultant internal torque on shaft line element 8 from a unit step input applied to the propeller through the dynamic model of the SAA II. This response was determined without damping. Results obtained by (a) Ikonen *et al.* (2014) and (b) current model.

The internal torque response in shaft line element eight for a unit step input and no damping is presented in Figure 5.3. This result was compared to the result obtained by Ikonen *et al.* (2014). The two graphs are identical indicating that the current method is accurate. The two lowest natural frequencies of the SAA II shaft line have been determined by Peltokorpi *et al.* (2014) to be 11.2 and 46.3 Hz. By comparison, the determined natural frequencies from Ikonen *et al.* (2014) and the current model are presented in Table 5.1.

The reason for the difference in natural frequencies between the two models is due to slightly different variables having been implemented by Ikonen *et al.* (2014) compared to the Rolls-Royce AB (2010*b*) variables used in the current model.

Table 5.1: Comparison of natural frequencies determined numerically through current model and by Ikonen *et al.* (2014) to natural frequencies determined through full-scale measurements by Peltokorpi *et al.* (2014).

	Peltokorpi *et al.* (2014)	Ikonen *et al.* (2014)	Current model
f_1	11.2 Hz	11.5 Hz	11.5 Hz
f_2	46.3 Hz	48.2 Hz	47.4 Hz
% error f_1		2.7%	2.4%
% error f_2		4.1%	2.3%

Modelling a system to have linearly elastic material behaviour allows for the principle of superposition to be applied (Inman, 2014). This enables the use of Equation 5.20 to determine the integral of the product of two functions, of which one is shifted by the variable of integration Φ (Inman, 2014):

$$Q_{shaft}(t) = \int_0^t H(t-\Phi)Q_{ice}(\Phi)d\Phi \tag{5.20}$$

This integral is referred to as the convolution integral and represents the dependency between the loading on the propeller, Q_{ice}, and the response measured on the shaft line, Q_{shaft}, with H the impulse response matrix between the loading point at the propeller and the measurement location on the shaft. Equation 5.20 can be solved by transforming it into a system of linear equations through discretizing the integral into time steps, resulting in the following equation (Jacquelin *et al.*, 2003):

$$Q_{shaft}(t) = H(t)Q_{ice}(t) \tag{5.21}$$

with

$$Q_{shaft} = \begin{bmatrix} q_{shaft}(\Delta t) \\ q_{shaft}(2\Delta t) \\ q_{shaft}(3\Delta t) \\ \vdots \\ q_{shaft}(n\Delta t) \end{bmatrix}; \qquad H = \begin{bmatrix} h(\Delta t) & 0 & \dots & 0 \\ h(2\Delta t) & h(\Delta t) & \dots & 0 \\ h(3\Delta t) & h(2\Delta t) & \dots & 0 \\ \vdots & \vdots & \ddots & 0 \\ h(n\Delta t) & h((n-1)\Delta t) & \dots & h(\Delta t) \end{bmatrix};$$

$$Q_{ice} = \begin{bmatrix} \Delta q_{p_1} \\ \Delta q_{p_2} \\ \Delta q_{p_3} \\ \vdots \\ \Delta q_{p_n} \end{bmatrix} = \begin{bmatrix} q_p(\Delta t) - q_p(0) \\ q_p(2\Delta t) - q_p(\Delta t) \\ q_p(3\Delta t) - q_p(2\Delta t) \\ \vdots \\ q_p(n\Delta t) - q_p((n-1)\Delta t) \end{bmatrix}; \tag{5.22}$$

where n is the number of time steps. The dynamic response of a system is dependent on the changes in applied load (Ikonen *et al.*, 2014). Therefore Q_{ice} in Equation 5.22 is defined by the changes in moment between the current time step t and previous time step $t - \Delta t$. The impulse response matrix H between the externally applied load on the propeller and the internal torque in the shaft line at the point of measurement can be determined from the unit response function values with damping applied. The matrix can be rewritten as

$$H = \begin{bmatrix} q_{shaft}(\Delta t) & 0 & \cdots & 0 \\ q_{shaft}(2\Delta t) & q_{shaft}(\Delta t) & \cdots & 0 \\ q_{shaft}(3\Delta t) & q_{shaft}(2\Delta t) & \cdots & 0 \\ \vdots & \vdots & \ddots & \vdots \\ q_{shaft}(n\Delta t) & q_{shaft}((n-1)\Delta t) & \cdots & q_{shaft}(\Delta t) \end{bmatrix} \tag{5.23}$$

where the matrix sub-entries $q_{shaft}(t)$ are the values obtained from the unit response function for the different time steps. In order to solve for the propeller-ice load vector Q_{ice} from shaft line measurements Q_{shaft}, Equation 5.21 can be rearranged as

$$Q_{ice} = H^{-1} Q_{shaft} \tag{5.24}$$

This equation seems straightforward through matrix operations, however the inverse of the impulse response matrix H cannot easily be determined as it is ill-posed. The stability of a system is determined through its condition number, which is obtained by dividing the largest singular value by the lowest singular value of the system. The condition number of H for the present application was of the order 10^{19}. A condition number greater than one represents an unstable system and the larger the condition number the more unstable the system is (Ikonen *et al.*, 2014). The inverse of an ill-conditioned matrix will result in unstable results with regards to small disturbances such as noise, which will be magnified in the solution through the measured signal (Jacquelin *et al.*, 2003). Inverse methods are therefore required to solve this problem.

5.1.2 Inverse method

Inverse methods have been investigated in order to perform indirect force determination in an impact loading situation of a dynamic structure. The complication with discretization of inverse problems is that it leads to a highly ill-conditioned coefficient matrix for the system of linear equations, therefore requiring regularization methods to obtain stable solutions (Golub *et al.*, 1999). Regularization is the procedure whereby the initial problem is modified to reduce the sensitivity of the response and obtain a robust solution (Jacquelin *et al.*, 2003). This will be achieved through the implementation of three regularization methods, namely singular value decomposition (SVD), generalized singular value decomposition (GSVD) and Tikhonov regularization.

SVD is a common method used to regularize ill-posed systems. The SVD of $H \in \mathbb{R}^{m \times n}$, where $m \geq n$, can be defined as (Hansen, 2001):

$$H = U\Sigma V^T = \sum_{i=1}^{n} u_i \sigma_i v_i^T \tag{5.25}$$

The ability to solve a system is therefore dependent on the singular values and vectors of H. There exists different kinds of ill-conditioning, whereby a system that contains singular values that decay gradually to zero with no discontinuity is ill-posed. However, if there is a well-determined discontinuity between two singular values, the system is rank-deficient as well (Jacquelin *et al.*, 2003). In order to determine the inverse of the ill-posed matrix H, the closest well-conditioned approximation will be obtained by reducing the rank and ignoring low-quality information. This is achieved through the truncated SVD whereby singular values before the discontinuity are kept and the rest are set equal to zero (Hansen, 2008). Equation 5.25 can be rewritten to obtain the desired solution through the truncated SVD method, where j is the number of singular values retained (Hansen, 2008):

$$Q_{ice} = \sum_{i=1}^{j} \frac{u_i^T q_s}{\sigma_i} v_i, \qquad j \leq n \tag{5.26}$$

GSVD is a more sophisticated method whereby further information about the desired solution can be incorporated to stabilize the problem (Jacquelin

et al., 2003). This is achieved through the regularization matrix L which often takes the form of the first or second derivative operator (Golub *et al.*, 1999). Ikonen *et al.* (2014) found the second order derivative to be the best for the present application which is defined as:

$$L = \begin{bmatrix} -1 & 1 & 0 & \cdots & 0 \\ 0 & -1 & 1 & \cdots & 0 \\ \vdots & \vdots & \ddots & \ddots & \vdots \\ 0 & 0 & \cdots & -1 & 1 \end{bmatrix} \tag{5.27}$$

The system can be defined from the real matrix pair ($H \in \mathbb{R}^{m \times n}$ and $L \in \mathbb{R}^{p \times n}$) with $m \geq n \geq p$ (Dykes and Reichel, 2014):

$$H = U \begin{bmatrix} \Sigma & 0 \\ 0 & I_{n-p} \end{bmatrix} X^{-1} \tag{5.28}$$

$$L = V \left(M, 0\right) X^{-1} \tag{5.29}$$

The desired solution can be obtained by applying the truncated GSVD, which is similar to the truncated SVD wherein the number of singular values is reduced to j (Hansen, 2008):

$$Q_{ice} = \sum_{i=p-j+1}^{p} \frac{u_i^T q_s}{\sigma_i} x_i + \sum_{i=p+1}^{n} \left(u_i^T q_s\right) x_i \tag{5.30}$$

Another widely used regularization method is the Tikhonov's regularization method, which involves a least squares problem. This method is convenient for problems in which both the coefficient matrix and the required solution can only be determined approximately (Golub *et al.*, 1999). This method filters out the unwanted components corresponding to small singular values by adding damping to each SVD component of the solution (Golub *et al.*, 1999). The formula for this method is (Golub *et al.*, 1999):

$$\min\{||HQ_{ice} - Q_{shaft}||_2^2 + \lambda ||LQ_{ice}||_2^2\} \tag{5.31}$$

where λ is a positive constant referred to as the regularization parameter. The required solution for load vector Q_{ice} will be the one that minimizes Equation 5.31.

5.2 Known moment impulse

To validate whether the applied regularization methods are correct, a known ice moment impulse was applied as described by Ikonen *et al.* (2014). This has three purposes: firstly, the feasibility of the method is evaluated; secondly, the optimum levels of regularization for the application of real data can be determined and thirdly, the different methods can be compared to one another to determine the most appropriate one. The known moment impulse is chosen to have strong similarities to that of a real ice induced loading moment, but an actual ice induced loading moment cannot be used due to the exact shape and number of consecutive ice contacts being unknown. This shape can either have a sharp peak or a round peak. Therefore a linear impulse of 40 ms duration and a peak of 200 kN · m were used, as well as a half sine impulse also of 40 ms duration and a maximum value of 175 kN · m. The duration of the impulse was based on the modelled torque excitation for 90 degree single blade impact sequence for four bladed propellers in Ice Class Rules by Det Norske Veritas (2011*a*). This impulse duration was also chosen by Ikonen *et al.* (2014), enabling a comparison of the results obtained. These impulses are presented in Figure 5.4a.

The current dynamic model applies the change in external moment, therefore the first derivative of the known moments need to be determined. This was done with a time step of 2 ms, the equivalent to a sample frequency of 500 Hz, as presented in Figure 5.4b. The change in external known moment will be applied to the dynamic model and the response recorded at the shaft line location. This response will then be passed through the inverse methods in order to obtain the estimated external moment. When performing these methods, it is important to avoid the concept of inverse crime. This occurs when the same, or very similar, theoretical information is employed to synthesize and invert data in an inverse problem (Wirgin, 2004). This will provide unrealistically good results that will only work for the current data set. In order to avoid this, Ikonen *et al.* (2014) suggested adding deviations to the verification data. Two types of deviations were added. Firstly, ±10% deviations were added to the inertia and torsional spring constants, which resembles the uncertainty

of the dynamic model. Secondly, random deviations of ±650 Nm were added to each data point of the verification data to model the uncertainty of the strain gauge measurements. This value corresponds to ±1% of the maximum measured internal torque due to ice induced loading.

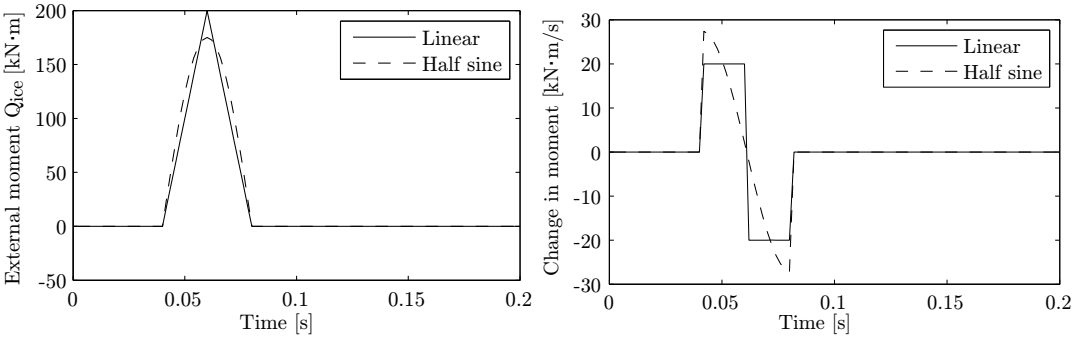

Figure 5.4: Known linear and half sine moment impulses of 40 ms duration presented as (a) a function of time and (b) the first derivative.

In order to apply inverse methods, the regularization parameters needed to be determined. This was done through the L-curve in which the semi-norm is plotted against the residual norm and the optimal values located at the corner of the curve. If too much regularization is applied, then the solution will not fit the desired curve properly and if too little regularization is applied then the solution will fit the desired curve well but will be dominated by the contribution from the data errors (Hansen, 2001). The L-curve will therefore be used to find the best compromise between the two quantities that need to be controlled.

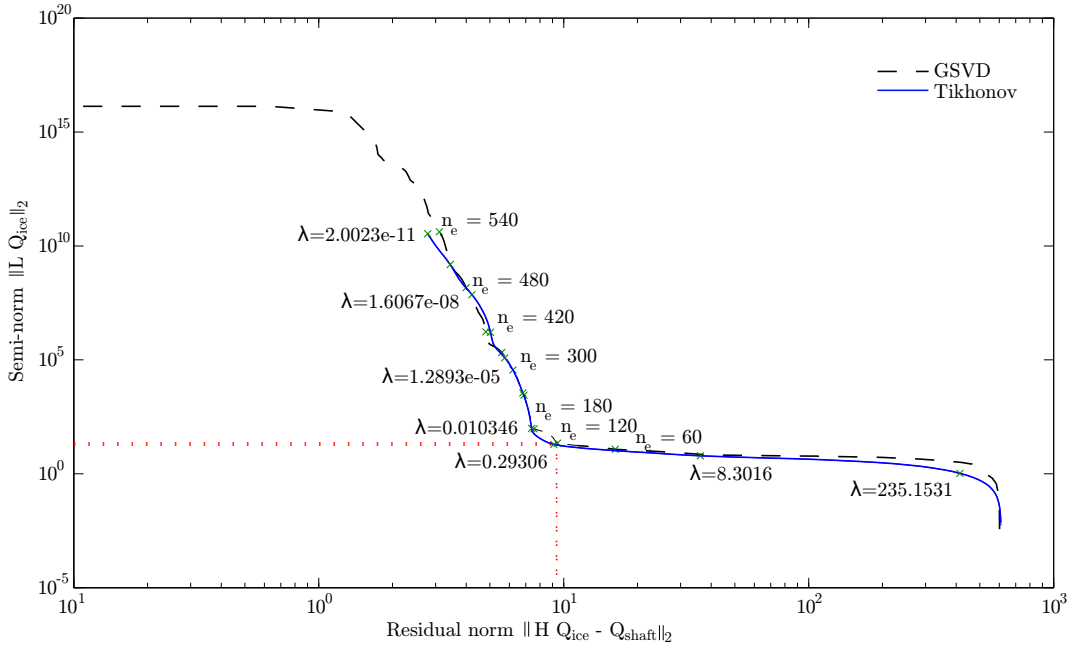

Figure 5.5: Comparison of GSVD and Tikhonov L-curves for a linear moment impulse.

This plot is only applicable for GSVD and Tikhonov as SVD does not implement the L matrix. The zero, first and second order regularization matrix L was evaluated for the current model and it was determined that the first order regularization matrix provided the best results for all three inverse methods. The optimum number of non-zero eliminated singular values for GSVD was determined to be $n_e = 120$ and the optimum regularization parameter for Tikhonov was determined to be $\lambda = 24.57 \times 10^{-2}$, as presented in Figure 5.5. These parameters were very different to that of Ikonen *et al.* (2014) as the compact truncated methods were used for the current model. Compact refers to retaining only the non-zero eigenvalues with the corresponding eigenvectors and truncated refers to the process of eliminating undesirable singular values by reducing the rank of the matrix. These regularization methods were implemented using algorithms written by Hansen (1998). The L-curve is only presented for the linear moment impulse as the half sine moment impulse provided similar results.

A comparison of different GSVD regularization values around the optimum value ($n_e = 120$) from the L-curve are presented in Figure 5.6. The reference

moment was initially described to be a linear moment impulse with a peak of 200 kN · m, however in Figure 5.6 it only has a peak of 173.6 kN · m. This is attributed to the water damping moment applied to the propeller. It is expected of regularization to damp sharp peaks in the solution, however the aim is to minimise this damping while maintaining the best curve fit to the remaining data. For $n_e = 70$, the signal deviated from the reference moment and had a -14.80% lower peak value compared to the reference moment. For $n_e = 170$, only a -4.03% difference in peak value was obtained but resulted in greater oscillations about the reference moment. It was therefore confirmed that the optimal number of eliminated singular values was $n_e = 120$, which followed the reference moment well and resulted in a peak difference of -5.53%.

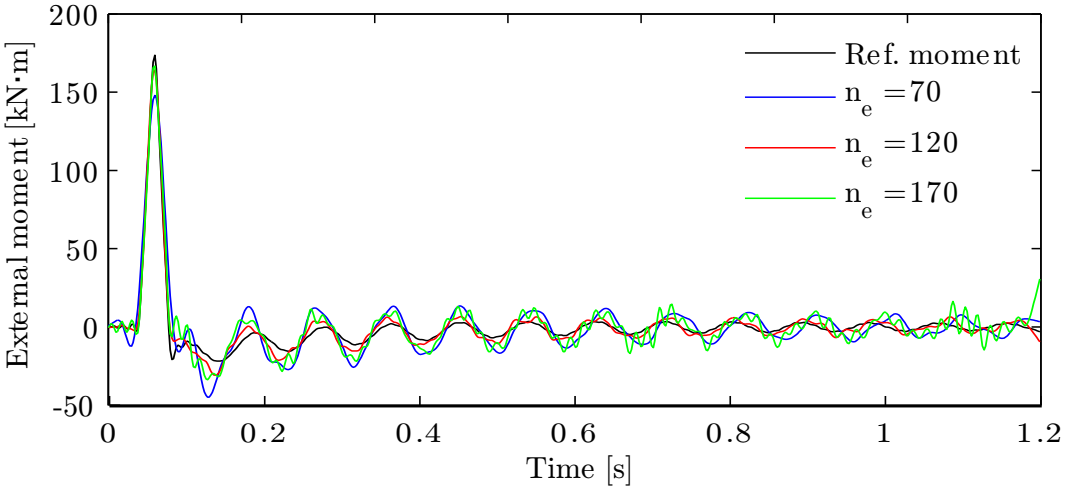

Figure 5.6: Comparison of varying regularization levels for GSVD. The reference moment (Ref. moment) was obtained from the linear moment impulse with propeller damping added. n_e represents the number of non-zero eliminated singular values.

The same method of comparison was done for Tikhonov regularization with similar results observed. A regularization parameter of $\lambda = 14.57 \times 10^{-2}$ resulted in the smallest peak difference of 1.21% compared to the reference moment but had the greatest deviations after the peak. For $\lambda = 34.57 \times 10^{-2}$ there was a slight phase shift and a greater peak difference of 7.20% but resulted in a much better fit to the reference curve. The phase shift could be due to the deviations applied to the inertias and spring constants. The

optimum regularization parameter was found to be $\lambda = 24.57 \times 10^{-2}$, which resulted in a -2.65% difference in peak value compared to the reference moment.

These regularization methods have been tested for single propeller-ice impacts, however multiple ice impacts are also a common occurrence, especially during milling. It is therefore necessary to test whether these methods will function properly for consecutive linear and half sine moment impulses. The optimally determined parameters for GSVD and Tikhonov were used, with the GSVD parameter used for the SVD. The results for consecutive linear and half sine moment impulses were similar, with the consecutive linear moment impulse graph presented in Figure 5.7. The percentage relative difference between the different regularization methods and the reference moment was recorded in Table 5.2, from which it is clear that GSVD resulted in the lowest percentage peak difference. Therefore GSVD was found to have the best peak representation, but Tikhonov regularization was found to have the best curve-fit capabilities for the current application.

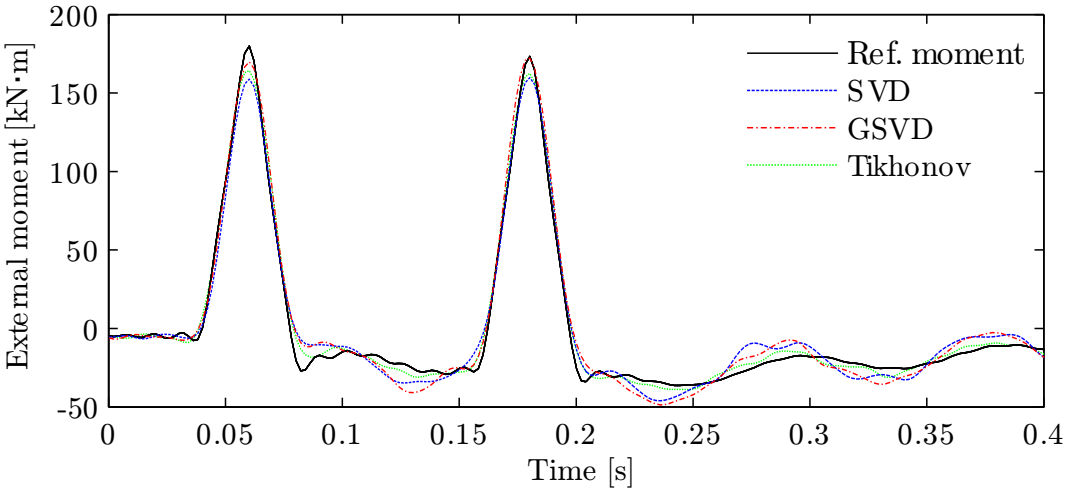

Figure 5.7: Comparison of SVD, GSVD and Tikhonov regularization methods for consecutive linear moment impulses. SVD and GSVD was applied with $n_e = 120$ and Tikhonov with $\lambda = 24.57 \times 10^{-2}$.

Table 5.2: Percentage differences between SVD, GSVD and Tikhonov relative to the reference moment for consecutive linear and sine moment impulses.

	Linear		Half sine	
	First peak	Second peak	First peak	Second peak
SVD	-11.35%	-7.63%	-3.49%	-6.64%
GSVD	-5.41%	-0.62%	1.60%	-2.07%
Tikhonov	-8.51%	-6.09%	5.68%	6.80%

Further validation of the current model for a milling condition was implemented through the IACS Case 1 for 4 bladed propellers during 90° single-blade impact sequence, presented in Figure 2.6. Rolls-Royce AB (2010*b*) used this case to validate the design of the SAA II shaft line prior to building, with the result for the motor shaft internal torque presented in Figure 5.8a. The same input without hydrodynamic load was applied to the current dynamic model with the results presented in Figure 5.8b. The current dynamic model uses the assumption of zero initial conditions and can therefore not be implemented with the hydrodynamic load. It only represents the ice induced loading during operations and could account for the difference between the results of the two models. There is however a similar pattern in the response of the shaft line.

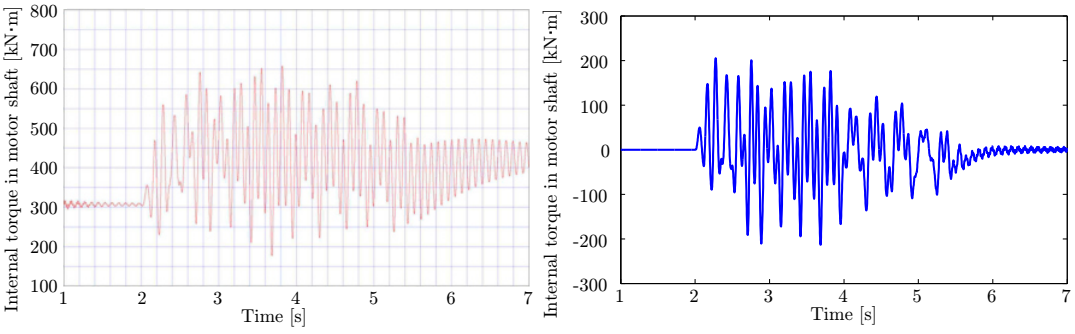

(a) (b)

Figure 5.8: Comparison of motor shaft response through IACS Case 1 milling condition between (a) Rolls-Royce AB (2010*b*) and (b) current model.

5.3 Full-scale measurements

Three different propeller-ice interaction conditions have been selected in order to test the stability of the inverse methods on full-scale measurement data

Q_{shaft}. For all cases the propeller pitch was approximately 88%. The operating conditions are presented in Table 5.3, with the measured internal torque plotted against the inverted torque in Figure 5.9. The hydrodynamic torque was subtracted from the measured internal torque and the direction of the moment inverted to obtain a positive external ice induced loading on the propeller. The inverted internal torque was obtained by determining the relevant external moment through the Tikhonov method and using this result as an input to the dynamic model to obtain the internal torque. The inverted torque follows the measured torque well (Figure 5.9), with sharp peaks being damped, which is expected from regularization methods.

Table 5.3: Operating conditions during three propeller-ice impact conditions with 88% propeller pitch on 12 for Case 1 and 2 and 13 December 2015 for Case 3. Average values of machine control data for the ice contact duration and hydrodynamic torque (H. torque) at the start of the ice contact condition are presented.

Case no.	Time [hh:mm:ss]	Speed [knots]	H. torque [kN·m]	Motor speed [rpm]	Motor power [kW]
1	09:27:16	5.0	219.2	109.0	2270.0
2	09:52:53	5.4	145.0	94.3	1313.3
3	07:46:45	6.6	310.7	130.0	4073.0

Inverse methods have been applied to the three measured propeller-ice impact cases in order to determine the relevant external propeller loads Q_{ice}, presented in Figure 5.10. The optimal values for regularization parameters n_e and λ were determined through the L-curve and found to be the same as for the known moment impulses. All three methods provided similar results, except Case 3 for which Tikhonov regularization method resulted in more oscillations compared to SVD and GSVD method. From the known moment impulses, it was determined that Tikhonov followed the reference curve the best and therefore should provide the best representation of the inversed external moment.

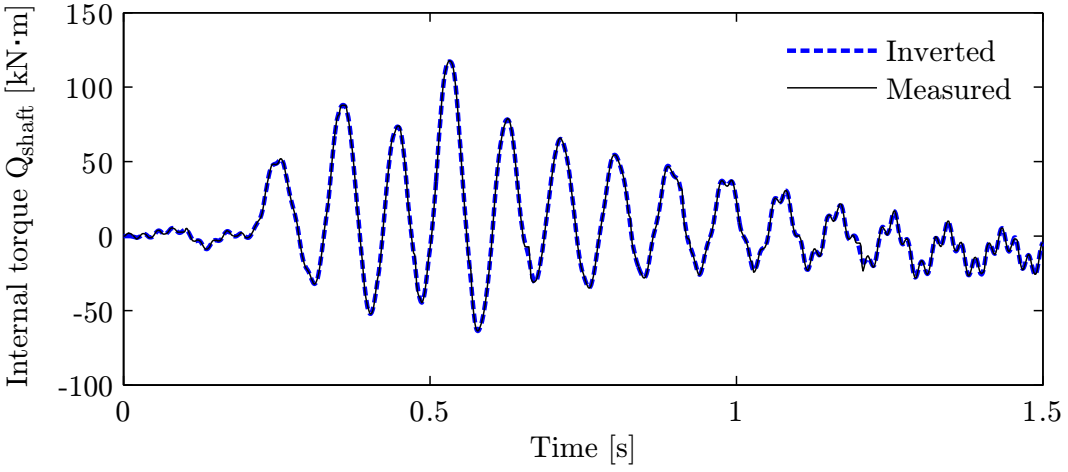

(a) Case 1

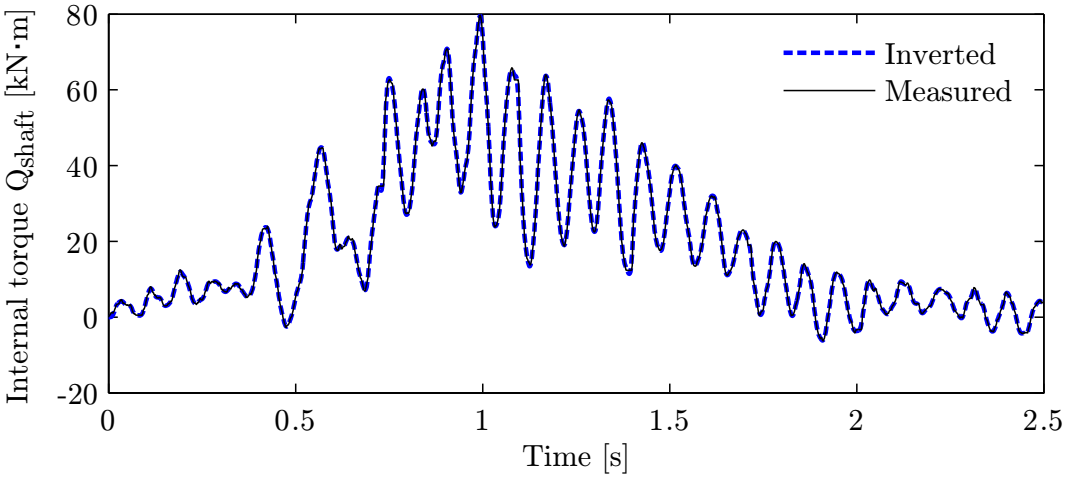

(b) Case 2

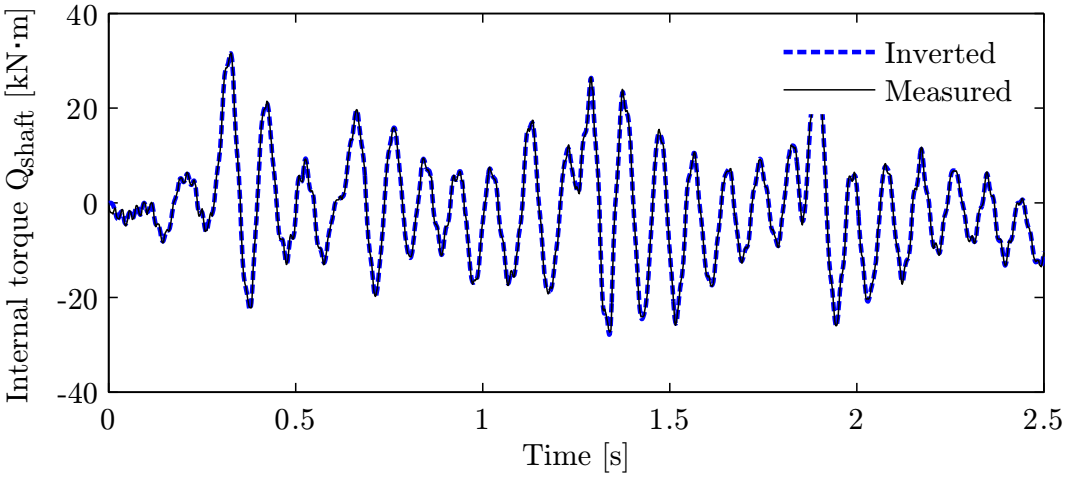

(c) Case 3

Figure 5.9: Measured internal torque and inversely determined internal torque for three propeller-ice impact cases of different durations and varying operating conditions.

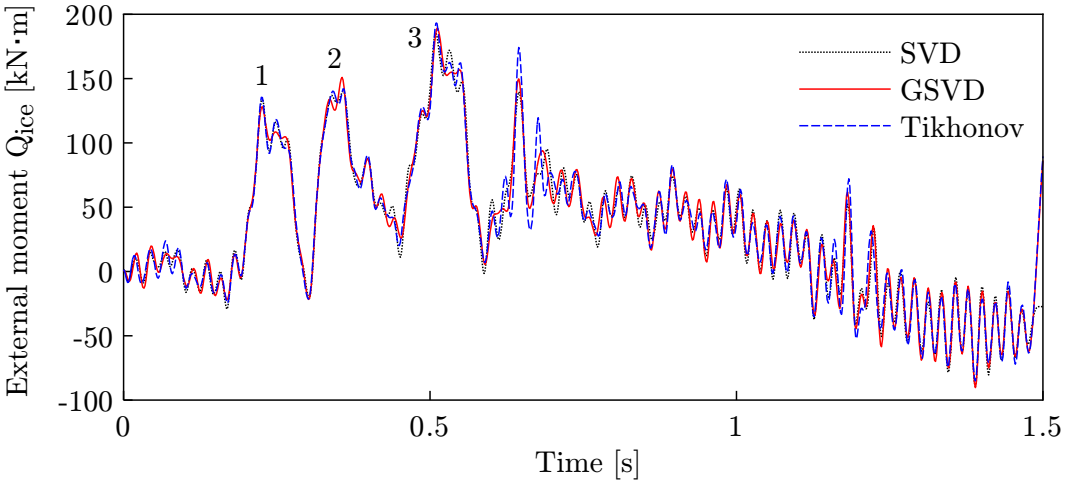

(a) Case 1

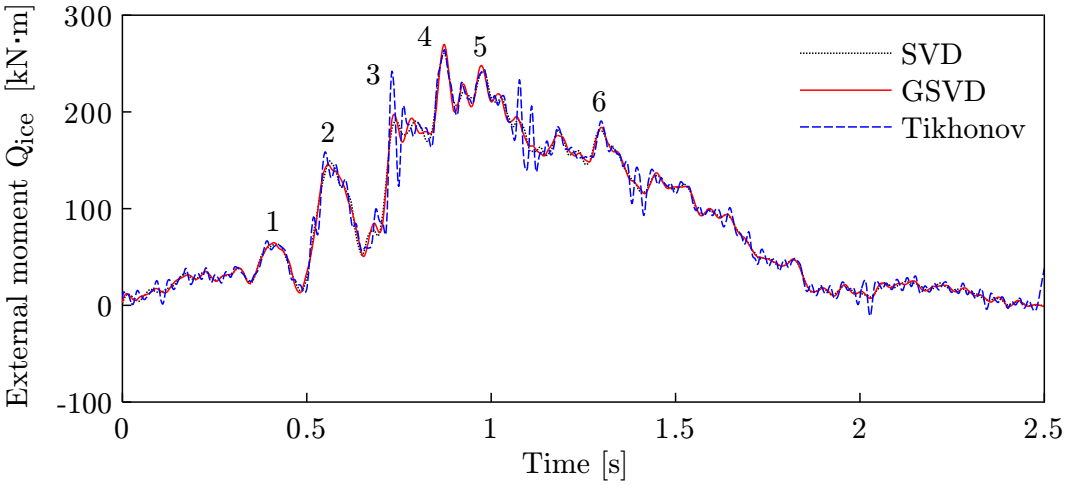

(b) Case 2

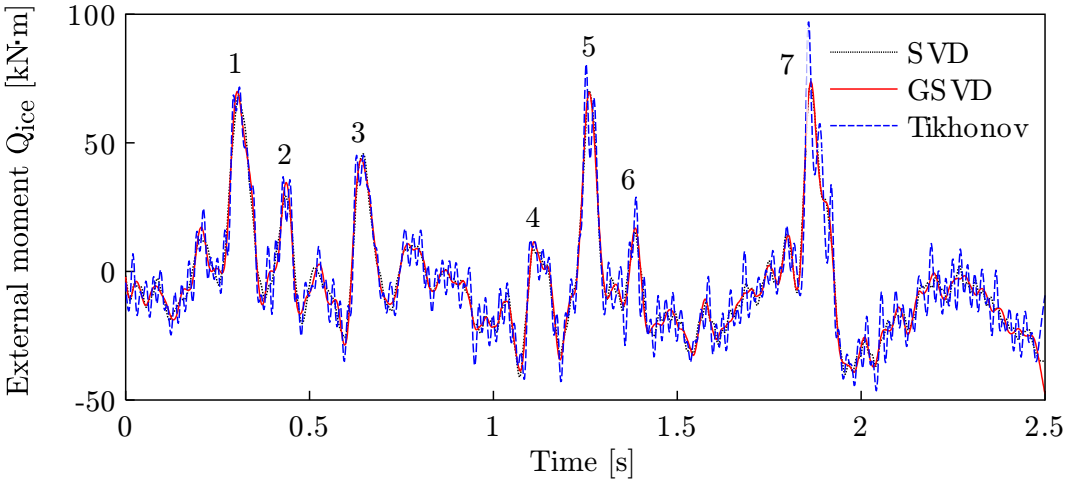

(c) Case 3

Figure 5.10: External propeller moment determined through inverse methods SVD, GSVD and Tikhonov regularization.

From the inversely determined external moments Q_{ice}, the number of impacts, the duration, the shape and the damping of water on the propeller was identifiable. In general, an ice impact initiates a rapid increase in amplitude followed by a rapid decrease. However, the peak does not immediately damp down to zero. There is a secondary peak evident which is usually smaller than the first. This secondary peak occurs between 15 ms and 47 ms after the first peak for the current conditions. The cause of this secondary peak is explained by Ikonen *et al.* (2014) to possibly be the shear stress wave that propagates back and forth from the propeller to the engine rotor. When this shear stress wave reaches the propeller again, it results in the blade of the propeller applying an impulsive load to the ice block. The propagation speed of a wave in a linearly elastic medium is defined by (Jensen *et al.*, 2011):

$$K_b = \rho c_p^2 \tag{5.32}$$

with (Hibbeler, 2011):

$$K_b = \frac{E}{3(1-2\nu)} \tag{5.33}$$

where K_b is the bulk modulus of elasticity, ρ the material density, c_p the propagation speed, E the modulus of elasticity and ν Poisson's ratio. Using the variables from Rolls-Royce AB (2010*c*) for $E = 210\,\text{GPa}$, $\rho = 7850\,\text{kg/m}^3$ and Budynas and Nisbett (2011) for $\nu = 0.29$ for steel, the propagation speed is 4607.76 m/s. For the 35.1 m long shaft, this translates to a duration of 15 ms, the time it takes the wave to propagate back and forth along the shaft. This coincides with the smallest duration measured between the first and second peak in the external ice induced moments. However, the exact location of the ice impact on the blade of the propeller and the propagation through the blade is unknown, which could account for the longer propagation time for some of the secondary peaks.

In Figure 5.10, the number of ice impacts is more easily determined compared to the measured internal torque as the dynamic response of the shaft line is not included in the external loads. For the first case, three ice impacts are clearly evident (numbered 1 to 3) followed by two smaller impacts. For the second case, individual ice impacts were not as prominent as the effect of milling causes multiple impacts to occur shortly after one another. A total of

six impacts were confidently determined for this case (numbered 1 to 6). In case three there were seven prominent ice impacts (numbered 1 to 7). The duration of ice impacts for these three cases ranged from 25 ms to 228 ms, where the duration was based on the minimum turning point before and after the first peak caused by the ice impact. From blade measurements performed by Jussila and Koskinen (1989) on a car ferry in the archipelago of Åland, ice impact durations of around 40 ms were recorded, thus similar to the durations determined for the current cases.

When analysing the maximum amplitudes for external ice induced moments Q_{ice} and measured internal torque Q_{shaft} for these cases, the external moments were consistently found to have greater peak values. This is due to the water damping and dynamic model of the shaft line. For Case 1, Q_{ice} was found to be 64.2% greater compared to the relative measured Q_{shaft}. However for Cases 2 and 3, this increase was found to be 231.0% and 206.6%.

5.4 Maximum conditions

The maximum recorded ice induced torque during the respective voyages for the SAA II and Polarstern is presented in Figure 5.11. The maximum thrust loading on the shaft occurred during cavitation for both vessels. These plots were obtained by subtracting the hydrodynamic load from the measured signal. The operating conditions for these cases are recorded in Table 5.4. From the Ice Class Rules, equations for obtaining the maximum forward F_f and backward F_b forces on the propeller blades could be obtained using Equation 2.8 to 2.11. These forces are translated to applied thrust, on the shaft at the location of the propeller, by multiplying the magnitudes by 1.1 (Det Norske Veritas, 2011*a*). The backward bending forces on the blades cause tension in the shaft and forward bending forces compression.

The calculated forward and backward bending forces for the SAA II and Polarstern are recorded in Table 5.4. The relative applied thrust caused by these forces are presented in Figure 5.11 with red dashed lines. The SAA II thrust exceeded the maximum ice induced tension thrust by 79.7% and the

Polarstern by 6.8%. The Polarstern thrust also exceeded the maximum ice induced compression thrust by 47.8%. The reason for the measured data exceeding these limits could be attributed to the fact that the transmissibility between the end of the shaft and the measured location was not taken into account in the calculations. However this transmissibility could not be determined due to the limitation of required variables and requires further investigation. It is important to note that the thrust conditions were induced by cavitation and are currently being compared to ice related calculations. This does however emphasise the importance of accounting for cavitation during the design phase of the vessel. The absolute maximum values for these cases including the hydrodynamic load is recorded in Table 5.4.

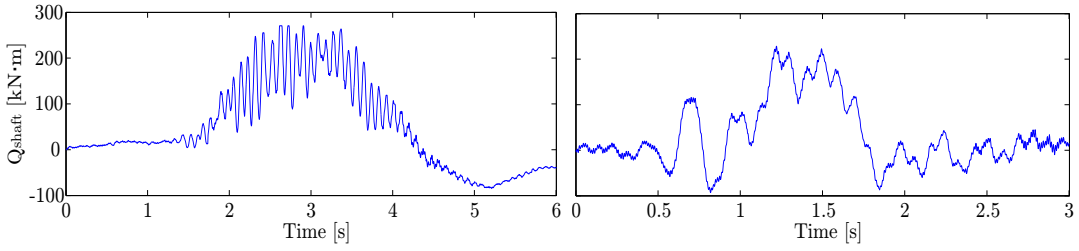

(a) SAA II - torque (b) Polarstern - torque

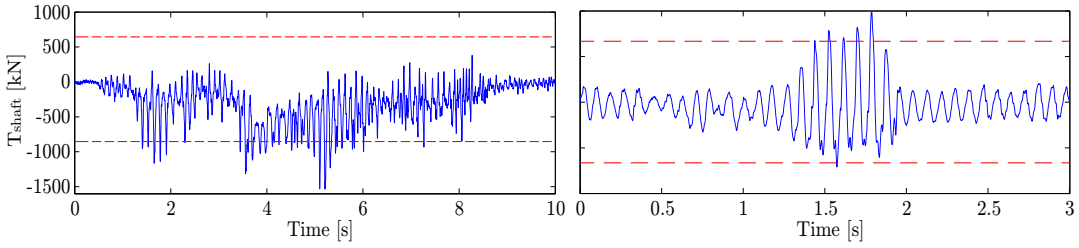

(c) SAA II - thrust (d) Polarstern - thrust

Figure 5.11: Maximum ice induced internal shaft loads for the SAA II and Polarstern over different time intervals. The red dash lines represent the maximum applied thrust from propeller bending forces.

The maximum ice induced external torque for the SAA II was determined through inverse methods from the measured internal torque and presented in Figure 5.12. Milling was evident for this case from the multiple ice impacts occurring shortly after one another. The maximum allowed ice induced torque on the propeller was determined through the Ice Class Rules, from Equation 2.4, to be 1009.9 kN · m. For SVD and GSVD, Q_{ice} did not exceed this

limit, however for Tikhonov this limit was exceeded by 12.6%. It was previously determined that Tikhonov regularization results in a maximum error for the known moment impulses of 6.8% and GSVD 1.6%. It was also determined that GSVD better represented the peak values and Tikhonov provided a better general fit to the required data. Therefore the GSVD should be used for peak value estimation, resulting in the maximum external ice induced moment occurring at 941.5 kN · m, 6.8% below the maximum allowed ice induced torque on the propeller.

Table 5.4: Operating conditions for vessels during maximum recorded ice induced torque loading and maximum cavitation induced thrust loading.

	SAA II		Polarstern	
	Torque	Thrust	Torque	Thrust
Date	2015/12/11	2015/12/15	2016/08/31	2016/09/01
Start time	16:50:47	15:16:35	19:04:54	14:07:05
Pitch	69.67%	31.3%	-	-
Shaft speed	85.1 rpm	143.2 rpm	173.0 rpm	175.0 rpm
Motor power	670.3 kW	1161.9 kW	-	-
Vessel speed	3.8 knots	2.9 knots	6.3 knots	5.8 knots
Hydro load	222.1 kN · m	113.2 kN	309.8 kN · m	519.4 kN
Max ice load	270.7 kN · m	379.2 kN	228.3 kN · m	986.8 kN
Min ice load	−84.7 kN · m	−1532.9 kN	−93.1 kN · m	−710.2 kN
Absolute max	492.9 kN · m	1419.7 kN	538.1 kN · m	1506.2 kN
F_b	-	775.3 kN	-	604.7 kN
F_f	-	585.9 kN	-	607.2 kN

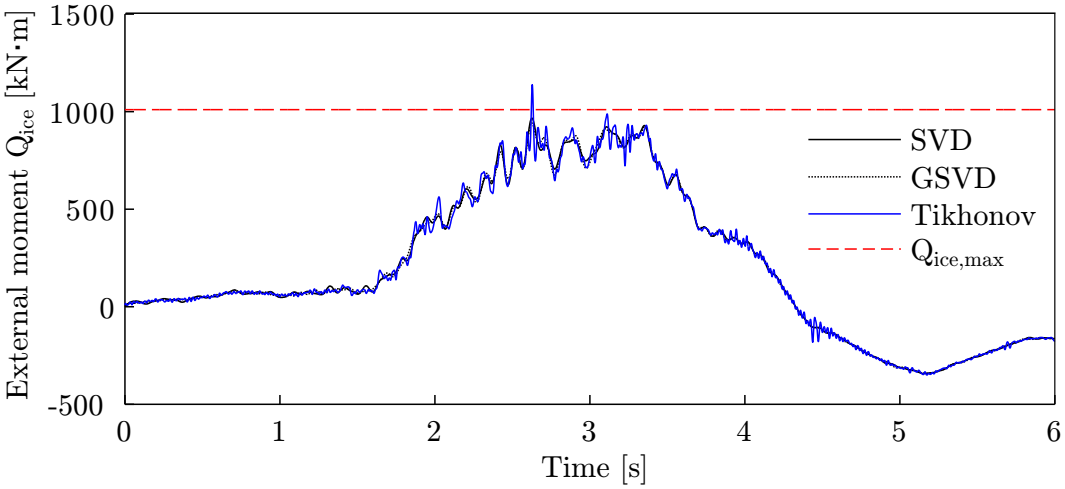

Figure 5.12: External moment determined from maximum measured internal torque for the SAA II.

A second ice loading case containing large torque oscillations was selected for analysis (Figure 5.13). The maximum measured internal torque for this case was 475.3 kN · m and the hydrodynamic load 254.3 kN · m. Different results were obtained compared to the previous case as the shaft line response torque had higher peaks compared to the determined external ice moment. Two other cases consisting of similar shaft line responses were tested and the same phenomena observed. This either demonstrates how the dynamic response of the shaft line can lead to higher internal torque loads compared to external ice induced loads or this is a shortcoming of the current regularization methods and requires further validation.

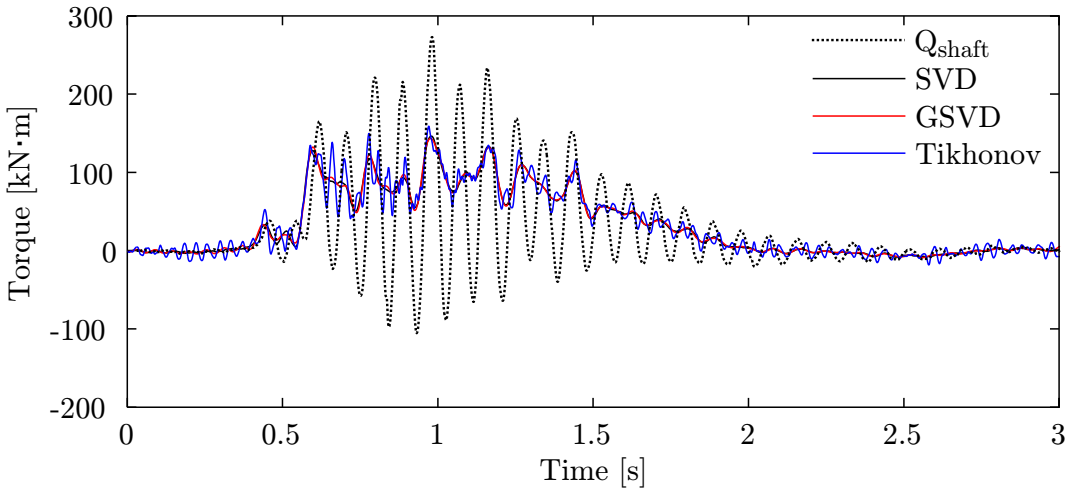

Figure 5.13: External moment determined through regularization methods for the SAA II on 12 December 2015 11h32m (SOG: 4.7 knots, shaft speed: 104.4 rpm, pitch: 87.9%, motor power: 1830 kW).

Chapter 6

Conclusion

Results from full-scale measurements on-board two Polar research vessels, the SAA II and Polarstern, were analysed and discussed. The Manner Telemetry system, which was used for shaft line measurements during the 2014/2015 voyage on-board the SAA II, was found to be unreliable. It is clear from the current study that during open water, cavitation and ice navigation, unique mechanisms are at work which result in noticeably different dynamic responses of the shaft line system. Ice impacts resulted in the largest torque measurements, with a maximum torque of 493 kN · m for the SAA II and 538 kN · m for the Polarstern. Cavitation resulted in the highest thrust loads of 1420 kN for the SAA II and 1506 kN for the Polarstern. The present investigation determined that cavitation can be identified from acceleration measurements in the fore-aft (x) direction on the shaft line radial bearings.

Inverse calculations were performed using three regularization methods, namely SVD, GSVD and Tikhonov. It was found that the internal torque for ice infested waters resulted in erratic torque responses, with the inversely determined external propeller-ice loads being characterized by overall greater peaks. An exception to this was during large amplitude oscillations about the hydrodynamic load, either demonstrating the ability of the shaft line dynamic response to induce higher internal torque loads compared to external ice induced loads, or this is a shortcoming of the current regularization methods and requires further validation. Of the three regularization methods used for

inverse force estimation, GSVD was found to represent impulse moments the best with a maximum error of -5.4%. Tikhonov regularization matched the reference moment the best overall with a maximum error of -8.5% during the linear impulse moment.

The highest ice-induced external moment for the investigated case studies were found to be 941.5 kN · m through the GSVD, which was 6.8% less than the maximum allowed ice induced torque on the propeller. The duration of these ice impacts ranged from 25 ms to 228 ms. A secondary peak was evident during propeller-ice impacts which is thought to be a shear stress wave that propagates back and forth along the shaft line. From the inversely determined ice-induced loads, the number of impacts, the duration, the shape and the damping of water on the propeller was identifiable.

For future work, it is recommended to:

1. Design a numerical model with increased precision. This would involve parameter optimization to enable better matching natural frequencies. Inverse force estimation could subsequently be performed to determine the propeller loads, more exact damping on the propeller during operation and improved regularization methods.
2. Build a scale model through which the inverse methods could be verified.
3. Inversely determine axial excitation induced by propeller-ice impacts from thrust measurements.
4. Perform shaft line recordings in more locations to better validate the numerical model.
5. Obtain continuous recordings during full scale measurements for better and more reliable load profiling.
6. Design an algorithm that is able to identify ice impacts and cavitation to reduce the required time to locate these phenomena.
7. Record more reliable and higher resolution shaft line speed measurements to validate whether torque impulses are due to ice impacts or other factors such as machine control parameters.

Appendix A

Data Validation

During the 2014/2015 voyage, torque and thrust data on the SAA II shaft line was recorded using a Manner Telemetry system. The data contained many peaks and the sample rate varied, resulting in questionable data. The purpose of this investigation was to determine if this data was reliable through validation methods. A further measurement system was installed to accompany this validation process. The Manner Telemetry system did not correlate well with the analytical calculations or the second measurement system. These comparisons emphasised the inconsistency and unreliability of the Manner Telemetry system data and therefore this data was not used for further analysis. The system installed on the Polarstern also needed to be validated in order to ensure the reliability of the data.

A.1 Manner Telemetry raw data

Raw data from the Manner Telemetry system during the 2014/2015 voyage contained peaks at irregular and random intervals as indicated by the arrows in Figure A.1a. During the 2012/2013 voyage to Antarctica, Myklebost and Dahler (2013) noted similar complications with the system and suggested the possible causes for these peaks could be attributed to interference from buffer overflow, electronic equipment or other hardware limitations. They suggested that the data values before and after the peak be taken and averaged to replace the questionable data. It was found that these peaks consist of multiple

consecutive data points which render this approach viable. Peaks were also found in the time vectors, as presented in Figure A.1b. The expected time vector should be an inclined straight line with a slope of Δt.

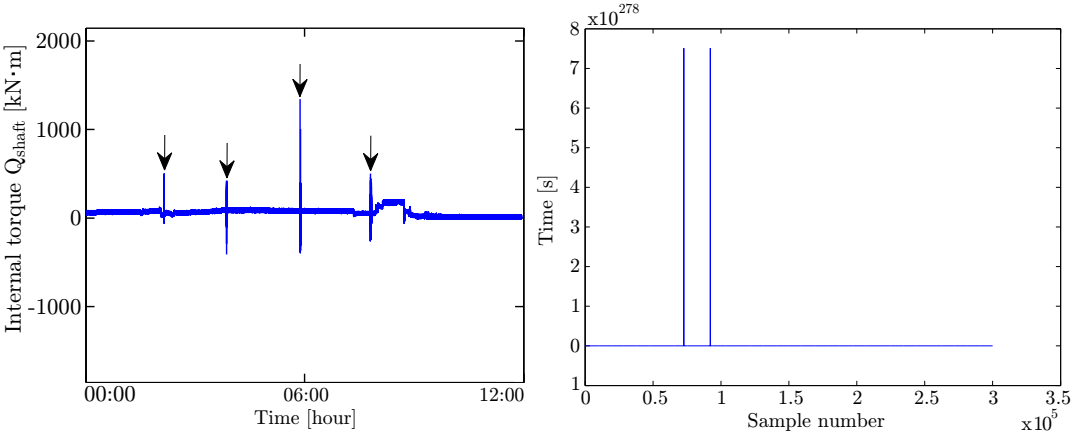

Figure A.1: Data with peaks measured on 6 January 2015 for (a) shaft line torque and (b) time from 15h50 to 16h00.

Measurements from the Manner Telemetry system were further questionable as a result of the maximum loads recorded during open water conditions. These loads exceeded the maximum ice induced torque on the propeller, as determined from the DNV Ice Class Rules (Equation 2.4), with the variables obtained from Table 3.2:

$$Q_{ice,max} = 1009.9\,\text{kN} \cdot \text{m} \tag{A.1}$$

where n was taken at the MCR due to the rotational speed at bollard condition being unknown, as suggested by Det Norske Veritas (2011*a*). Data from the Manner Telemetry system also appears to have clipped the maximum torque around $1030\,\text{kN} \cdot \text{m}$ and the minimum torque around $-985\,\text{kN} \cdot \text{m}$ as shown in Figure A.2a and A.2b. Whether this error is introduced through the A/D converter or the computer is unknown.

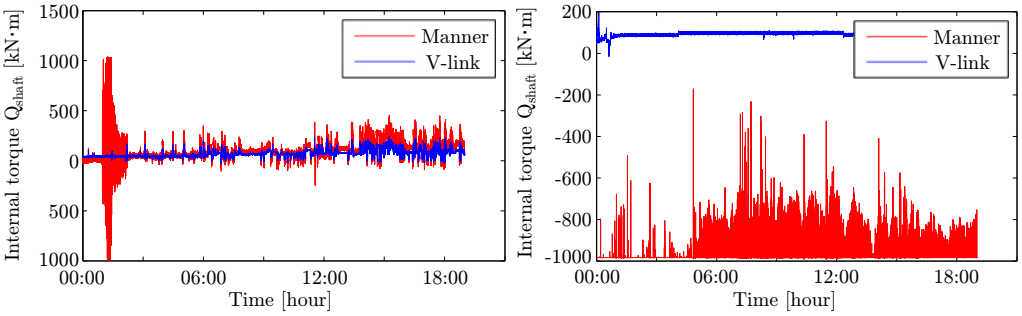

Figure A.2: Torque data from the Manner Telemetry system and V-link on (a) 12 December 2015 and (b) 2 February 2016.

When analysing the sample frequency of the Manner Telemetry system, it was found to be inconsistent, as presented in Figure A.3. A stable system should have a consistent sample frequency, in this case the Manner Telemetry system is expected to be recording at a 500 Hz.

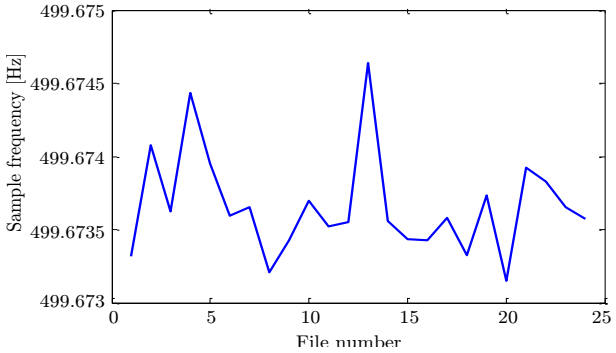

Figure A.3: Sample frequency per file for the Manner Telemetry system over one day on 15 December 2014.

Due to the inconsistent reliability of the Manner Telemetry system, additional case studies were introduced (Figure A.4). The Manner Telemetry data was compared to the V-link data and the numerical calculations determined. It is interesting to note that there was a reasonably strong correlation for torque on 6 December 2015 in Table A.1, however from Figure A.4b it is clear that the Manner Telemetry system had a large offset. This changed on 13 December 2015 whereby the torque had a strong correlation with the motor

torque in Table A.1 and very similar profiles in Figure A.4d. These comparisons emphasised the inconsistency and unreliability of the Manner Telemetry system data and therefore this data was not used for further analysis.

Table A.1: Correlation results for torque and thrust data

	Thrust		Torque	
	6 Dec	13 Dec	6 Dec	13 Dec
Manner vs V-link	-0.34	-0.08	0.78	0.95
Manner vs Numeric/Motor torque	0.75	0.69	0.78	0.65
V-link vs Numeric/Motor torque	-0.53	-0.11	0.78	0.66

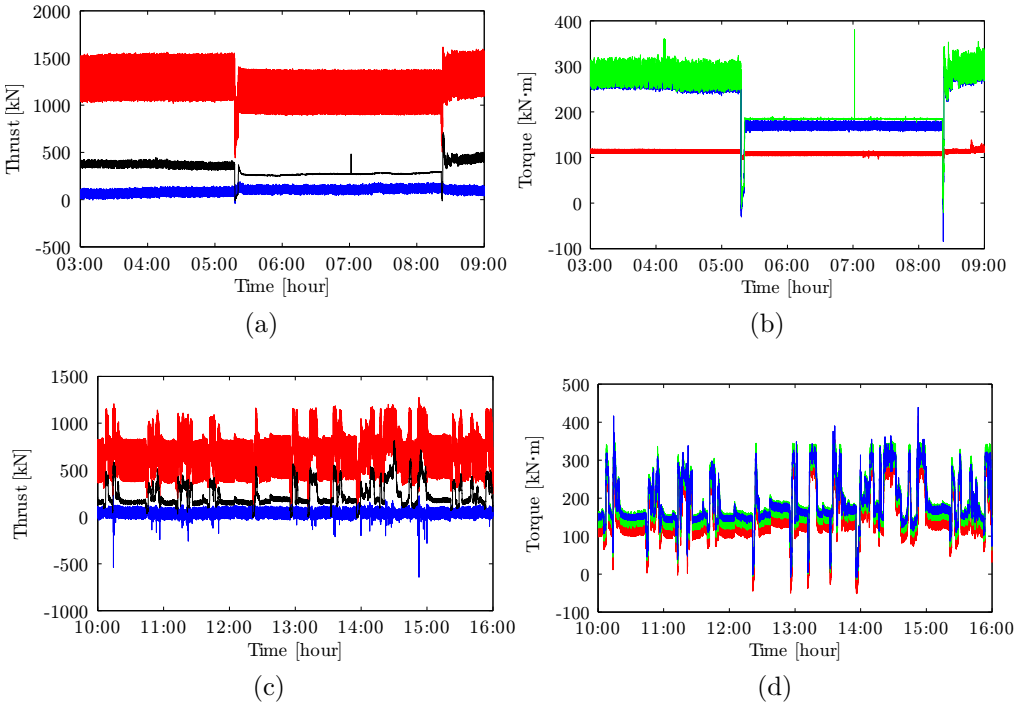

Figure A.4: Data comparison from 03h-09h on 6 December 2015 for (a) thrust and (b) torque (SOG: 6.3 knots, shaft speed: 123.9 rpm, pitch: 82.0%, motor power: 3017 kW), as well as data from 10h-16h on 13 December 2015 for (c) thrust and (d) torque (SOG: 6.8 knots, shaft speed: 112.0 rpm, pitch: 87.5%, motor power: 2160 kW). The Manner Telemetry data is represented by red, V-link blue, numerical thrust black and the motor torque green.

In addition, the frequency content up to 100 Hz for these two cases are presented in Figure A.5. Similar peaks were identified among the two data sets. However, for the Manner Telemetry system all the shaft line rotational orders

were dominant, masking the significant frequency content. From the torque graphs, Figure A.5b and A.5d, seven significant peaks could be identified from the V-link data. These were the shaft rotational speed (marker 1), the first torsional natural frequency (marker 2), the second torsional natural frequency (marker 3), first blade pass frequency (marker 4), second blade pass frequency (marker 5), six times the blade pass frequency (marker 6) and twelve times the blade pass frequency (marker 7). These frequencies were also identifiable in the Manner Telemetry data but were not as evident as shaft line rotational orders masked these frequencies.

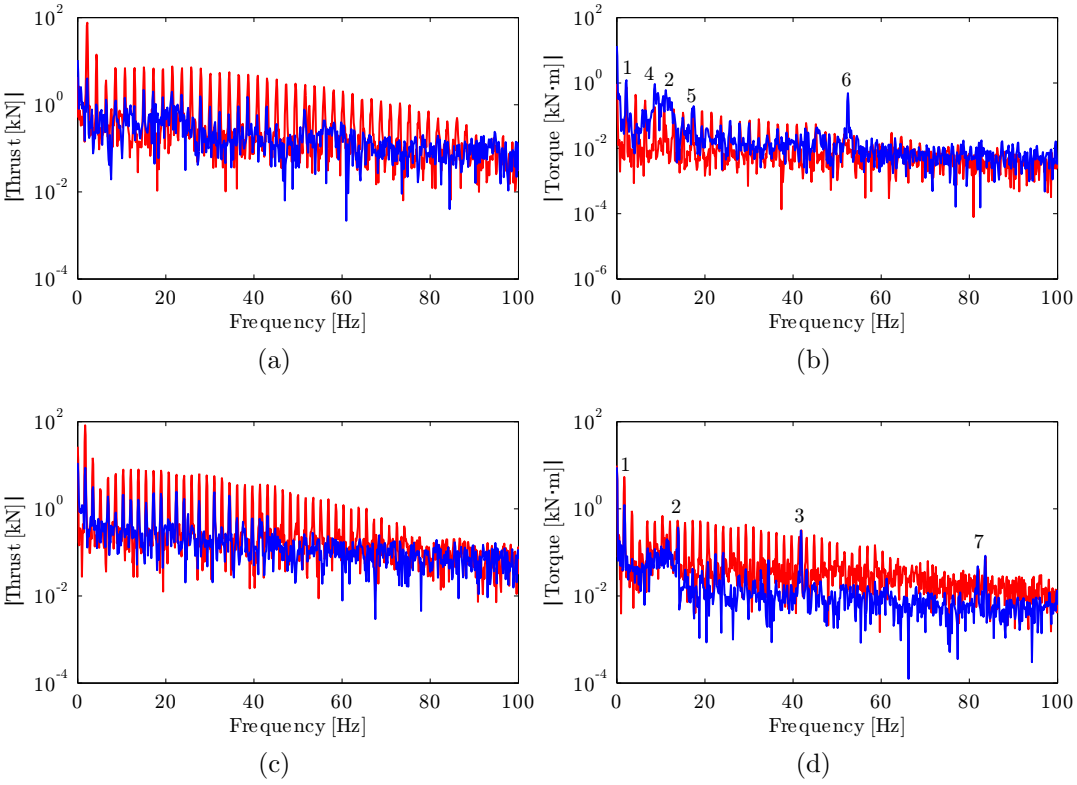

Figure A.5: Frequency analyses for 03h to 09h on 6 December 2015 for (a) thrust and (b) torque and 10h to 16h on 13 December 2015 for (c) thrust and (d) torque. The Manner Telemetry data is represented in red and V-link data in blue (Duration: 6 hours, Sample rate: 500 Hz - Manner Telemetry and 600 Hz - V-link, Block size: 4096, Window: Hanning, Overlap: 50%).

This effect was worse for the thrust frequency analysis (Figure A.5a and A.5c) wherein only the shaft rotational speed was dominant. The rotational

orders were only evident below 100 Hz. It is interesting to note that there appears to be a relationship between the correlation of the data and the relative magnitude of the rotational order. For the torque cases, there was a strong correlation between the measured data sets and a reduced influence from the shaft line rotational orders. For the thrust cases, there was a very weak correlation with greater shaft line rotational order influence. This illustrates that the resonance of the shaft line rotational orders contributes to making the Manner Telemetry system data unreliable.

A.2 Analytical calculations

In order to validate the V-link data, shaft line torque was compared to the motor output torque. It is realized that there exists a transmissibility between the two locations, however for this section this transmissiblity was neither measured nor modelled. The motor torque was calculated from the motor rotational speed and motor power, obtained from the machine control data, as presented in Equation A.2 (Budynas and Nisbett, 2011).

$$P_D = Q\omega \tag{A.2}$$

Thrust data from the V-link system was validated as presented by Matusiak (2013) to estimate the vessel resistance in water. These equations are based on the assumption that; resistance and thrust are of equivalent magnitude, there is a constant power delivered as well as a constant propulsive efficiency.

$$X_r = \frac{-R_T}{1-t_d} \tag{A.3}$$

$$R_T = \frac{P_D \eta_D}{V_s} \tag{A.4}$$

$$\eta_D = \eta_O \eta_R \eta_H = \eta_O \eta_R \frac{1-t_d}{1-w} \tag{A.5}$$

From Equation A.3 to A.5, the following relationship can be used to determine the propeller thrust, where efficiency losses due to off-design operational conditions are not taken into account (Matusiak, 2013):

$$T_{prop} = \frac{P_D \eta_O \eta_R}{V_s(1-w)} \tag{A.6}$$

Matusiak (2013) states that the vessel resistance equation could lead to unrealistically high values at low vessel speeds. Therefore two cases during open water where the vessel was sailing at speed was selected. The first case was on 5 December 2015 from 13h00 to 18h00 and the second was on 2 February 2016 from 13h00 to 14h00. Thrust for the V-link system was compared to the numerical propeller thrust (Figure A.6a and A.6c) and shaft line torque was compared to the central measurement unit (CMU) motor torque (Figure A.6b and A.6d).

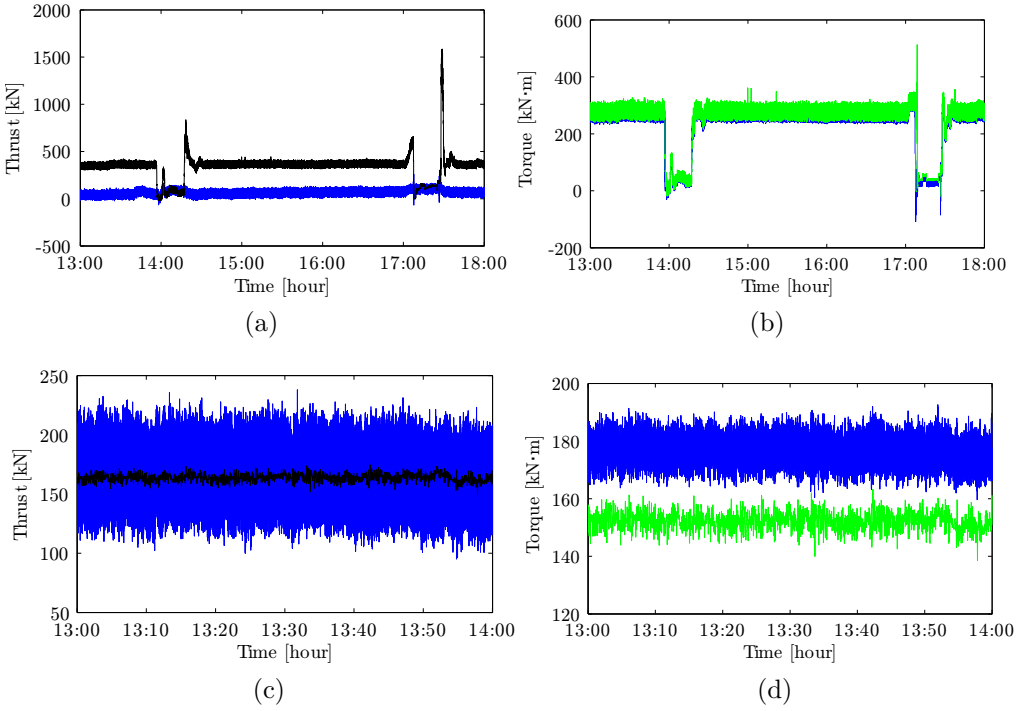

Figure A.6: Data comparison Case 1: 13h to 18h on 5 December 2015 for (a) thrust and (b) torque (SOG: 6.3 knots, shaft speed: 121.0 rpm, pitch: 82.1%, motor power: 3251 kW), Case 2: 13h-14h on 2 February 2016 for (c) thrust and (d) torque (SOG: 7.1 knots, shaft speed: 108.2 rpm, pitch: 99.6%, motor power: 1688 kW). The V-link system is presented by blue, numerical thrust black and the motor torque green.

From Figure A.6, it is clear from the thrust comparisons that the V-link data corresponds better to the numerical thrust for Case 2 compared to Case 1, whereby there are only short durations during which the two data sets overlap. When analysing the torque data, the V-link data corresponds very well to the

motor torque for Case 1, however there was a mean offset of 24.5 kN · m for Case 2. It is expected for the motor torque to closely match the shaft line torque as the shaft line is directly driven from the electric motor. This difference could be attributed to the fact that the dynamic response of the shaft line is superimposed on the hydrodynamic response, therefore the transmissibility between the measured locations on the shaft line and the electric motor needs to be taken into account. There is a large difference in sample rate between the analytical calculations and the torque and thrust data which also needs to be taken into consideration. Furthermore, the V-link data was sampled at 600 Hz, whereas the machine control data was sampled at under 1 Hz. This will effect the accuracy and resolution of the data during comparison.

A correlation comparison between the V-link data and the analytical calculations was performed, as presented in Table A.2. The Spearman correlation r_s is a coefficient ranging from -1 to 1, indicating the strength of the relationship between two variables (Vaughan *et al.*, 2001). A coefficient value of -1 indicates a perfect negative relationship and a value of 1 a perfect positive relationship, with zero no relationship. The Spearman correlation between the V-link, analytical calculations and motor torque was compared using Statistica (Dell Inc., 2015). Spearman correlation was used due to the data sets being ordinal data (Vaughan *et al.*, 2001). The p-value for all correlations were zero and therefore the null hypothesis could be rejected, confirming that a relationship between the data sets exist (Vaughan *et al.*, 2001).

Table A.2: Spearman correlation, r_s, for V-link torque compared to motor torque and V-link thrust compared to analytical calculations.

Thrust		Torque	
Case 1	Case 2	Case 1	Case 2
-0.10	0.06	0.90	0.07

From Table A.2 it is evident that there is a strong correlation for the torque of Case 1, but not for Case 2. There is also very weak to no correlation for the thrust data. These cases did not provide substantial validation of the V-link thrust data. It was therefore decided to conduct model tests in which the

setup of the V-link system and strain calculations could be validated. These tests are presented in Section A.3.

The thrust model test resulted in less than two percent error and the static torque model test resulted in less than three percent error. This could be attributed to the following reasons: Firstly, the Poisson's ratio of the rod was assumed to be that of standard steel $\nu = 0.29$ (Budynas and Nisbett, 2011). Secondly, there is human error involved in sticking strain gauges at the correct angle, gauging the spirit level by eye and measuring the distance from the center of the rod to the applied force. Thirdly, there are slight torque losses introduced in the bearing and the V-link system has an accuracy of $\pm 0.1\%$ (LORD MicroStrain sensing systems, 2015). All of these factors add up to result in the difference in strain measured. The technical drawing for the design of the model and the tensile test specimen are provided in Appendix C.

Due to the machine control parameters not being recorded for the Polarstern, the same type of analysis could not be performed. The engine room does however have a shaft line output display and could therefore be used for validation. This shaft line torque is measured just after the gearbox. A video recording of this output was performed on 30 August 2016 and compared against the recorded shaft line torque, Figure A.7a. The display refreshes at a very low frequency (0.1 Hz) and therefore the resolution of this comparison is compromised. The shaft line torque and engine room display did correlate well and the slight offset could be attributed to the dynamic response of the shaft line which was not accounted for between the two measurement locations.

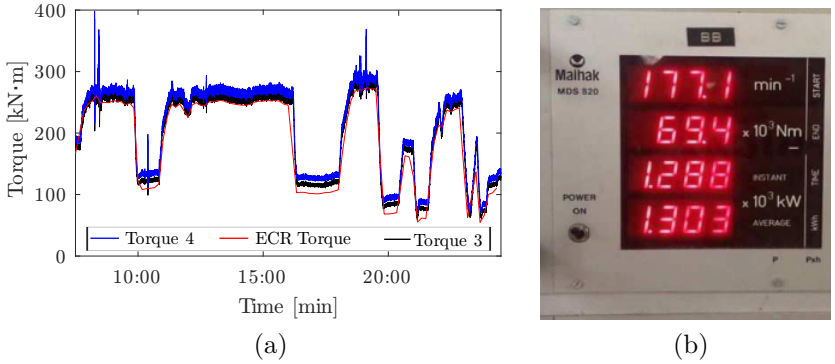

(a) (b)

Figure A.7: (a) Shaft line torque from the Polarstern compared to (b) ECR displayed torque.

During the 2016 Arctic voyage on-board the Polarstern, one of the V-link systems provided unrealistically high torque values compared to the engine room output display and the second V-link. It was therefore decided to replicate the setup on a bending beam experiment, presented in Appendix A.3, through which it was proven that the second LXRS Base station was faulty and streamed inaccurate data to the HBM Quantum. The number of torque channels on the Polarstern shaft line was therefore reduced to only two instead of the originally planned four channels.

A.3 Model tests

In order to eliminate as many variables as possible, static tests on a fixed rod, with the same measurement setup as on the SAA II, was performed. The first test for thrust validation was achieved through the use of a calibrated (18/11/2014) HBM C4 500 kN load cell (Serial number: 69969) and a Alfred J.Amsler & Co. hydraulic press, presented in Figure A.8a. Six tests of thirty seconds each were conducted in which the rod was progressively compressed. The results compared well for the thrust measurements with an overall error of less than two percent. Sample results are provided in Figure A.8b.

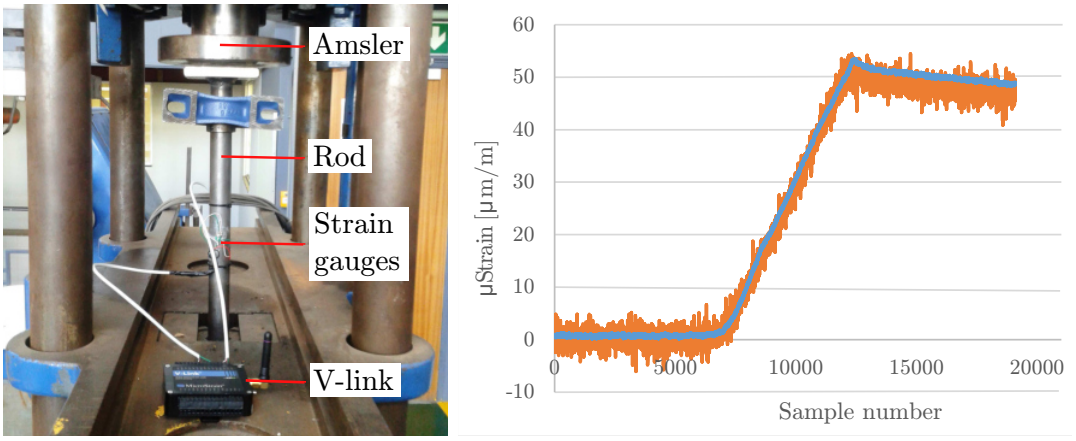

(a) (b)

Figure A.8: Data validation for thrust (a) using a load cell and (b) sample results obtained (blue - V-link, orange - load cell).

A second test was done in order to validate the torque measurement setup.

This was achieved by bolting the rod to a solid surface and applying a known torque to the end of the rod, as presented in Figure A.9a. The torque was induced by hanging weights a known distance from the centre of the rod. To ensure the test was as true as possible, the weights were measured using an electronic scale before the test was conducted.

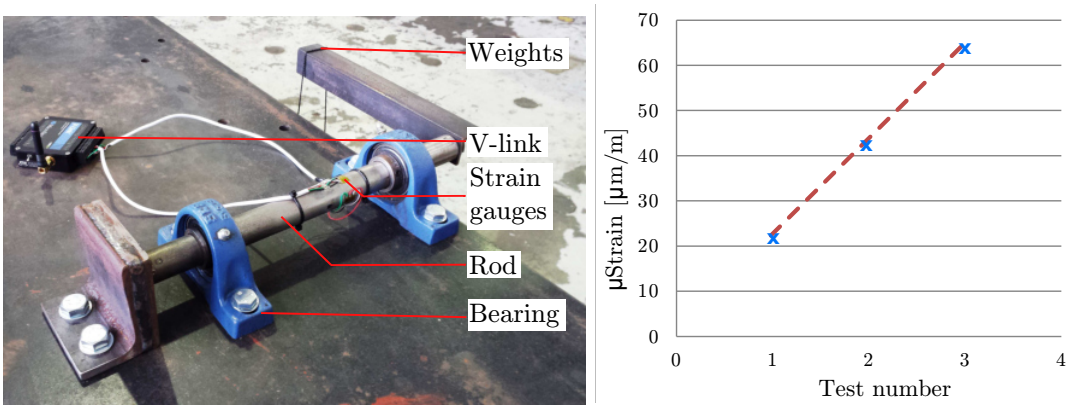

(a) (b)

Figure A.9: Data validation for torque (a) using a known applied load and (b) the results obtained from the three tests (x - measured points, dotted line - calculated).

The inclination of the moment arm was measured with a spirit level before and during each test to ensure that the weight vector was applied vertically and not at an angle, which could result in a reduced moment. The modulus of elasticity of the mild steel rod was determined through two tensile tests. The number of tests were limited to the number of samples that could be extracted from the rod. The average Modulus of Elasticity for the two tensile tests were determined to be 207.97 GPa with a 0.12% difference between the two values. Details of the tensile tests are provided in Section A.4. The gravitational force in the Stellenbosch laboratory was determined to be 9.796 m/s^2 through an online calculator by Physikalisch-Technische Bundesanstalt (2007) that takes latitude, longitude and elevation into account. Three static torque tests were performed during which the applied torque was varied. The tests resulted in less than three percent error, with the results provided in Figure A.9b.

During the 2016 Arctic voyage on-board the Polarstern, one of the V-link systems provided unrealistically high torque values compared to the engine

room output display and the second V-link. It was therefore decided to replicate the setup on a bending beam experiment. Due to limitations with regards to available material and equipment on-board the research vessel, the following setup was created using a mild steel bar and a G-clamp to model a fixed-free beam. Two sets of T-rosette strain gauges were glued on either side of the beam to measure bending stress while eliminating stress induced by a change in temperature. Two weights of around 1.25 kg was used to induce a force at the free end of the beam.

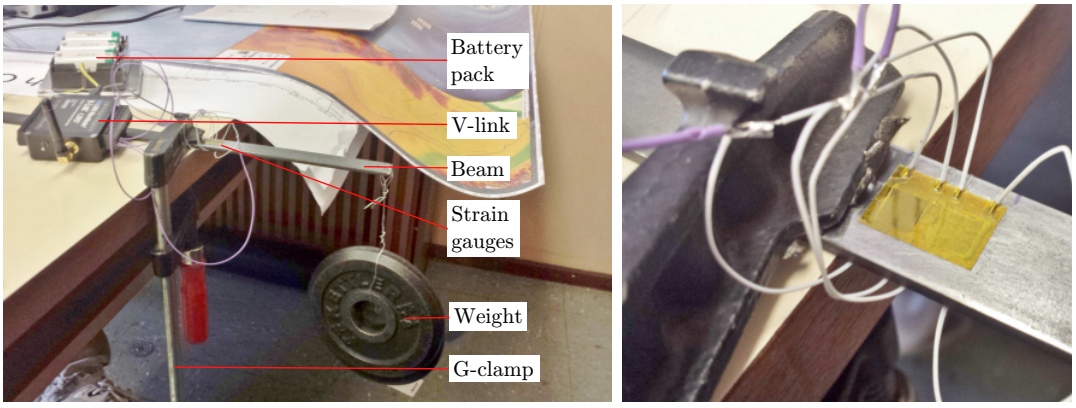

(a) (b)

Figure A.10: Data validation of system setup on-board Polarstern through implementation of a bending test, (a) layout of test and (b) close-up of strain gauges.

The strain gauges were glued 15 mm from the fixed support and therefore would not be able to measure the maximum bending mode. This was accounted for through the use of method of sections. The calculations were performed in SMath Studio (Ivashov, 2010).

Bending strain in beam

07-08-2016 PS100 voyage onboard German Research Vessel Polarstern

Variables:

d_1 := 150 mm Length of beam/distance from support to applied force

d_2 := 15 mm Length from fixed support to strain gauge center

m := 2.5 kg Mass of weight applied to end of beam

Material Properties of the beam:

base := 20 mm

height := 3 mm

E := 207 GPa Modulus of elasticity for mild steel

v := 0, 292 Poisson's ratio for mild steel

Free Body diagram and strain gauge setup:

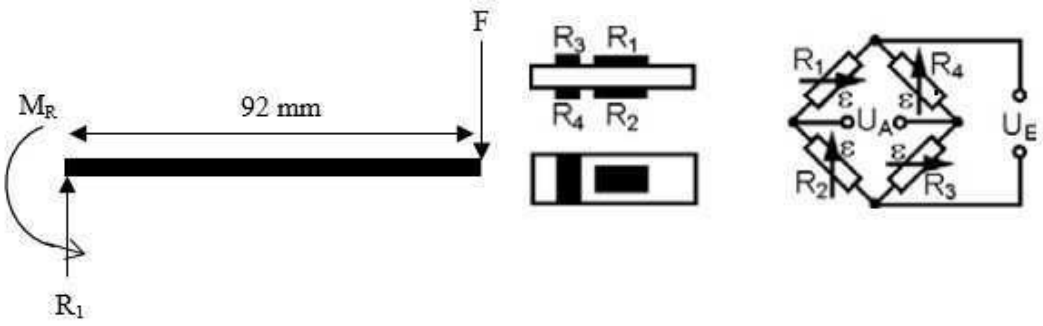

F := mg Force induced by weights

F = 24, 52 N

M_R := F · d_1 Resultant moment from induced force

M_R = 3, 68 J

R_1 := F

R_1 = 24.52 N

The strain gauge was glued 15mm from the fixed support and therefore will not be able to measure the maximum bending moment. This can be accounted for through method of sections:

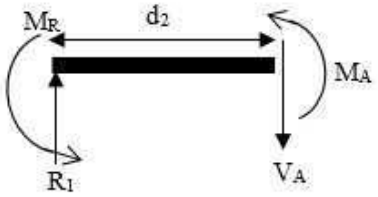

M_A := M_R − R_1 · d_2 Moment experienced by strain gauge

M_A = 3, 31 N m

$I := \frac{base \cdot height^3}{12}$ Moment of inertia

$I = 4, 5 \cdot 10^{-11}\ m^4$

$y := \frac{height}{2}$

$$\sigma := \frac{M\_A \cdot y}{I} \qquad \sigma = 1,1 \cdot 10^{8}\ \text{Pa}$$

$$\varepsilon := \frac{\sigma}{E} \qquad \varepsilon = 532,97\ \frac{\mu m}{m}$$

The stress obtained from the V-link through Node Commander is not the final stress value. This is due to Node Commander not taking additional factors into account and determines stress from the reduced principle formula (Hoffman, 2001):

$$U\_A / U\_E = k\varepsilon$$

The formula for stress during bending is as follows (Hoffman, 2001):

$$\varepsilon = \varepsilon_b = \frac{1}{2(1-\mu)} \cdot \frac{4}{k} \cdot \frac{U_A}{U_E}$$

Therefore, there is a factor of 2/(1-v) that needs to be accounted for. For a single weight applied, the equivalent strain measured by the V-link should be:

$$Strain1 := \varepsilon \cdot \frac{1-v}{2} \qquad Strain1 = 188,67\ \frac{\mu m}{m}$$

Figure A.11: Bending test calculations for the validation of the Polarstern shaft line system.

The mean strain measured during the single weight test was 88.2μ mm/mm. The numerically determined strain was 93.3μ mm/mm, thus there is a 5.5% difference in the results. For the second strain test with two weights applied, the measured strain was 180.9μ mm/mm with the numerically determined strain being 186.5μ mm/mm. Thus a 3% difference. The reason for the difference in results could be attributed to the following factors: the tests were conducted on a moving vessel and therefore a very accurate zero balance could not be established by the V-link, the masses used in the test could not be weighed on a calibrated scale and therefore the manufacturer supplied masses had to be used, the boundary conditions involved through the use of a G-clamp is not ideal, the V-link system has an accuracy of $\pm$0.1% (LORD MicroStrain sensing systems, 2015) and the material properties of standard mild steel (E =207 GPa and $\nu = 0.29$) (Budynas and Nisbett, 2011) had to be assumed.

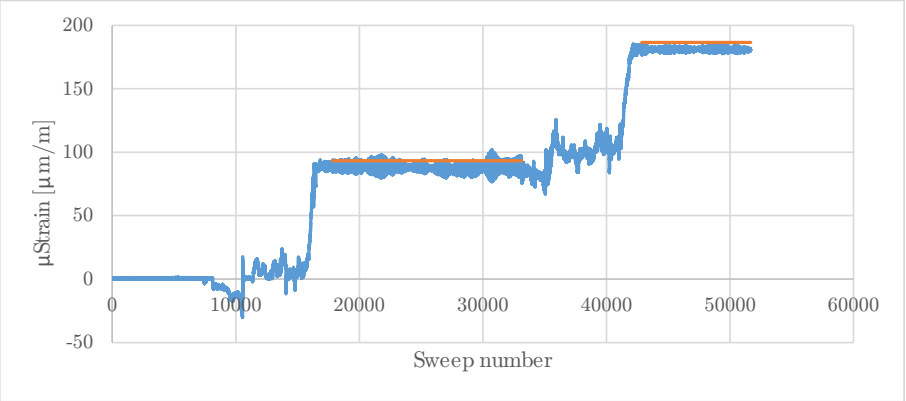

Figure A.12: V-link strain (blue) compared to hand calculations (orange) in order to validate the Polarstern shaft line measurement system.

A.4 Tensile Test

The procedure for conducting a tensile test was based on the E8/E8M-09 Standards by ASTM International E8/E8M-09 (2010). The specimens to be tested were designed in CAD Autodesk Inventor 2016 and presented in Appendix C. Due to the limitation of 25 kN for the tensile test apparatus, the specimens had to be designed accordingly. The following formulas were used to determine the maximum allowed diameter (Budynas and Nisbett, 2011):

$$T_{max} = S_t A \tag{A.7}$$

with

$$A = \pi \left(\frac{d_{max}}{2} \right)^2 \tag{A.8}$$

where

T_{max} is the maximum allowed tensile force [N]
S_t is the tensile strength [Pa]
A is the cross sectional area of the rod [m^2]
d_{max} is the maximum allowed diameter [m]

Using tensile test material properties for cold drawn AISI 1040 as an estimate (Budynas and Nisbett, 2011), Equation A.8 can be substituted into

Equation A.7 to solve for the maximum diameter:

$$25000 = 520 \cdot 10^6 \pi \left(\frac{d_{max}}{2}\right)^2 \tag{A.9}$$

Thus providing an answer of 7.82 mm maximum diameter. In order to ensure the tensile force required will not exceed 25 kN, it was decided to design a specimen, proportional to the E8/E8M-09 Standard, with a diameter of 5 mm which will allow for a safety factor of 1.5. Before the tensile tests were conducted, the specimens were analysed to ensure a smooth surface finish of the reduced section and to ensure no undercutting of the fillets in the reduced section. These inaccuracies could negatively effect the outcomes of the test due to forming stress concentrations causing the specimen to fail prematurely. The diameter of the specimens were measured with a micrometer in order to obtain the true cross sectional area.

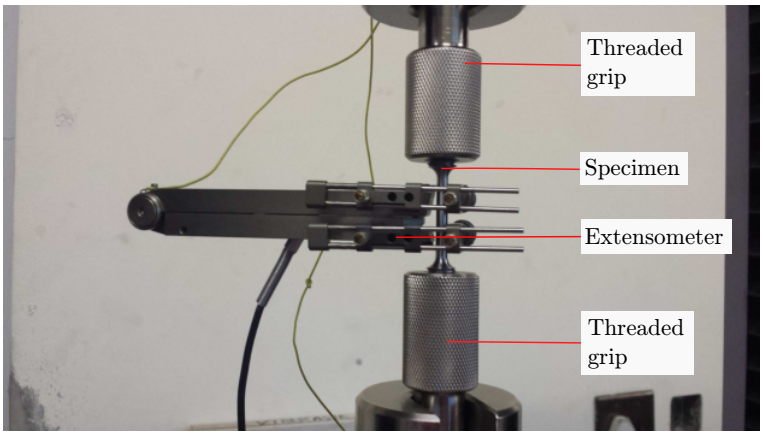

Figure A.13: Tensile test setup with the clip-on tachometer attached.

A MTS Criterion Model 44 (SN: 05000076) was used with a MTS LPS.304 force transducer (SN: 376349) to conduct the tensile tests, presented in Figure A.13. The force transducer was calibrated on 10 November 2016 (Certificate no: SHQ-56868 A+B), five days prior to the test and had a load capacity of 30 kN. According to the control method C in the E8/E8M-09 Standards (ASTM International E8/E8M-09, 2010), the tensile test speed should be set to 0.015 mm/mm/min times the reduced section length. For a 40 mm reduced section, this provides a test speed of 0.6 mm/min. The specimen was attached

to the threaded grips and installed on the tensile test machine. The Mess- & Feinwerktechnik GmbH MFA 25/12 clip-on extensometer was attached and the setup allowed to hang from the top clamp attachment. This was done in order to calibrate the force transducer to zero to exclude the induced load due to gravity. A small initial load was applied to ensure all the equipment had settled, after which the load was reduced to zero and the tensile test started.

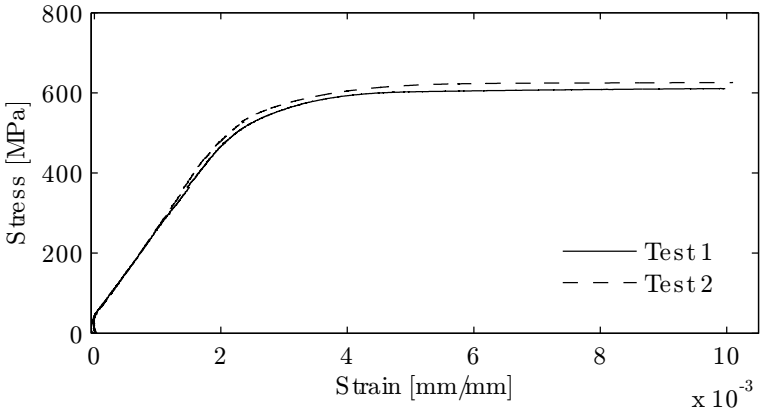

Figure A.14: Tensile test results for mild steel rod with stress versus strain.

The tests were conducted at a sample frequency of 25 Hz, with a duration of roughly 6.5 min. This resulted in a total of just under ten thousand samples, with the first two thousand samples presented in Figure A.14. The Modulus of Elasticity for the two tests was determined to be 207.85 and 208.09 GPa with 0.12% difference between the two.

Appendix B

Specifications

B.1 Accelerometers

Table B.1: Accelerometer specifications for support structure measurements on the SAA II (Manufacturer PCB).

Direction measured	Serial number	Sensitivity
Set1: x (Bow)	333B32 SN 31629	10.20 mV/m/s^2
Set1: y (Starboard)	333B32 SN 18862	9.82 mV/m/s^2
Set1: z (Vertical)	333B32 SN 18871	9.81 mV/m/s^2
Set2: x (Bow)	333B32 SN 38401	10.12 mV/m/s^2
Set2: y (Port)	333B32 SN 31629	10.57 mV/m/s^2
Set2: z (Vertical)	333B32 SN 38404	10.00 mV/m/s^2
Set3: x (Aft)	333B32 SN 31631	10.35 mV/m/s^2
Set3: y (Starboard)	356B40 SN 26977	10.04 mV/m/s^2
Set3: z (Vertical)	356B40 SN 26977	10.25 mV/m/s^2

Table B.2: Accelerometer specifications for support structure measurements on the Polarstern (Manufacturer PCB).

Direction measured	Serial number	Sensitivity
Set1: x (Bow)	SEN021F SN P36546	1.026 mV/m/s^2
Set1: y (Starboard)	SEN021F SN P36546	1.014 mV/m/s^2
Set1: z (Vertical)	SEN021F SN P36546	1.053 mV/m/s^2
Set2: y (Bow)	333B32 SN 18868	10.10 mV/m/s^2
Set2: z (Port)	333B32 SN 38401	10.20 mV/m/s^2

B.2 Strain gauges and V-link system

Table B.3: Strain gauges and V-link system (LORD MicroStrain sensing systems, 2015).

Strain gauges	
Setup	Torque / Thrust
Manufacturer	HBM
Type (SAA II)	VY41 3-350 / XY71 3-350
Type (Polarstern)	XY41 6-350 / XY33 6-350
Description	Full bridge / T-rosette
Gauge resistance	350 ohm
Gauge factor (SAA II)	1,99 / 2,10
Gauge factor (Polarstern)	2,06 / 2,12
Temperature range	−70°C to 200°C
V-link system	
Manufacturer	LORD MicroStrain
Model	V-link LXRS
Resolution	16 bit
Sample rate (continuous)	600 Hz
Bridge supply voltage	3 V
Temperature range	−20°C to 60°C

B.3 Dynamic model

Table B.4: Mass moment of inertia, torsional stiffness and damping constants used for the dynamic model (Rolls-Royce AB, 2010*b*).

Variable	Description	Value
J_1	Propeller	$1.347 \times 10^4\,\mathrm{kg \cdot m^2}$
J_3	Mid propeller shaft	$5.590 \times 10^2\,\mathrm{kg \cdot m^2}$
J_5	Sleeve coupling	$5.120 \times 10^2\,\mathrm{kg \cdot m^2}$
J_7	OD box flange	$4.870 \times 10^2\,\mathrm{kg \cdot m^2}$
J_9	Thrust shaft collar	$1.410 \times 10^2\,\mathrm{kg \cdot m^2}$
J_{11}	Motor flange	$1.740 \times 10^2\,\mathrm{kg \cdot m^2}$
J_{13}	Propulsion motor	$4.415 \times 10^3\,\mathrm{kg \cdot m^2}$
c_1	Water damping	$1.136 \times 10^5\,\mathrm{Nm \cdot s/rad}$
$c_{2,4,\ldots,12}$	Steel shaft	$-180\,\mathrm{Nm \cdot s/rad}$
k_2	Steel shaft	$5.950 \times 10^7\,\mathrm{Nm \cdot rad}$
k_4	Steel shaft	$5.950 \times 10^7\,\mathrm{Nm \cdot rad}$
k_6	Steel shaft	$1.120 \times 10^8\,\mathrm{Nm \cdot rad}$
k_8	Steel shaft	$6.930 \times 10^8\,\mathrm{Nm \cdot rad}$
k_{10}	Steel shaft	$5.090 \times 10^8\,\mathrm{Nm \cdot rad}$
k_{12}	Steel shaft	$1.430 \times 10^8\,\mathrm{Nm \cdot rad}$

B.4 Algorithm

InverseMethod.m

```
%% ======================User input============================
FFT = 0;          % Plot FFT of impulse response matrix (TF)
Reg = 3;          % Plot external torque through: 1 = SVD,
% 2 = GSVD, 3 - Tikhonov
IACS = 0;         % apply IACS exc. torque to propeller
KnownMoment = 1; % Test TF through: 1 = linear,
% 2 = half sine moment imp.
Measured = 0;     % Apply full-scale measurement data
Deviations = 1;  % Add 10% random deviation to variables and
% 650Nm to simulation
% Transfer function between propeller and:
Index = 15; % 1 = T_Prop; 2 = Theta_Prop; 3 = T_shaft1;
% 4 = Theta_shaft1...

%% ====================Initialize values=====================
Beta = 0.25;                % Newmark-Beta constants
Gamma = 0.5;                % Newmark-Beta constants

Fs = 600;                   % Sampling frequency
Dt = 1/Fs;                  % Size of time increments
T_final = 1.2;              % Duration in seconds
C_a = zeros(13,1);          % Variable for elements
C_b = zeros(13,1);          % Variable for elements
D_Theta = zeros(13,1);      % Change in angular displacement
D_Theta_d = zeros(13,1);    % Change in angular velocity
D_Theta_dd = zeros(13,1);   % Change in angular acceleration

%%%%%%%%%%Rolls Royce%%%%%%%%%%
% Mass moment of inertia [kg.m^2]
J_1 = 1.347e4;     % CPP
J_3 = 5.59e2;      % Mid propeller shaft (lumped mass)
J_5 = 5.12e2;      % Sleeve coupling (lumped mass)
J_7 = 4.87e2;      % OD box flange (lumped mass)
J_9 = 1.41e2;      % Thrust shaft collar (lumped mass)
J_11 = 1.74e2;     % Electric motor flange (lumped mass)
J_13 = 4.415e3;    % Propulsion motor
```

```
% Damping [Nm.s/rad]
C_1 = 1.136e5;     % CP Propeller
C_shaft = -180;    % shaft line damping
% Torsional stiffness [Nm/rad]
K_2 = 5.88e7;      % Normal steel shaft
K_4 = 5.95e7;      % Normal steel shaft
K_6 = 1.12e8;      % Normal steel shaft
K_8 = 6.93e8;      % Normal steel shaft
K_10 = 5.09e8;     % Normal steel shaft
K_12 = 1.43e8;     % Normal steel shaft

J = [J_1; 0;  J_3; 0; J_5; 0; J_7; 0; J_9; 0; J_11; 0; J_13];
C = [C_1; C_shaft; 0; C_shaft; 0; C_shaft; 0; C_shaft; 0;...
    C_shaft; 0; C_shaft; 0];
K = [0; K_2; 0; K_4; 0; K_6; 0; K_8; 0; K_10; 0; K_12; 0];
clear var K_2 K_4 K_6 K_8 K_10 K_12
clear var J_1 J_3 J_5 J_7 J_9 J_11 J_13
clear var C_1 C_shaft
% Add deviations to data
if Deviations == 1
    for i = 1:length(J)
        if J(i) ~= 0
            J(i) = (J(i)*1.1-J(i)*0.9)*rand(1,1)+J(i)*0.9;
        end
        if K(i) ~= 0
            K(i) = (K(i)*1.1-K(i)*0.9)*rand(1,1)+K(i)*0.9;
        end
    end
end
%% ======================Initial conditions=======================
G = zeros(T_final*Fs+1);       % Impulse response matrix
Z = zeros(28,T_final*Fs+1);    % Torque and angular displ.
M = zeros(T_final*Fs+1,1);     % Load vector (External moment)
Theta_d = zeros(13,1);         % Change in angular velocity
Theta_dd = zeros(13,1);        % Change in angular acceleration
Theta_d_Pre = zeros(13,1);     % Save previous angular velocity
Theta_dd_Pre = zeros(13,1);    % Save previous angular acc.
D_T_Ext = zeros(13,1);         % Change in ext. torque
W_sub = zeros(26,4);           % Sub-matrices per element
W_pre = zeros(26,28);          % Sub-matrix of sub-matrices along
```

```
% main diag.
W_first = zeros(1,28);          % First node boundary condition
W_first(1) = 1;
W_last = zeros(1,28);           % Last node boundary condition
W_last(27) = 1;
Time = zeros(1,T_final*Fs+1); % Time vector

%% ========Forward problem to determine Unit response function===
for t = 1:T_final*Fs + 1

    % Only apply external torque initially to propeller
    if t == 1
        D_T_Ext(1) = 1;
    else
        D_T_Ext(1) = 0;
    end

    % Loop through each element
    for i = 1:13
        % Test for odd or even
        if mod(i,2) == 0      % Even (Spring)
            C_a(i) = K(i) + (C(i)*Gamma)/(Beta*Dt);
            C_b(i) = C(i)*((Gamma/Beta)*(Theta_d_Pre(i)-...
                Theta_d(i)) + ((Gamma/(2*Beta))-1)*Dt*...
                (Theta_dd_Pre(i)-Theta_dd(i)));
            W_sub((i*2-1):(i*2),:) = [1 C_a(i) 0 -C_a(i);...
                1 0 -1 0];
        else                  % Odd (Inertia)
            C_a(i) = J(i)/(Beta*Dt^2) + (C(i)*Gamma)/(Beta*Dt);
            C_b(i) = J(i)*((1/(Beta*Dt))*Theta_d(i)+...
                (1/(2*Beta))*Theta_dd(i)) + C(i)*...
                ((Gamma/Beta)*Theta_d(i)+...
                (Gamma/(2*Beta)-1)*Theta_dd(i)*Dt) + D_T_Ext(i);
            W_sub((i*2-1):(i*2),:) = [1 C_a(i) -1 0; 0 1 0 -1];
        end
        % Create W matrix and det. change in Torque and theta
        W_pre(2*i-1:2*i,2*i-1:2*i+2) = W_sub((i*2-1):(i*2),:);
    end
    W = [W_first; W_pre; W_last];
    B = [0; C_b(1); 0; C_b(2); 0; C_b(3); 0; C_b(4); 0; ...
```

```
        C_b(5); 0; C_b(6); 0; C_b(7); 0; C_b(8); 0; ...
        C_b(9); 0; C_b(10); 0; ...
        C_b(11); 0; C_b(12); 0; C_b(13); 0; 0];
    [L,U] = lu(W);
    y = L\B;
    D_Z = U\y;

    clear var L U y W B

    for q = 1:13
        D_Theta(q) = D_Z(2*q);
    end
    if t == 1
        Z(:,t) = 0 + D_Z;
    else
        Z(:,t) = Z(:,t-1) + D_Z;
    end
    g_ind = Z(Index,t)*ones(1,length(G)-(t-1));
    % Determine TF between propeller and shaft line
    % measurement location
    G = G + diag(g_ind,(1-t));
    Time(1,t) = (t-1)/Fs;
    % Update variables for each element
    for i = 1:13
        D_Theta_dd(i) = (1/(Beta*Dt^2))*D_Theta(i)-...
            (1/(Beta*Dt))*Theta_d(i)-(1/(2*Beta))*Theta_dd(i);
        D_Theta_d(i) = (Gamma/(Beta*Dt))*D_Theta(i)-...
            (Gamma/Beta)* Theta_d(i)-(Gamma/(2*Beta)-1)*...
            Theta_dd(i)*Dt;
        % Update variables
        Theta_d_Pre(i) = Theta_d(i);
        Theta_dd_Pre(i) = Theta_dd(i);
        Theta_dd(i) = Theta_dd(i) + D_Theta_dd(i);
        Theta_d(i) = Theta_d(i) + D_Theta_d(i);
    end
end
clearvars -except Z G Time FFT Reg TestTF IACS ...
    KnownMoment Deviations Measured Fs Theta_d_Prop Index

figure (1)
```

```
title('Shaft response to step input at measurement location.');
plot(Time,Z(Index,:),'b-','LineWidth',1.5);
xlabel('time [s]'); ylabel('Internal moment [kNm]');
% save('ImpulseResp','G');

%% ========Apply IACS Case 1 loading to propeller to test TF====
if IACS == 1
    % Load IACS excitation torque
    TorqExc = load('IACS_excitation.mat');
    PropTorq = -TorqExc.Q;
    D_PropTorq = zeros(length(PropTorq),1);
    for i = 1:length(PropTorq)
        if i == 1
            D_PropTorq(i) = PropTorq(i);
        else
            D_PropTorq(i) = PropTorq(i) - PropTorq(i-1);
        end
    end
    TimeStruc = load('IACS_Time.mat');
    TimeIn = TimeStruc.Time;
    RespTest = G*D_PropTorq;
    figure (2)
    plot(TimeIn,RespTest);
    xlabel('time [s]'); ylabel('Internal torque [kNm]');
    title('Internal torque response from IACS');
end

%% ==============FFT of determined transfer function=============
if FFT == 1
    NFFT = 2048;     % window size
    noverlap = 50;  % percentage overlap
    XRange = [0 60];
    Overlap = floor((noverlap*NFFT)/100);     %Size of overlap
    Data = detrend(Z(15,:));
    nFrames = floor(length(Data)/Overlap)-1; %Number of frames

    for k = 1:length(nFrames)
        FrameSignal = Data(k:k+NFFT-1);
        %Select range of data to be processed for overlap
        % and windowing
```

```
        win = hanning(NFFT); %Define window and size
        %         win = flattopwin(WinSize);
        winData = FrameSignal(:).*win;  %Window frame data
        Y1 = fft(winData,NFFT);  %Determine fft of windowed data
        f1 = (Fs/2)*linspace(0,1,NFFT/2+1);
        % Only determine frequency for first half of data,
        % second half is a repitition of the first.

        % Plot single-sided amplitude spectrum
        figure (3)
        semilogy(f1,2*abs(Y1(1:NFFT/2+1))/length(winData),...
            'k','LineWidth',1);
        hold on;
    end

    xlabel('Frequency [Hz]');
    ylabel('|Internal Torque [kNm]|');
    xlim(XRange)
end

%% ==================Apply known ice moment impulse=============
%=============linear moment impulse==================
if KnownMoment == 1
    IceMom = zeros(length(Time),1);
    for i = 1:length(Time)
        if Time(i) < 0.04
            IceMom(i) = 0;
        elseif Time(i) >= 0.04 && Time(i) <0.06
            IceMom(i) = 10^4*Time(i)-400;
        elseif Time(i) >=0.06 && Time(i) < 0.08
            IceMom(i) = -10^4*Time(i)+800;
        else
            IceMom(i) = 0;
        end

    end
    %================Half sine moment impulse==============
elseif KnownMoment == 2
    IceMom = zeros(length(Time),1);
    for i = 1:length(Time)
```

```
        if Time(i) < 0.04
            IceMom(i) = 0;
        elseif Time(i) >= 0.04 && Time(i) <0.08
            IceMom(i) = -175*sin(2*pi*12.5*Time(i));
        else
            IceMom(i) = 0;
        end
    end
end

if KnownMoment ~= 0
    % Regularization matrix L
    L = zeros(length(Time),length(Time));
    L_1 = ones(1,length(Time)-1);
    L_2 = -ones(1,length(Time));
    L = L + diag(L_1,1);
    L = L + diag(L_2,0);
    L = L(1:end-1,:);

    D_IceMom = L*IceMom;
    D_IceMom = [D_IceMom; 0];
    % insert last value lost through delta calc
    Resp = -G*D_IceMom;

    figure (4)
    plot(Time,IceMom,'b');
    hold on;
    plot(Time,Resp,'r');
    title('Shaft response to known linear moment impulse');
    xlabel('Time [s]'); ylabel('Internal torque [kNm]');
    hold on;

end

if Deviations == 1 && KnownMoment ~= 0
    pm = rand(length(Resp),1);
    pm(pm<0.5) = -1;
    pm(pm>=0.5) = 1;
    for i = 1:length(Resp)
        Resp(i) = Resp(i) + pm(i)*0.65*rand(1,1);
```

```
    end
    figure (4)
    plot(Time,Resp,'g');
    legend('Ice moment impulse','Shaft response',...
        'Shaft response with dev.');
end

%% ============================Measured data ====================
if Measured == 1
    Data_Meas = load('SAAII_Max.mat');
    Resp = detrend(Data_Meas.Torq);
    Diff = Data_Meas.Torq - Resp;
    figure (4)
    plot(Time,Resp,'b');
    title('Measured shaft line torque');
    xlabel('Time [s]'); ylabel('Internal torque [kNm]');
end

%% ============================Inverse methods===================
%==================SVD=======================
if Reg ~= 0
    % First order regularization matrix
    L = zeros(length(Time),length(Time));
    L_1 = ones(1,length(Time)-1);
    L_2 = -ones(1,length(Time));
    L = L + diag(L_1,1);
    L = L + diag(L_2,0);
    L = L(1:end-1,:);
end
if Reg == 1
    [U,s,V] = csvd(G);
    [D_M,rho,eta] = tsvd(U,s,V,Resp,150);
    % Update external moment on propeller
    for q = 1:length(D_M)
        if q == 1
            M(q) = 0 + D_M(q);
        else
            M(q) = M(q-1) + D_M(q);
        end
    end
```

```
    figure (5)
    plot(Time,-M,'k');
    title('External moment determined through SVD');
    ylabel('External moment [Nm]'); xlabel('time [s]');
    hold on;
    plot(Time,IceMom,'r');
    legend('Determined load','Actual load')

    %==================GSVD=======================
elseif Reg == 2
    [U,sm,X,V,W] = cgsvd(G,L);
    figure (10)
    [reg_corner,rho,eta,reg_param] = l_curve(U,sm,Resp,...
        'tsvd',L,V);
    hold on;
    [D_M,rho,eta] = tgsvd(U,sm,X,Resp,reg_corner);

    % Update external moment on propeller
    for q = 1:length(D_M)
        if q == 1
            M(q) = 0 + D_M(q);
        else
            M(q) = M(q-1) + D_M(q);
        end
    end
    % Plot results
    figure (5)
    plot(Time,-M,'b');
    title('External moment determined through GSVD');
    ylabel('External moment [Nm]'); xlabel('time [s]');
    hold on;
    plot(Time,IceMom,'r');
    legend('Determined load','Actual load')

    %================Tikhonov=====================
elseif Reg == 3
    Lambda = 5.12*10^(-2);
    [U,sm,X,V,W] = cgsvd(G,L);
    figure (10)
    [reg_corner,rho,eta,reg_param] = l_curve(U,sm,Resp,...
```

```
        'Tikh');
    hold on;
    [D_M,rho,eta] = tikhonov(U,sm,X,Resp,reg_corner);

    % Update external moment on propeller
    for q = 1:length(D_M)
        if q == 1
            M(q) = 0 + D_M(q);
        else
            M(q) = M(q-1) + D_M(q);
        end
    end
    % Plot results
    figure (5)
    plot(Time,-M,'g');
    title('External moment determined through Tikhonov');
    ylabel('Ext Moment [Nm]'); xlabel('time [s]');
    hold on;
    plot(Time,IceMom,'r');
    legend('Determined load','Actual load')
end
```

Appendix C

CAD drawings

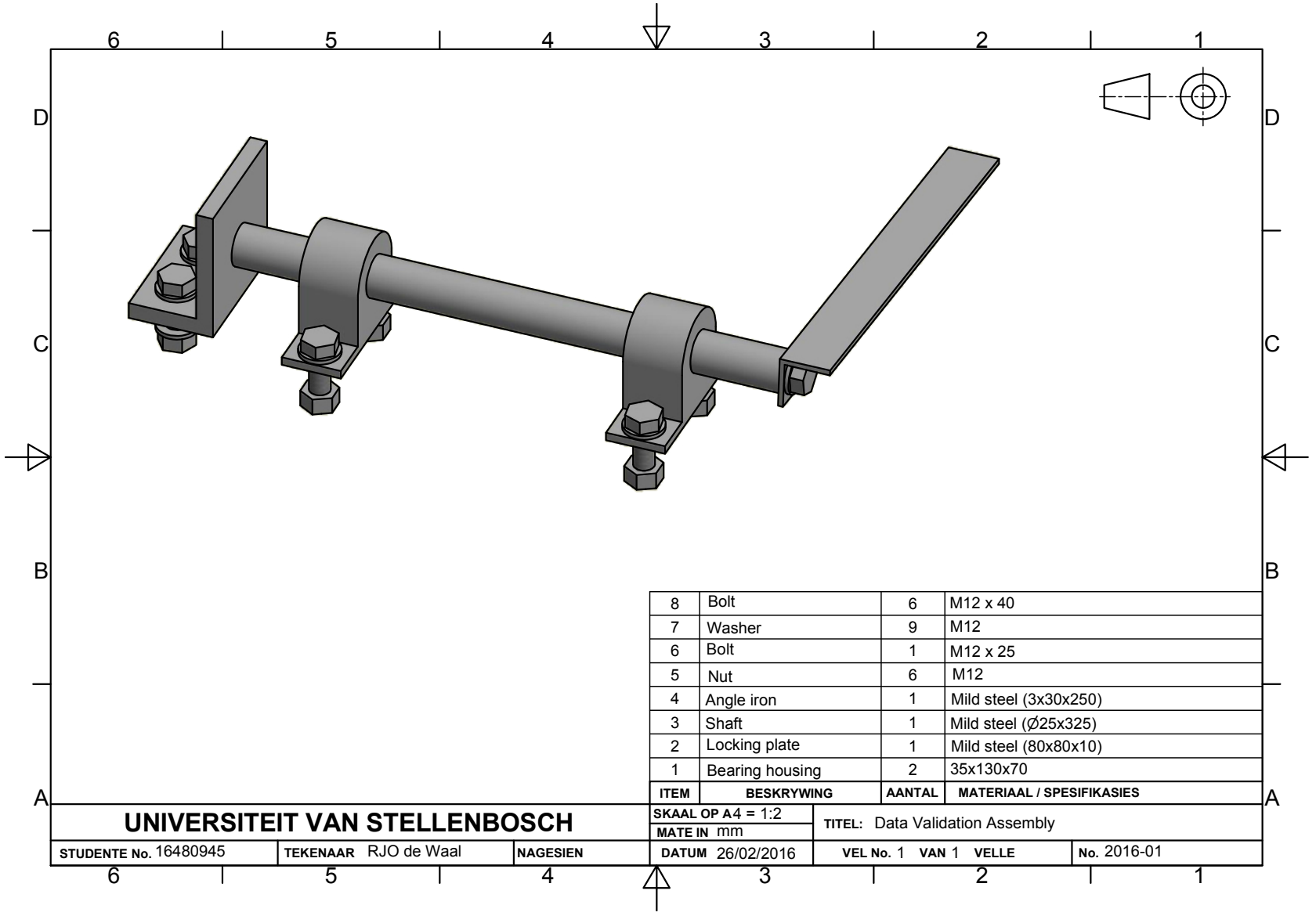

Figure C.1: Drawing of the model used to validate the V-link setup and calculations.

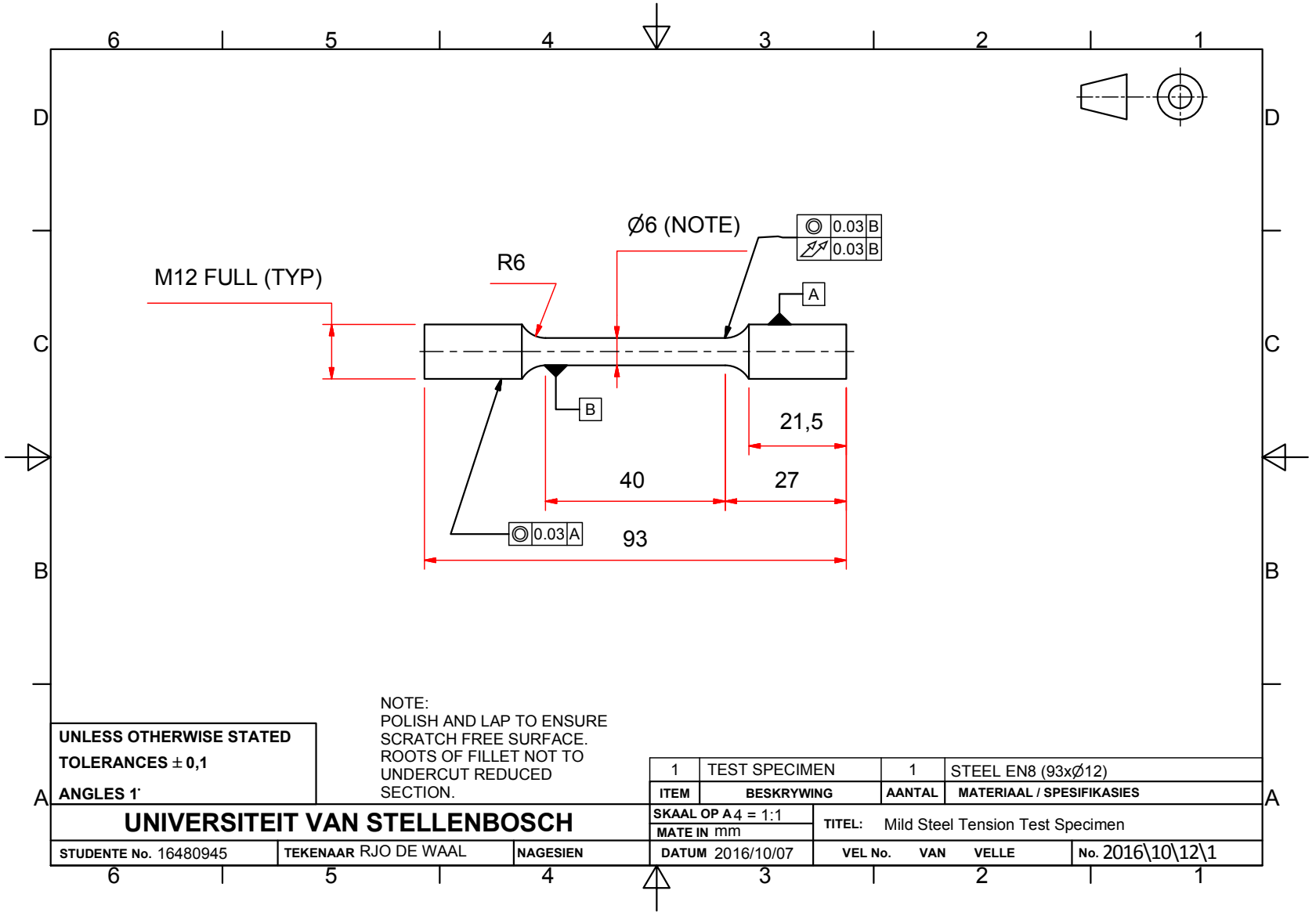

Figure C.2: Drawing of the machined specimen from the shaft on which data validation tests were performed.

List of References

Al-Bedoor, B., Aedwesi, S. and Al-Nassar, Y. (2006). Blades condition monitoring using shaft torsional vibration signals. *Journal of Quality in Maintenance Engineering*, vol. 12, no. 3, pp. 275–293.

American Bureau of Shipping (2006). Guidance notes on ship vibration.

Araujo, L.S., Mendes, M.C., de Almeida, L.H., Dutra, M.S. and Cardoso, D. (2013). Failure of a concentric pipe for a controllable pitch propeller system. *Journal of Failure Analysis and Prevention*, vol. 14, no. 1, pp. 55–60.

ASTM International E1049-85 (2011). ASTM E1049-85: Standard practices for cycle counting in fatigue analysis.

ASTM International E8/E8M-09 (2010). ASTM E8/E8M-09: Standard test methods for tension testing of metallic materials.

AWI (2015). Ocean Data View.
Available at: http://odv.awi.de/en/home/

Barro, R.D. and Lee, D.C. (2011). Excitation response estimation of polar class vessel propulsion shafting system. *Transactions of the Korean Society for Noise and Vibration Engineering*, vol. 21, no. 12, pp. 1166–1176.

Batrak, Y. (2010). *Torsional vibration calculation issues with propulsion systems.*

Batrak, Y.A., Serdjuchenko, .M. and Tarasenko, A.I. (2012). Calculation of propulsion shafting transient torsional vibration induced by ice impacts on the propeller blades. In: *Fourth World Maritime Technology Conference*, May 29 - June 1, pp. 1–8. Saint-Petersburg.

Batrak, Y.A., Serdjuchenko, A.M. and Tarasenko, A.I. (2014). Calculation of torsional vibration responses in propulsion shafting system caused by ice impacts. In: *Torsional Vibration Symposium*, May 21-23. Salzburg.

Brouwer, J., Hagesteijn, G. and Bosman, R. (2013). Propeller-ice impacts measurements with a six-component blade load sensor. In: *Third International Symposium on Marine Propulsors*, May 5-8, pp. 47–54. Tasmania.

Budynas, R.G. and Nisbett, J.K. (2011). *Shigley's mechanical engineering design*. 9th edn. McGraw-Hill, New York.

Casciani-Wood, J. (2015). An introduction to propeller cavitation. Available at: http://www.iims.org.uk/introduction-propeller-cavitation/

Chen, D. (2006). An exact solution for free torsional vibration of a uniform circular shaft carrying multiple concentrated elements. *Journal of Sound and Vibration*, vol. 291, no. 3-5, pp. 627–643.

Connor, S.O., Arbor, A., Lynch, J.P., Arbor, A. and Law, K.H. (2010). Fatigue life monitoring of metallic structures by decentralized rainflow counting embedded in a wireless sensor network. In: *ASME 2010 Conference on Smart Materials, Adaptive Structures and Intelligent Systems*, September 28 - October 1. Philadelphia, PA, USA.

Dell Inc. (2015). Statistica.

Det Norske Veritas (2011*a*). Classification of ships for navigation in ice. *Rules for Classification of Ships*, vol. 5, no. 1322.

Det Norske Veritas (2011*b*). Ice strengthening of propulsion machinery. *Classification Notes*, vol. 1, no. 51.

Dinham-Peren, T. and Dand, I. (2010). The need for full scale measurements. In: *William Froude Conference: Advances in Theoretical and Applied Hydrodynamics - Past and Future*, November 24. Portsmouth.

Doyle, J.F. (1987). Experimentally determining the contact force during the transverse impact of an orthotropic plate. *Journal of Sound and Vibration*, vol. 118, no. 3, pp. 441–448.

Dukkipati, R.V. (2010). *MatLab - An introduction with applications*. New Age International Publishers, New Delhi.

Dykes, L. and Reichel, L. (2014). Simplified GSVD computations for the solution of linear discrete ill-posed problems. *Journal of Computational and Applied Mathematics*, vol. 255, pp. 15–27.

Encyclopædia Britannica (2016). Cavitation.
Available at: http://www.britannica.com/science/cavitation

Escher Wyss (1980). Gesamtanordnung VP Anlage.

Finnish Maritime Administration and Swedish Maritime Administration (2005). Guidelines for the application of the Finnish - Swedish Ice Class Rules. vol. 1.

Gao, Y. and Randall, R. (1999). Reconstruction of diesel engine cylinder pressure using a time domain smoothing technique. *Mechanical Systems and Signal Processing*, vol. 13, no. 5, pp. 709–722.

Germanischer Lloyd (1981). Test certificate for shaft line materials.

Germanischer Lloyd (2007). Rules for classification and construction. *Part 6 Offshore Technology, Chapter 5 Machinery Installations, Section 7 Torsional Vibrations.*

Golub, G.H., Hansen, P.C. and O'Leary, D.P. (1999). Tikhonov regularization and total least squares. *Siam Journal on Matrix Analysis and Applications*, vol. 21, no. 1, pp. 185–194.

Google (2016). Google Maps - Greenland Sea.
Available at: https://www.google.com/maps/@-33.9366817,18.8729732,15z

Grobe, H. and Alfred Wegener Institute (2007). Photo from the German research vessel Polarstern port propeller.
Available at: https://commons.wikimedia.org/wiki/File:Polarstern{_}propeller-bb{_}hg.jpg

Hansen, P.C. (1998). Regularization tools.
Available at: https://www.mathworks.com/matlabcentral/fileexchange/52-regtools

Hansen, P.C. (2001). *Computational inverse problems in electrocardiology*, vol. 5. WIT Press, Southampton.

Hansen, P.C. (2008). Regularization tools - a MatLab package for analysis and solution of descrete ill-posed problems.

He, Q. and Du, D. (2010). Modeling and calculation analysis of torsional vibration for turbine generator shafts. *Journal of Information and Computational Science 7*, vol. 10, pp. 2174–2182.

Hibbeler, R. (2011). *Mechanics of materials*. 8th edn. Pearson Prentice Hall, Singapore.

Hoffmann, K. (2001). Applying the wheatstone bridge circuit. *HBM W1569-1.0 en, HBM, Darmstadt, Germany*, pp. 1–28.

Huisman, T.J., Bos, R.W., Hagesteijn, G., Brouwer, J. and de Koning Gans, H.J. (2014). Interaction between warm model ice and a propeller. In: *Proceedings of the ASME 2014 33rd International Conference on Ocean, Offshore and Arctic Engineering OMAE2014*, June 8-13. San Francisco, California, USA.

Ikonen, T., Peltokorpi, O. and Karhunen, J. (2014). Inverse ice-induced moment determination on the propeller of an ice-going vessel. *Cold Regions Science and Technology*, vol. 112, pp. 1–13.

Inman, D. (2014). *Engineering vibration*. 4th edn. Pearson Education, USA.

International Association of Classification Societies (2016). Requirements concerning polar class.

Ivashov, A. (2010). SMath Studio Desktop.

Jacquelin, E., Bennani, A. and Hamelin, P. (2003). Force reconstruction: Analysis and regularization of a deconvolution problem. *Journal of Sound and Vibration*, vol. 265, no. 1, pp. 81–107.

Jensen, F.B., Kuperman, W.A., Porter, M.B. and Schmidt, H. (2011). Chapter 2: Wave propagation theory. In: *Computational Ocean Acoustics*, vol. 97, pp. 65–154. arXiv:1011.1669v3.

Jussila, M. and Koskinen, P. (1989). Ice loads on propeller blade of small car ferry. In: *The 10th International Conference on Port and Ocean Engineering under Arctic Conditions (POAC)*, vol. 2, pp. 862–872. Luleå, Sweden. arXiv: 1011.1669v3.

Korean Register (2015). Guidance for ship for navigation in ice.
Available at: http://www.krs.co.kr/KRRules/KRRules2015/KRRulesE.html

Kuiper, G. (1997). Cavitation research and ship propeller design. *Applied scientific research*, vol. 58, no. 1, pp. 33–50.

Kujala, P., Kulovesi, J., Lehtiranta, J. and Suominen, M. (2014). Full-scale measurements on board S.A. Agulhas II in the Antarctic waters 2013-2014. Tech. Rep., Aalto University.

Kushwaha, V. (2012). *Analysis of torsional vibration characteristics for multi-rotor and gear-branched systems using finite element method.* Ph.D. thesis, National Institute of Technology.

LORD MicroStrain sensing systems (2015). LORD product datasheet: V-Link LXRS. *LORD product datasheet.*

Manner Sensortelemetrie (2012). Inductive sensortelemetry multi channel sensor signal amplifiers and receivers.

Martelli, M., Figari, M., Altosole, M. and Vignolo, S. (2013). Controllable pitch propeller actuating mechanism, modelling and simulation. *Proceedings of the Institution of Mechanical Engineers, Part M: Journal of Engineering for the Maritime Environment*, vol. 228, no. 1, pp. 29–43.

Matusiak, J. (2013). *Dynamics of a rigid ship.* Aalto University publication series, Helsinki.

McGraw-Hill Dictionary of Scientific & Technical Terms (2003). Torsional vibration. Available at: http://encyclopedia2.thefreedictionary.com/torsional+vibration

Metallurgica Veneta (2004). Material specifications for S355J2.

Myklebost, M.R. and Dahler, G. (2013). Agulhas II data analysis of torsional shaft responses from operation in Arctic waters - Technical summary report. *Det Norske Veritas AS.*

Nieslony, A. (2003). Rainflow counting algorithm. Available at: https://www.mathworks.com/matlabcentral/fileexchange/3026-rainflow-counting-algorithm

Peltokorpi, O., Bekker, A., Kulovesi, J., Suominen, M., Kujala, P. and Karhunen, J. (2014). Full-scale measurements on a polar supply and research vessel during maneouver tests in an ice field in the Baltic Sea. In: *Proceedings of the ASME*

2014 33rd International Conference on Ocean, Offshore and Arctic Engineering OMAE2014. San Francisco, California, USA.

Physikalisch-Technische Bundesanstalt (2007). Gravity Information System PTB. Available at: http://www.ptb.de/cartoweb3/SISproject.php

Polić, D., Ehlers, S., Æsøy, V. and Pedersen, E. (2014). Shaft response as a propulsion machinery design load. In: *Proceedings of the ASME 2014 33rd International Conference on Ocean, Offshore and Arctic Engineering OMAE2014*. California,.

Rolls-Royce AB (2010*a*). Axial vibration calculation. *Report SA1091*, pp. 1–15.

Rolls-Royce AB (2010*b*). Ice impact simulation - polar research vessel. *RRAB STX Research Vessel RES 05B40400 20100414*, vol. 110, pp. 1–9.

Rolls-Royce AB (2010*c*). Whirling calculation. *Report SA1090*, pp. 1–15.

Sampson, R., Atlar, M. and Sasaki, N. (2009). Propeller ice interaction - effect of blockage proximity. In: *First International Symposium on Marine Propulsors*, June. Trondheim, Norway.

Sharma, S.D., Mani, K. and Arakeri, V.H. (1990). Cavitation noise studies on marine propellers. *Journal of Sound and Vibration*, vol. 138, no. 2, pp. 255–283.

Ship Year (2013). STX SA Agulhas II documentary: taking Antarctic exploration to the next level.
Available at: http://www.shipyearonline.co.za/articles/documentary-stx-sa-agulhas-2-4332.html

STX Finland Oy (2012). Polar supply and research vessel shaft line arrangement.

Tang, B. and Brennan, M.J. (2013). On the influence of the mode-shapes of a marine propulsion shafting system on the prediction of torsional stresses. *Journal of Marine Science and Technology*, vol. 21, no. 2, pp. 209–214.

The Alfred Wegener Institut (2016). Technical data.
Available at: http://www.fs-polarstern.de/index.php?lang=EN{&}aktion=anzeigen{&}rubrik=015006

Transport Safety Agency (2010). Finnish ice classes equivalent to class notations of recognized classification societies. *Maritime Safety Regulations*.

Transportation Safety Board of Canada (2010). Statistical summary marine occurences 2010.

Vaughan, L., for Information Science, A.S. and Technology (2001). *Statistical methods for the information professional: a practical, painless approach to understanding, using, and interpreting statistics*. ASIST monograph series. American Society for Information Science and Technology.

Walker, D.L.N. (1996). *The influence of blockage and cavitation on the hydrodynamic performance of ice class propellers in blocked flow*. Ph.D. thesis, Memorial University of Newfoundland.

Werft Nobiskrug GmbH (1980). Wellenleitung, Hauptmasse.

Wilson, E.L. (2002). *Three-dimensional static and dynamic analysis of structures - A physical approach with emphasis on earthquake engineering*, vol. 90. 3rd edn. California, USA.

Wirgin, A. (2004). The inverse crime. *Cornell University Library*.